Trinity College Dublin
Coláiste na Tríonóide, Baile Átha Cliath
The University of Dublin

SCHOOL OF CHEMISTRY

Dr Cristina Trujillo & Prof Stephen Connon

CATALYSIS OF ORGANIC REACTIONS THROUGH NON-COVALENT INTERACTIONS

NIKA MELNYK

4TH JUNE 2026

SUBMITTED IN PARTIAL FULFILMENT OF THE REQUIREMENTS FOR THE DEGREE OF PHD IN CHEMISTRY

Declaration

I hereby declare that this Thesis is entirely my own work and that it has not been submitted as an exercise for a degree at this or any other university.

I have read and I understand the plagiarism provisions in the General Regulations of the University Calendar for the current year, found at `http://www.tcd.ie/calendar`.

I have also completed the Online Tutorial on avoiding plagiarism 'Ready Steady Write', located at `http://tcd-ie.libguides.com/plagiarism/ready-steady-write`.

Signed:  Date: 4th June 2026

Abstract

This thesis presents a computational investigation into halogen bonding (XB) as a foundation for organocatalyst design, positioning it as both an alternative and a complement to traditional hydrogen-bond (HB) catalysis. While often compared to HB, XB interactions display unique characteristics, most notably a high degree of directionality, tunability, and mechanistic versatility, and the ability to promote different activation modes, making them a unique platform for catalyst development. The work is structured around successive chapters, beginning with a systematic computational study of symmetric monovalent XB scaffolds. By analysing the relationship between scaffold geometry, electronic structure, and donor accessibility, this part reveals how subtle variations in orientation and flexibility can dramatically alter substrate activation. It also demonstrates that XB catalysis is not limited to a single mechanistic pathway but can operate through multiple, context-dependent activation modes. Building on these principles, the thesis explores hypervalent XB architectures, where enforced rigidity and geometric control fundamentally reshape activation preferences. These donors emerge not as extensions of monovalent scaffolds, but as a distinct and powerful class of XB-based catalysts. The final chapter of the thesis examines the influence of counterions and intramolecular interactions, showing that counterions can actively stabilise specific key conformations and modulate σ-hole accessibility, thereby exerting a direct influence on catalytic behaviour. Together, these findings establish a comprehensive framework for computational design of XB-based organocatalysts, outlining the principles of scaffold design, mechanistic diversity, and environmental effects that define their reactivity and potential

in asymmetric synthesis.

Acknowledgements

I would first like to extend my deepest gratitude to my supervisor, Dr Cristina Trujillo. Thank you for the opportunity to undertake what has been a truly life-changing experience. Through your guidance, expertise, and unwavering dedication to science, I have been able to grow personally, professionally, and scientifically into a version of myself I did not previously know was possible.

I would also like to thank all those who made this journey possible. I am especially grateful to Dublin Institute of Technology, where my interest in Chemistry was first sparked on Kevin Street. Thank you to Dr Sarah Rawe and Dr Claire McDonnell, whose dedicated and intentional approach to education truly engaged me in the field. I thank Trinity College Dublin for hosting my PhD and for providing such a multifaceted experience across research, teaching, and outreach. I am also grateful to ICHEC and MeluXina for the computational resources and countless CPU hours that made the projects I worked on possible.

To my closest friends, thank you for grounding me throughout this journey and reminding me to maintain balance and perspective. Last, but certainly not least, I would like to thank my family. Thank you for the unwavering support and their courage to make sacrifices that made opportunities such as this possible for me.

I would like to acknowledge the memorable characters I encountered along the way. Thank you to the Connon Group for their impeccable hospitality and for always making the Trujillos feel welcome and included. I am grateful to be part of the Trujillo Group, a supportive community of brilliant and unique individuals, and it has been an honour to grow alongside you.

A special thank you to Iñigo, Diana, and Tim. Iñigo, my muse, thank you for your patience, authenticity, and generosity with your time and knowledge. You have inspired me both inside and outside the camera lens. Diana, separated by the

Carpathian Mountains and reunited in Ireland. I still don't know how we managed to work while talking about absolutely everything under the sun. Thank you for the manic adventures, past, present and future. Tim, I deeply cherish our friendship and bond. Thank you for always grounding me with your logic and wisdom.

In a world often driven by materialism, it is important to remember that education is a privilege and one of the truest measures of an enriched life. While this experience has been a testament to dedication and resilience, I firmly believe that you are only as strong as your support system, and for that, I am incredibly fortunate.

Contents

List of Figures

List of Tables

Acronyms

AARON Automated Reaction Optimiser for New Catalysts

ACE Asymmetric Catalyst Evaluation

ASO Averaged Steric Occupancy

BCP Bond Critical Point

BD Bonding Orbital

BD* Antibonding Orbital

BM1 Binding Mode 1

BM2 Binding Mode 2

BM3 Binding Mode 3

BOA Born Oppenheimer Approximation

CatVS Catalyst Virtual Screening

CC Coupled Cluster

CCP Cage Critical Point

cc Correlation Consistent

CGF Contracted Gaussian Functions

ChB Chalcogen Bonding

CI Configuration Interaction

CP Critical Point

CREST Conformer Rotamer Ensemble Sampling Tool

CT Charge Transfer

DCM Dichloromethane

DFT Density Functional Theory

EWG Electron Withdrawing Group

FCC Fluid Catalytic Cracking

FDE Framework Distortion Energy

GGA Generalised Gradient Approximation

GS Ground State

GTO Gaussian Type Orbitals

HB Hydrogen Bonding

HBeXB Hydrogen Bond Enhanced Halogen Bonding

HF Hartree Fock

ICl3 Iodine Trichloride

LCAO Linear Combination of Atomic Orbitals

LDA Local Density Approximation

LP Lone Pair

LSDA Local Spin Density Approximation

MEP Molecular Electrostatic Potential

ML Machine Learning

MP Moller Plesset

NAO Natural Atomic Orbital

NACP Nuclear Attractor Critical Point

NBO Natural Bond Orbital

NCI Noncovalent Interaction

NHO Natural Hybrid Orbital

NIS N Iodoimides

NLS Natural Lewis Structure

PBE Perdew Burke Ernzerhof

PES Potential Energy Surface

PLA Biodegradable Poly Lactic Acid

PnB Pnictogen Bonding

PreTS Pre Transition State

PT2 Perturbative Second Order

QM/MM Quantum Mechanical Molecular Mechanical

QTAIM Quantum Theory of Atoms in Molecules

RCP Ring Critical Point

RMSD Root Mean Square Deviation

ROP Ring Opening Polymerisation

SCF Self Consistent Field

SCR Selective Catalytic Reduction

SE Schrodinger Equation

SMD Solvation Model Based on Density

STO Slater Type Orbitals

TDSE Time Dependent Schrodinger Equation

TISE Time Independent Schrodinger Equation

TS Transition State

XB Halogen Bonding

XC Exchange Correlation

1 Introduction

1.1 Catalysis – A Cornerstone of Chemical Science

Chemical reactions underpin both life and modern society, from the biochemical processes within cells to the manufacture of medicines, materials, and energy technologies. Most reactions, however, are kinetically inaccessible under practical conditions due to substantial activation barriers. Catalysis overcomes these barriers, enabling efficient and selective transformations in which small quantities of catalyst convert vast amounts of material. As a result, catalysis lies at the core of chemical science and plays a central role in addressing global challenges spanning sustainable energy, environmental remediation, agriculture, and healthcare. As illustrated in Figure 1.1, this section traces key milestones in the evolution of catalysis, underscoring its enduring adaptability in tandem with societal change. Catalysis traces its origins to biological systems and early human practice. Enzymes drive the essential reactions of living systems, and humans have applied catalytic processes for millennia, exemplified by carbohydrate fermentation to produce wine, beer, and acetic acid before 2000 BCE. The deliberate application of chemical catalysts emerged much later, with the first recorded inorganic example reported in 1552 when Valerius Cordus used sulfuric acid to convert alcohol into ether.[1,2] Early observations remained largely empirical until Berzelius coined the term *catalysis* in 1835, formalising the concept through systematic analysis.[3] By the late nineteenth and early twentieth centuries, the combined contributions of Ostwald, Haber, Bosch, and Mittasch transformed catalysis from serendipitous practice into an engineered scientific discipline, enabling hundreds of

catalytic processes and industrial-scale bulk chemical production.[1,4]

Bridging theory and practice, Wilhelm Ostwald established the foundational principles of catalysis, chemical equilibria, and reaction kinetics, work recognised with the 1909 Nobel Prize in Chemistry.[1,5,6] These principles directly enabled industrial translation, with Haber demonstrating small-scale ammonia synthesis using an iron-based catalyst by 1905.[1,3,5–8] Industrial implementation at BASF, led by Bosch and enabled by Mittasch's catalyst development, established the Haber-Bosch process as a template for modern high-pressure catalysis.[6,8–10] This platform subsequently enabled a wide range of bulk chemical technologies, including methanol synthesis, Fischer-Tropsch hydrocarbon production, and petroleum refining processes such as catalytic cracking and reforming.[4,11–13,13–15] The growing scientific maturity of heterogeneous catalysis was marked by the Faraday Society's first conference devoted to the field in 1950.[16]

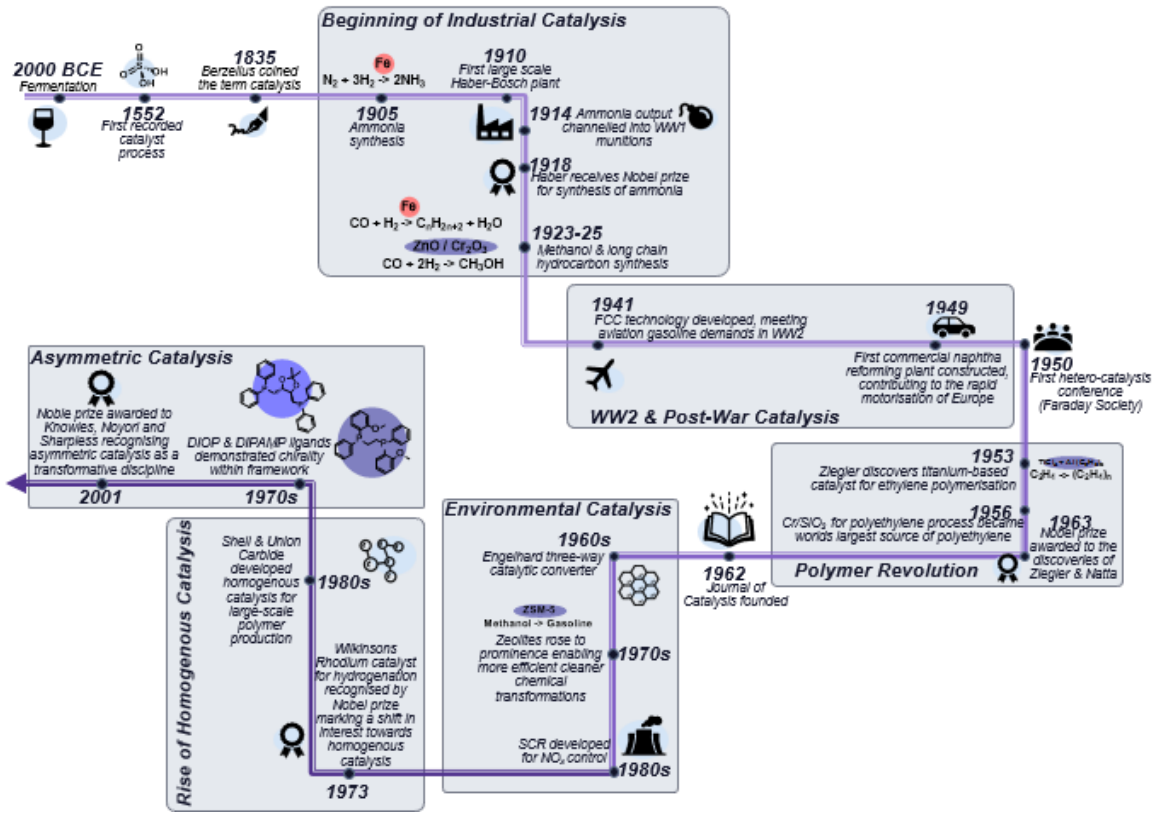

Figure 1.1: Timeline of key milestones in catalysis from its origin to the early 2000s.

As post-war demand expanded beyond fuels and petrochemicals, catalytic innova-

tion rapidly extended into polymer synthesis and materials manufacturing. Ziegler's titanium-based ethylene polymerisation system (1953) and Natta's stereospecific propylene polymerisation (1954) founded the modern plastics industry and were recognised with the 1963 Nobel Prize.[17,18] Rapid industrial uptake followed, including Phillips Petroleum's chromium catalysts for polyethylene and Ziegler-Natta systems for synthetic rubber, with the Phillips process becoming the world's largest source of polyethylene by 1956.[15,19] Several additional catalytic routes of global significance reached industry by the end of the decade.[15] Alongside these developments, catalysis consolidated as a scientific discipline and diversified beyond classical heterogeneous platforms. The launch of the *Journal of Catalysis* in 1962 and the introduction of a highly active nickel-based steam reforming catalyst marked increasing scientific growth[20] This transition accelerated with Wilkinson's soluble rhodium complex (1965), which established homogeneous catalysis for pharmaceuticals and fine chemicals and was later recognised with the 1973 Nobel Prize.[21,22] Subsequently, homogeneous catalysis was translated to industrial polymer production by Shell and Union Carbide via catalytic routes to linear low-density polyethylene.[23]

Entering the twenty-first century, asymmetric catalysis rose to prominence as the biological consequences of molecular chirality became increasingly apparent. Although early demonstrations date back to Rosenthaler's enzyme-mediated cyanohydrin formation (1908)[24] and Bredig and Fiske's prochiral transformation (1913),[25] the field gained major recognition with the 2001 Nobel Prize awarded to Knowles, Noyori, and Sharpless.[26–28] Knowles's adaptation of Wilkinson's rhodium(I) complex enabled the first efficient homogeneous asymmetric hydrogenations,[29,30] while Kagan and Dang's DIOP ligand demonstrated that ligand chirality could drive enantioselectivity.[31,32] These principles enabled widespread industrial adoption, including Monsanto's Rh-DIPAMP synthesis of L-DOPA for Parkinson's therapy,[33] Noyori's Ru-BINAP hydrogenation of olefins and ketones,[34,35] Takasago's 150-ton-per-year acetoxyazetidinone process for antibiotic synthesis,[36] and Hoffmann-La Roche's MeO-BIPHEP catalysts for vitamins and fine chemicals.[37]

1.2 Emergence of Organocatalysis

As the twentieth century drew to a close, catalysis found itself increasingly shaped by environmental imperatives and the emerging paradigm of green chemistry. Automotive emissions control drove widespread deployment of Engelhard's exhaust after-treatment systems, now the most widely used catalytic reactors globally.[38] Zeolite catalysts enabled shape-selective processes such as Mobil's methanol-to-gasoline conversion with ZSM-5 (1976) and Fe-ZSM-5-catalysed oxidation of benzene to phenol (1990).[39] Selective Catalytic Reduction (SCR) emerged in the 1980s for NO_x control in power generation and heavy-duty transport.[40] Before the turn of the millennium, most high-performance catalytic systems relied heavily on transition metals, whose effectiveness was well established but whose reliance on scarce, often toxic elements raised concerns of sustainability and safety.[41] Organocatalysis, defined as the use of small chiral organic molecules to catalyse stereoselective reactions, emerged as a compelling alternative. Its rise around the year 2000, as illustrated in Figure 1.2, was driven not only by its capacity to deliver high levels of reactivity and selectivity but also by attributes uniquely suited to the evolving needs of modern chemistry and society. Organocatalytic reactions are characterised by operational simplicity, broad functional group tolerance, and robustness under ambient conditions, often proceeding in the presence of air and water. Importantly, the catalysts themselves are stable, non-toxic, and structurally diverse, drawing on the vast repertoire of organic molecules available for design and modification. These features are synonymous to the efficiency observed in biological systems, where small organic motifs operate under mild conditions. These qualities, combined with the absence of metals, aligned organocatalysis with the principles of sustainability, offering synthetic strategies with reduced environmental burden.[41] In this sense, organocatalysis resonated strongly with the wider cultural and methodological shift towards green chemistry, a discipline that by the late twentieth century had become firmly embedded in the scientific and industrial agenda. As defined by Anastas and Warner, the twelve principles of

green chemistry established a framework for innovation aimed at minimising waste, reducing hazardous substances, and improving energy efficiency.[42–45]

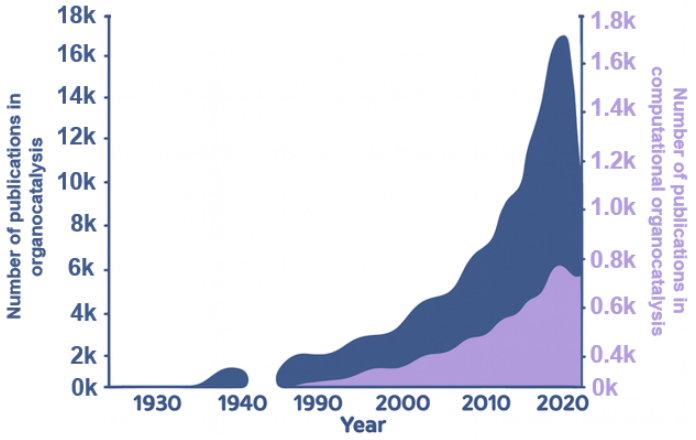

Figure 1.2: Publication of organocatalysis (blue) and computational organocatalysis (purple) papers over time.

Early asymmetric applications of organocatalysis appeared sporadically throughout the twentieth century. Bredig and Fiske reported the asymmetric HCN addition to benzaldehyde using Cinchona alkaloids in 1913, albeit with modest enantiomeric excess,[46,47] followed decades later by Pracejus's O-acetylquinine-catalysed methanolysis of ketenes in 1960[48] and Sheehan's use of chiral carbenes in asymmetric benzoin condensations.[49,50] These early demonstrations remained largely isolated and did not immediately establish a coherent field. A clear inflection point emerged in the early 1970s, as illustrated in Figure 1.3, when Eder, Sauer, and Wiechert at Schering[51] and independently Hajos and Parrish at Hoffmann-La Roche[52] demonstrated proline-catalysed intramolecular aldol cyclisations en route to steroid precursors, providing one of the first compelling examples of enzyme-like catalysis by a small organic molecule. Although these studies were initially underappreciated, they catalysed a gradual broadening of conceptual approaches through the late 1970s and 1980s, including Wynberg's development of Cinchona alkaloids as chiral bases and phase-transfer catalysts.[53–55] By the 1990s, organocatalysis had evolved into a dense and diverse landscape of strategies, with pioneering examples including Jacobsen's thiourea-catalysed Strecker reaction,[56] Miller's peptide-based catalysts,[57] Fu's chiral DMAP derivatives,[58] Shi's and Yang's ketone-based oxidation systems, Denmark's

phosphoramides,[59] and Maruoka's quaternary ammonium salt catalysts.[60] Together, these contributions formed a scattered but increasingly concentrated foundation that directly preceded the rapid expansion of organocatalysis in the early twenty-first century.

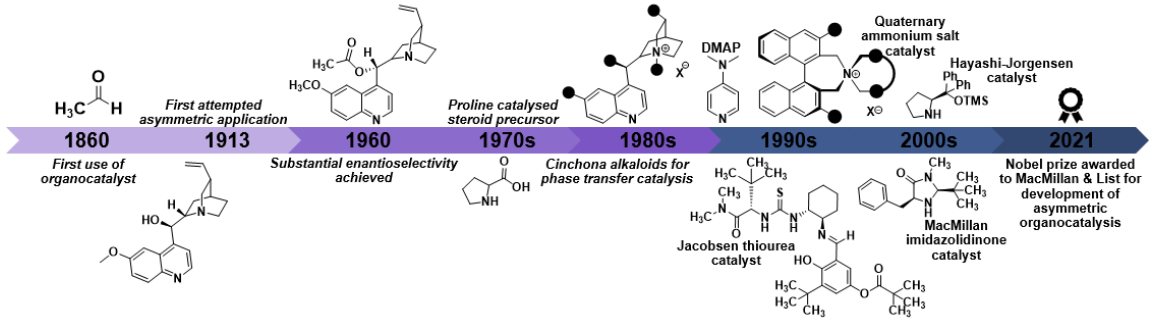

Figure 1.3: Timeline of milestones within organocatalysis from its first uses (purple) to the gold rush era and ending with the field's recognition with a Nobel Prize (blue).

This momentum culminated in the seminal, near-simultaneous reports by List and MacMillan in 2000, which triggered the rapid expansion of modern organocatalysis. List and co-workers demonstrated that the simple amino acid L-proline could mediate enamine-based aldol reactions, while MacMillan introduced imidazolidinone catalysts enabling iminium activation in Diels-Alder reactions.[61,62] Two complementary activation modes, enamine catalysis acting through Lewis base character, and iminium catalysis functioning as a Lewis acid analogue, fundamentally reshaped thinking in asymmetric synthesis by proving that small, readily available organic molecules could rival transition metals in scope and selectivity. It was in this context that MacMillan coined the term *organocatalysis*, defined as "the acceleration of a chemical transformation through the addition of a substoichiometric amount of an organic compound which does not contain a metal atom".[61] This conceptual clarity, together with the operational simplicity and sustainability inherent to organocatalysts, ignited what has since been described as the "organocatalysis gold rush".[63] The field continued to expand at remarkable speed, with both List and MacMillan extending their strategies to diverse transformations such as Mannich reactions, conjugate reductions, cycloadditions, Michael additions, and domino processes.[63–74] Crucial

contributions from others soon followed. The Jørgensen–Hayashi catalyst, based on diarylprolinol silyl ethers, emerged in 2005 as a powerful and versatile scaffold with enhanced stereoselectivity compared to proline and imidazolidinone systems.[75–77] Around the same time, MacMillan's group introduced single-electron pathways through SOMO activation, broadening the conceptual landscape of organocatalysis.[78,79] Perhaps most notably, the mergence of organocatalysis with photoredox catalysis in 2008 by MacMillan and Nicewicz demonstrated how light-driven single-electron events could be harnessed in tandem with enamine activation, opening new frontiers in sustainable catalysis.[80] The field rapidly integrated into a cornerstone of modern asymmetric synthesis, firmly establishing its place as a third pillar of catalysis, alongside transition-metal catalysis and biocatalysis.[81]

Over the past two decades, organocatalysis has sustained its momentum and established itself as a foundational discipline in modern chemistry. Its recognition with the 2021 Nobel Prize in Chemistry[82] marked not only the validation of its scientific maturity but also its establishment as one of the central paradigms in catalysis. This field's evolution is marked by the ever-expanding range of activation modes and mechanistic principles. Among the most established are enamine and iminium activation, Brønsted acid/base catalysis, nucleophilic Lewis base catalysis, hydrogen-bonding catalysis, and ion-pairing phase-transfer catalysis, as summarised in Figure 1.4. Each of these approaches enables highly enantioselective transformations across diverse substrate classes and reaction types. Beyond these classical categories, contemporary research has increasingly focused on multifunctional catalysts and synergistic systems, in which multiple activation pathways operate cooperatively within a single transformation. Such strategies, inspired in part by enzymatic catalysis, have dramatically expanded the synthetic reach and efficiency of organocatalytic methodologies. Catalysts can now be grouped according to their acid–base characteristics, or alternatively by their mode of interaction, whether they form covalent intermediates with substrates or promote reactivity through NCIs.

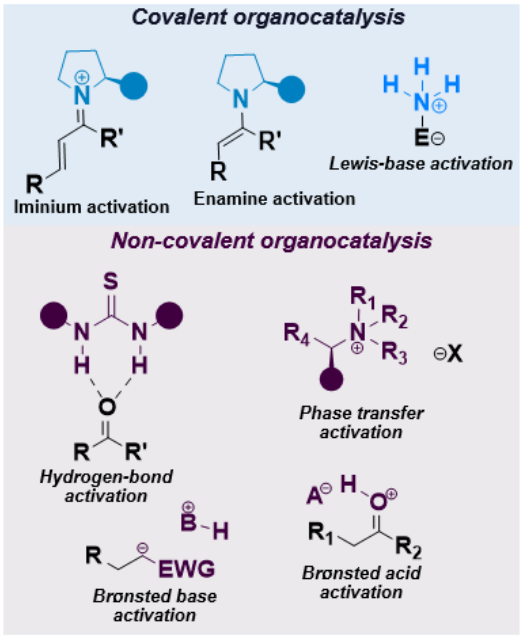

Figure 1.4: Overview of covalent (blue) and non-covalent (purple) organocatalytic activation mechanisms.

1.3 Halogen Bonding

Inspired by the success of HB in organocatalysis, attention has increasingly shifted toward XB as a parallel yet fundamentally distinct NCI with growing influence in molecular recognition, crystal engineering, and, more recently, organocatalysis.[83] XB is formally defined as *"a net attractive interaction between an electrophilic region associated with a halogen atom in a molecular entity and a nucleophilic region in another or the same molecular entity."*[84,85] Contrary to the classical perception of halogens as nucleophilic donors, XB emerges when a covalently bound halogen, most prominently iodine due to its high polarisability, develops a localised electrophilic region capable of accepting electron density.[86] This behaviour arises from the anisotropic distribution of electron density around a halogen atom when bound to an electron-withdrawing framework. As illustrated in Figure 1.5, a region of positive electrostatic potential develops along the extension of the R–X bond axis, referred to as the σ-hole, while an electron-rich belt occupies the perpendicular region.[87–94] This charge anisotropy imparts the pronounced directionality characteristic of halogen bonding, with R–X···LB angles

typically approaching linearity due to repulsive interactions between the halogen's lateral lone pairs and the Lewis base.[95] Although early experimental observations of halogen–anion interactions date back to 1819,[96] the modern theoretical foundation of XB was only established in the 1990s with the help of quantum chemical analysis of the σ-hole by Politzer and Murray.[97,98] Subsequent computational and experimental studies further validated this framework,[99,100] leading to formal IUPAC recognition in 2013.[94,101] The description of the XB continues to receive notable attention with recent work demonstrating that XB arises from a balance of electrostatics, charge transfer, polarisation, and dispersion contributions.[102–104] Direct experimental imaging of the σ-hole by Kelvin probe force microscopy in 2021 provided compelling validation of this conceptual model.[105]

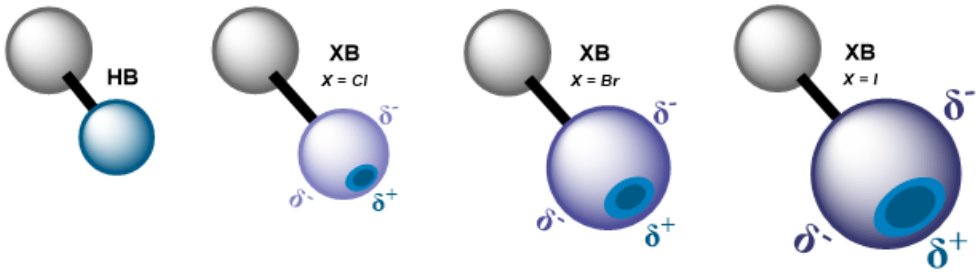

Figure 1.5: Electron poor (blue) and rich (purple) regions highlighted in HB and various XB-based scaffolds.

Although closely related to HB, XB exhibits several distinctive properties that are particularly attractive for catalyst design. XB interactions are typically more directional than XB, reflecting the spatial localisation of the σ-hole.[89,95,106] They are also highly tunable; the interaction strength varies with halogen polarisability (Cl < Br < I) as shown in Figure 1.5, alongside electron-withdrawing substitution of the donor scaffold.[84,89,106,107] As a result, iodine-based donors usually display the strongest XB interactions, while fluorine rarely functions as an effective donor.[108] In addition, XB donors possess larger van der Waals radii and higher hydrophobicity than classical HB donors, leading to enhanced solubility in nonpolar solvents and increased steric sensitivity.[89] These features allow XB to function as a hydrophobic analogue of HB,

enabling activation in low-polarity environments and with apolar substrates.[109,110] Importantly, XB donors may be neutral and apolar, in contrast to protic HB donors, opening new catalytic design space in organocatalysis where solubility, directionality, and tunability must be balanced.

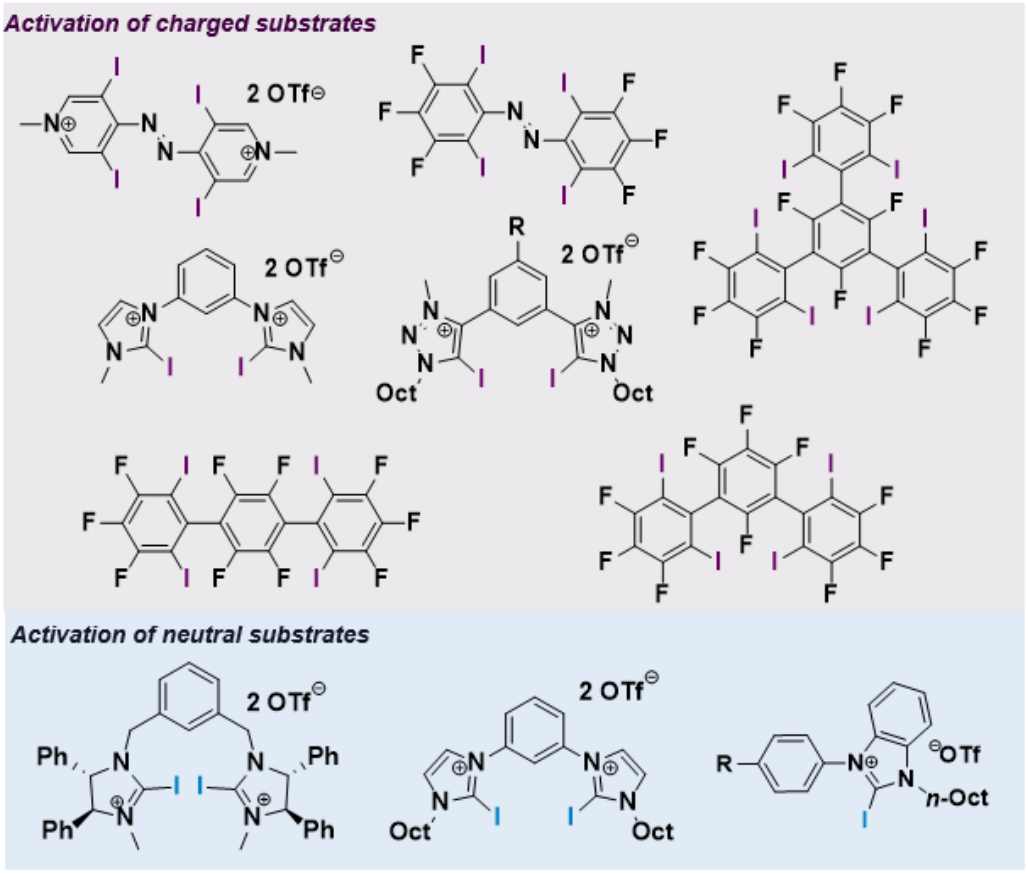

Figure 1.6: Main examples of XB-based catalytic scaffolds used in chiral organic synthesis.

As shown in Figure 1.6, XB donors typically function as Lewis-acidic activators that interact with anionic or neutral substrates and π-systems, often using cationic or polyfluorinated iodine scaffolds.[111,112] Monodentate and multidentate architectures have been explored, with multidentate systems providing enhanced binding strength, preorganisation, and transition-state stabilisation, features critical for stereocontrol.[89,106] Two major activation modes dominate XB catalysis. Anion binding and halide abstraction, where XB donors coordinate strongly to anionic leaving groups, stabilising bond cleavage and accelerating heterolytic processes.[113,114] Benchmark demonstrations include the Ritter-type solvolysis of benzhydryl bromide, activated

by imidazolium-, pyridinium-, and triazolium-based XB donors, where iodinated scaffolds showed dominant activity relative to non-halogenated analogues, highlighting the role of the XB donor in facilitating abstraction through binding to the leaving bromide ion.[108,115] Higher denticity systems further enhanced activity, though counterion effects remained unpredictable.[116,117] Neutral perfluoroaromatic donors improved solubility but displayed weaker binding, while rigid multidentate scaffolds restored catalytic efficiency.[118,119] The second major activation mode, neutral substrate activation, involves coordination of XB donors to carbonyls or heterocycles, lowering LUMO energies and stabilising charge in transition states. Crystallographic and computational studies confirmed the feasibility of XB interactions with neutral Lewis bases.[120] Early catalytic demonstrations include quinoline reductions using haloperfluoroalkanes,[121] later improved using bidentate donors.[122] XB catalysis has also been extended to polymerisation, pericyclic reactions, Michael additions, Friedel–Crafts alkylations, and Nazarov cyclisations.[119,123–128]

Asymmetric induction through halogen bonding remains a central challenge for the field.[112,129] While the strong directionality of XB enables selective functional group activation, it simultaneously imposes strict geometric constraints that complicate catalyst design and limit efficient chirality transfer due to the spatial separation between the halogen donor and the chiral scaffold. As a result, most reported asymmetric systems achieve only modest stereocontrol, including chiral bis(imidazolium) scaffolds,[130,131] neutral tetradentate iodotriazoles,[131–133] halonium(III) systems,[112,134] and monodentate iodine(III) derivatives,[131,135] as illustrated in Figure 1.8. Notably, second-generation bidentate iodine(I) donors have recently achieved up to 95% *ee* in Mukaiyama aldol reactions, demonstrating that high stereocontrol through XB alone is feasible but remains exceptional (Figure 1.7).[112,131]

Beyond asymmetric applications, XB catalysis faces additional challenges in mechanistic ambiguity, catalyst inhibition by anions, counterion effects, limited recyclability, and the synthetic complexity of multidentate scaffolds.[121,136–140] Polymer-supported XB catalysts remain scarce compared to established organic and inorganic

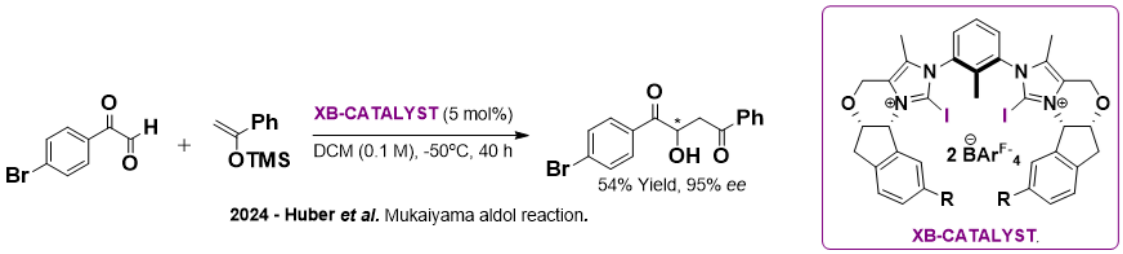

Figure 1.7: XB-catalysed Mukaiyama aldol reaction.

systems,[141,142] although early immobilised platforms have demonstrated promising recyclability.[143,144] Mechanistic understanding of XB catalysis has progressed from crystallographic validation of halogen–acceptor contacts,[115,118,122,145–152] through spectroscopic and thermodynamic measurements of binding strength,[122,153] and control experiments distinguishing XB from competing Brønsted acid or radical pathways,[115,154,155] to increasingly sophisticated computational analyses. Throughout this evolution, the σ-hole framework has remained central to rationalising donor strength, substituent effects, solvent sensitivity, and activation pathways.[107,114,156,157] Despite these advances, the complexity of NCIs limits intuition-based catalyst design, motivating the need for quantitative, computation-driven strategies capable of resolving mechanistic ambiguity, predicting selectivity, and accelerating the discovery of improved XB and related NCI-based catalysts. Modern computational modelling now enables predictive catalyst screening, mechanistic discrimination, and rational donor optimisation, directly addressing the intrinsic complexity of XB systems.

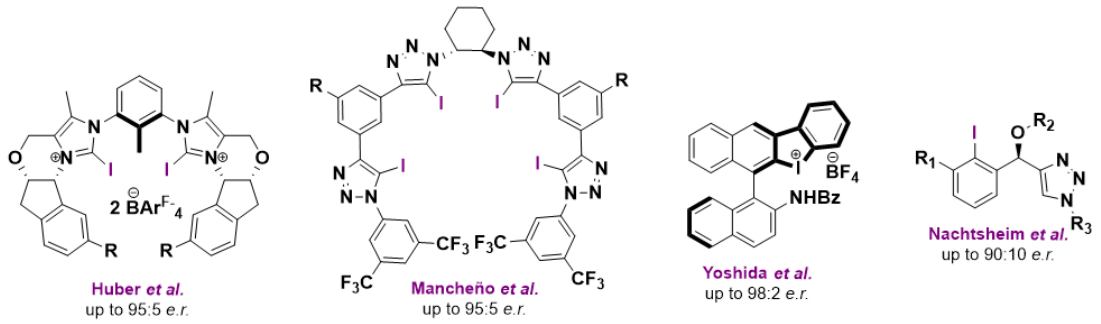

Figure 1.8: Previously reported XB-based catalytic scaffolds for asymmetric organic chemistry transformations.

1.4 Computational Design of Catalysts

The growing recognition that organocatalytic reactivity and selectivity are governed by subtle, cooperative NCIs has fundamentally reshaped strategies for catalyst discovery and optimisation. As previously noted, the interplay of electrostatics, polarisation, charge transfer, dispersion, and geometric preorganisation often exceeds the limits of qualitative chemical intuition. Quantitative computational methods have therefore become indispensable for resolving mechanistic ambiguity, rationalising structure–reactivity relationships, and guiding the deliberate design of next-generation catalysts.[158] This shift marks a broader transformation of organocatalysis from empirically driven optimisation toward predictive, model-guided discovery. As illustrated by Figure 1.9, early catalyst development relied largely on trial-and-error screening and incremental modification, but advances in electronic-structure theory, high-performance computing, and automation have dramatically expanded the scope of in silico exploration. Density functional theory (DFT) and hybrid quantum mechanical/molecular mechanical (QM/MM) approaches now enable detailed characterisation of reaction pathways, transition states, and non-covalent stabilisation effects, providing molecular-level insight into reactivity trends and stereochemical control.[158–166] Automated platforms such as ACE, AARON, and CatVS facilitate high-throughput virtual screening of catalyst libraries, accelerating hypothesis testing and reducing reliance on costly experimental trial-and-error.[167–173] Collectively, these methods enable systematic exploration of chemical space and quantitative evaluation of competing activation modes, an essential capability for systems dominated by weak but highly directional NCIs.

Machine learning (ML) has further amplified this paradigm shift by enabling data-driven prediction of catalytic performance from molecular descriptors.[174] Rather than relying solely on mechanistic intuition, ML models can identify multidimensional correlations between catalyst structure and experimentally measured outcomes, offering rapid estimates of reactivity and enantioselectivity across large

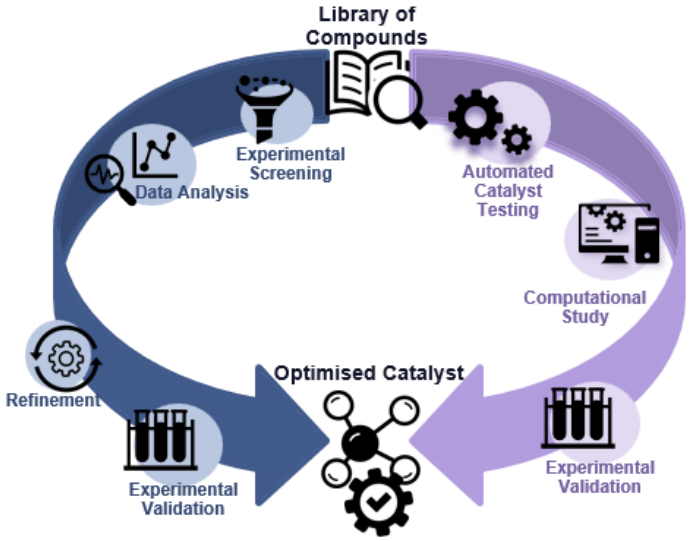

Figure 1.9: General workflow for the traditional (blue) and modern (purple) automatic approach to catalyst design.

design spaces. A notable example is provided by Denmark and co-workers, who demonstrated that averaged steric occupancy (ASO) descriptors accurately predict enantioselectivity in chiral phosphoric acid catalysis.[175] The integration of statistical learning with mechanistic modelling (Figure 1.9) increasingly enables closed-loop optimisation workflows in which candidate catalysts are computationally generated, evaluated, and prioritised prior to synthesis, significantly accelerating discovery timelines. Beyond individual catalyst optimisation, computational approaches have also facilitated the emergence of hybrid and cooperative catalytic strategies. The deliberate merging of complementary activation modes, such as enamine/iminium dual catalysis or combined organocatalytic and metal-based systems, has enabled increasingly complex, stereodivergent, and multistep transformations.[176–182] Representative examples include MacMillan's cascade iminium–enamine catalysis, Carreira's stereodivergent Ir/amine platforms, and Snaddon's Pd/benzotetramisole cooperative α-allylation strategy. Parallel advances in multifunctional catalyst design increasingly exploit multiple binding motifs within a single scaffold to achieve enzyme-like levels of selectivity and rate acceleration. Notable demonstrations include HB donor/acid co-catalysis,[183] bis-urea hydrogen-bonding phase-transfer systems for fluoride activation,[184] and cooperative catalysts that integrate hydrogen bonding with Lewis or

Brønsted acid activation. More recently, attention has expanded toward emerging σ-hole interactions, namely halogen bonding (XB), chalcogen bonding (ChB), and pnictogen bonding (PnB), as orthogonal tools for molecular activation and catalyst design.[185,186] These interactions offer distinctive directionality, tunable Lewis acidity, and complementary solvation characteristics relative to classical HB, but also introduce heightened sensitivity to geometry, electronics, and environmental effects. As a result, computational modelling plays a uniquely critical role in disentangling competing interaction pathways, quantifying stabilisation energies, and rationally engineering donor architectures capable of delivering reliable and selective catalysis. The convergence of electronic-structure modelling, automation, machine learning, and NCI-focused catalyst engineering has transformed organocatalysis into a predictive and increasingly data-driven discipline. This computationally enabled framework provides the foundation for addressing the mechanistic complexity and design challenges inherent to XB catalysis, and directly motivates the computational strategy adopted in this thesis.

1.5 Aims and Objectives

The emergence of XB as a distinct NCI in organocatalyst design, often compared with the HB, has revealed a fundamentally greater degree of tunability, as the electronic and steric properties of the XB donor can be modulated through scaffold design, substituent effects, and XB-donor identity, a level of control that is far less accessible in HB-based systems. In addition to its pronounced directionality, XB exhibits notable mechanistic versatility, enabling diverse modes of activation, including anion binding, leaving-group abstraction, polarisation of electrophiles, and stabilisation of charged or high-energy intermediates, thereby expanding the scope of catalytic transformations accessible through NCIs.[89,107,113,187,188] Despite the rapidly growing experimental interest,[89] the structure–reactivity relationships, operative activation modes, and environmental merits of XB organocatalysis remain insufficiently charac-

terised.

This thesis aims to establish a rigorous and transferable computational framework for understanding XB-based catalytic reactivity. Through detailed quantum chemical analysis, the overarching goal is to deliver quantitative mechanistic insight and extract rational design principles to guide the next generation of XB organocatalysts, with a particular emphasis on prospective asymmetric applications.

To establish this foundation, an extensive series of computational studies was undertaken, beginning with a systematic investigation of electronically activated monovalent XB scaffolds.[125] Chapter 3, Monovalent XB-Based Scaffolds, examines how donor identity, scaffold geometry, and substituent orientation govern σ-hole magnitude, accessibility, and directionality, thereby defining the structural parameters that control XB strength and thermodynamic feasibility. Particular emphasis was placed on contrasting classical O-type activation with the recently proposed π-type activation mode[157] in the Michael addition of indole to *trans*-crotonophenone (Figure 1.10). Molecular iodine was incorporated as a minimalistic reference system to probe fundamental aspects of XB-mediated catalysis.[154] Together, these studies reveal the mechanistic diversity inherent to XB activation and challenge the assumption of a single universal pathway.

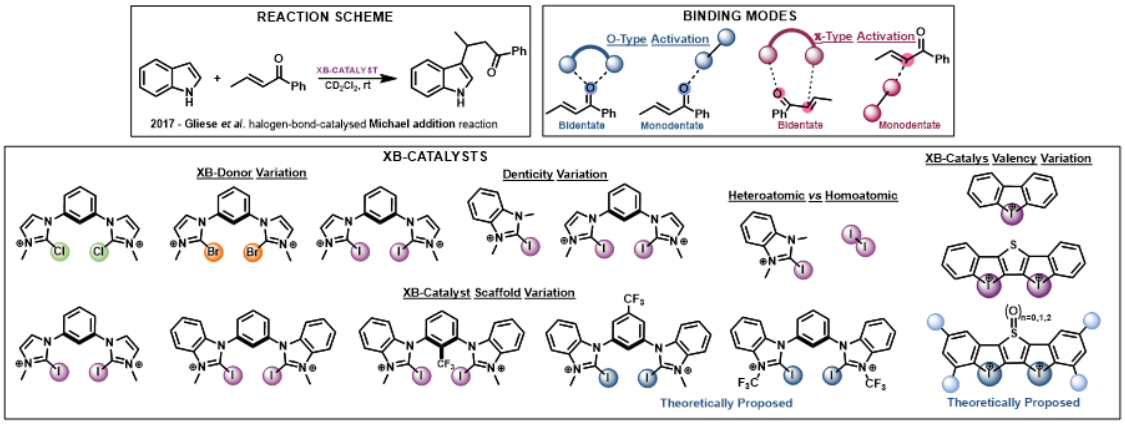

Figure 1.10: Framework of the XB-catalyst stabilised Michael addition reaction.

Building upon this mechanistic platform, the scope of XB catalysis was extended

beyond small-molecule transformations to the ring-opening polymerisation (ROP) of L-lactide, thereby evaluating the transferability of XB activation principles to macromolecular systems of industrial and biomedical relevance.[189] The influence of catalyst–substrate orientation and base-mediated activation on polymerisation behaviour was analysed to assess the robustness and adaptability of XB-mediated control (Figure 1.11).

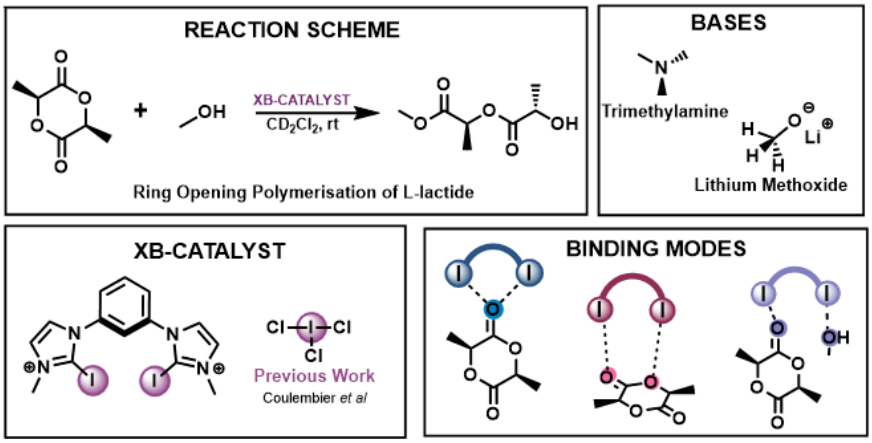

Figure 1.11: Framework of the XB-catalyst stabilised ring-opening polymerisation of L-lactide.

In Chapter 4, Hypervalent XB-Based Scaffolds, the investigation is extended from monovalent to hypervalent iodine(III) XB architectures, introducing enhanced Lewis acidity, structural rigidity, and dual σ-hole cooperativity.[190–194] Both O-type and π-type activation modes within the hypervalent scaffolds were examined,[157] alongside systematic scaffold modulation through targeted substituent variation and oxidation-state control. These studies clarify how inductive, mesomeric, and steric effects collectively govern reactivity–selectivity relationships and unify monovalent and hypervalent XB donors within a coherent mechanistic framework.

A further layer of complexity arises from secondary intramolecular interactions and counterions in realistic XB catalysts.[125] In Chapter 5, Counterion-Induced Conformational Effects in Catalysis, bifunctional cationic systems incorporating HB donor motifs were investigated to evaluate hydrogen bond–enhanced halogen bonding (HBeXB) effects on XB strength and directionality.[154,157,195] In parallel, counterion

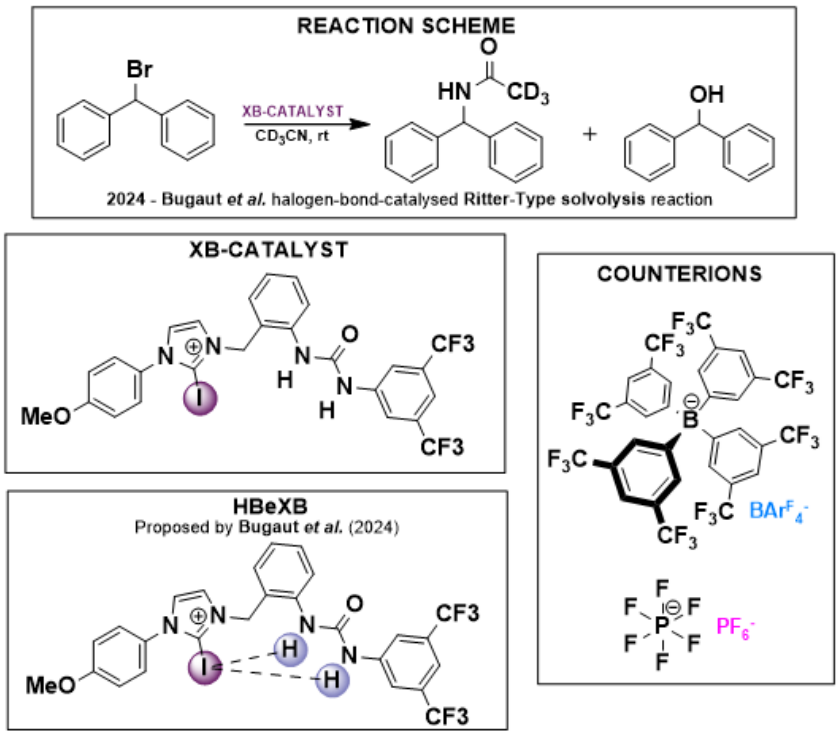

Figure 1.12: Framework of the XB-catalyst stabilised Ritter-type solvolysis reaction.

effects were systematically assessed in a Ritter-type solvolysis reaction to quantify how ion size and coordinating ability, PF_6^- vs. $BarF_4^-$, modulate catalyst conformation, σ-hole accessibility, substrate binding energetics, and overall free-energy profiles (Figure 1.12). These results highlight the necessity of explicitly accounting for counterions and cooperative interactions in computational modelling and catalyst design.

Collectively, these studies establish a unified computational framework linking electronic structure, activation mode, scaffold architecture, and environmental effects in XB organocatalysis. The resulting design principles position halogen bonding as a versatile platform for rational catalyst development, providing a foundation for future advances, particularly in asymmetric XB catalysis.

2 Computational Theory

2.1 Quantum Chemistry

The field of theoretical chemistry has experienced remarkable growth through its increasing integration with experimental studies across all branches of chemistry, in both justification and iterative collaboration. Notably, the scope of theoretical approaches was constrained by the available computational resources. However, recent advances in computational power, coupled with the development of sophisticated quantum methodologies, have enabled chemists to investigate previously inaccessible systems, continuously pushing the boundaries of the ever-evolving field.

A pivotal milestone in the formulation of quantum mechanics was achieved by Louis-Victor de Broglie in 1923,[196], who extended the concept of wave-particle duality from light to all matter. He proposed that every particle with momentum p possesses an associated wavelength λ, which can be expressed as:

$$\lambda = \frac{c}{\nu} = \frac{2\pi c}{\omega} = \frac{2\pi\hbar}{p} \tag{1}$$

Building upon this idea, Erwin Schrödinger later argued that particles exhibiting wavelike behaviour should be described by a wavefunction, leading to one of the foundational equations of quantum mechanics, the Schrödinger Equation (SE):[197]

$$i\hbar\frac{\partial\Psi}{\partial t} = -\frac{\hbar^2}{2m}\left(\frac{\partial^2\Psi}{\partial x^2} + \frac{\partial^2\Psi}{\partial y^2} + \frac{\partial^2\Psi}{\partial z^2}\right) + U(x,y,z)\Psi = \hat{H}\Psi \tag{2}$$

When relativistic effects are neglected and atomic units are used ($\hbar = m_e = e = c = 1$), the non-relativistic time-dependent Schrödinger Equation (TDSE) for a quantum system can be written as a function of electron coordinates (r_i), nuclear coordinates (R_i), and space-spin coordinates $x_i = (r_i, \eta_i)$, with the Hamiltonian $\hat{H}(r_i, R_i, t)$ and wavefunction $\Psi(r_i, R_i, t)$:

$$i\hbar\frac{\partial}{\partial t}\Psi(x_i, R_i, t) = \hat{H}(r_i, R_i, t)\,\Psi(x_i, R_i, t) \tag{3}$$

In most chemical applications, systems are considered at stationary points, allowing the removal of the time dependence and resulting in the time-independent Schrödinger Equation (TISE):

$$\hat{H}\Psi = E\Psi \tag{4}$$

Here, $\hat{H}$ denotes the total energy of the system, composed of the kinetic energy of electrons ($\hat{T}_e$) and nuclei ($\hat{T}_n$), the electron-electron ($\hat{V}_{ee}$) and nucleus-nucleus ($\hat{V}_{nn}$) repulsions, and the electron-nucleus Coulomb attraction ($\hat{V}_{\text{ext}}$):

$$\begin{aligned}\hat{H} &= -\sum_{i=1}^{N}\frac{\hbar^2}{2}\nabla_i^2 - \sum_{A=1}^{M}\frac{\hbar^2}{2m_A}\nabla_A^2 + \sum_{i=1}^{N}\sum_{j>i}^{N}\frac{1}{r_{ij}} + \sum_{i=1}^{N}\sum_{j>i}^{M}\frac{Z_A Z_B}{R_{ij}} - \sum_{i=1}^{N}\sum_{A=1}^{M}\frac{Z_A}{r_{iA}} \\ &= \hat{T}_e + \hat{T}_n + \hat{V}_{ee} + \hat{V}_{nn} + \hat{V}_{\text{ext}}\end{aligned} \tag{5}$$

Despite its generality, the Schrödinger Equation cannot be solved exactly for systems with more than two particles. Exact solutions are limited to hydrogen-like atoms or single-electron ions, a challenge known as the many-body problem. To address this, Max Born and Julius Robert Oppenheimer introduced the Born-Oppenheimer

approximation (BOA) in 1927. This approximation exploits the large mass disparity between electrons and nuclei, which permits the separation of electronic and nuclear contributions in both the Hamiltonian and wavefunction:

$$\hat{H} = \hat{H}_{\text{elec}} + \hat{H}_{\text{nuc}} = \hat{T}_e + \hat{V}_{ee} + \hat{V}_{\text{ext}} + \hat{V}_{nn} \tag{6}$$

$$\Psi(\mathbf{r}, \mathbf{R}) = \Phi(\mathbf{r}, \mathbf{R})\, \chi(\mathbf{R}) \tag{7}$$

Within this framework, the nuclear kinetic energy $\hat{T}_n$ is neglected, the nuclear repulsion term $\hat{V}_{nn}$ is treated as constant, and the electronic wavefunction Φ depends parametrically on the nuclear positions $\mathbf{R}$, while the nuclear wavefunction χ depends solely on $\mathbf{R}$. This separation significantly simplifies the study of molecular systems in quantum chemistry.

Nonetheless, separating the electronic and nuclear components of the SE alone does not suffice to solve the many-body problem. To make the problem tractable, a series of assumptions, approximations, and idealisations must be introduced. In 1927, Douglas Rayner Hartree proposed the *Self-Consistent Field* (SCF) method[198], wherein the motion of one electron, e_1, is described within the mean potential generated by the nucleus together with the remaining electron, e_2. This approach yields an effective Hamiltonian, $\hat{H}_1^{\text{eff}}$, for electron e_1:

$$\hat{H}_1^{\text{eff}}\, \Psi_1(\mathbf{r}) = E_1\, \Psi_1(\mathbf{r}) \tag{8}$$

To achieve an exact solution for accuracy, the variational principle must be integrated:

$$\Psi_{\text{trial}}^{*}\, \hat{H}\, \Psi_{\text{trial}} = E_{\text{trial}} \geq E_{\text{min}} \langle \Psi | \hat{H} | \Psi \rangle \tag{9}$$

In the case of larger N-electron systems, the exact wavefunction becomes computationally intractable, and is therefore approximated as a product of N individual electron functions, a construction known as the Hartree product:

$$\Psi(\mathbf{r}_1, \mathbf{r}_2, \ldots, \mathbf{r}_N) = \psi_1(\mathbf{r}_1)\,\psi_2(\mathbf{r}_2)\,\ldots\,\psi_N(\mathbf{r}_N) = \prod_{i=1}^{N} \psi_i(\mathbf{r}_i) \tag{10}$$

Furthermore, to account for the Pauli exclusion principle in line with the fermionic properties of electrons, antisymmetric functions are applied. Consequently, following Hartree's approximation, Vladimir A. Fock and John C. Slater proposed the Slater determinant[199,200], conveying the wavefunction as the determinant of a matrix of one-electron wavefunctions:

$$\Phi_0(\mathbf{r}_1, \mathbf{r}_2, \ldots, \mathbf{r}_N) = \frac{1}{\sqrt{N!}} \begin{vmatrix} \phi_1(\mathbf{r}_1) & \phi_2(\mathbf{r}_1) & \cdots & \phi_N(\mathbf{r}_1) \\ \phi_1(\mathbf{r}_2) & \phi_2(\mathbf{r}_2) & \cdots & \phi_N(\mathbf{r}_2) \\ \vdots & \vdots & \ddots & \vdots \\ \phi_1(\mathbf{r}_N) & \phi_2(\mathbf{r}_N) & \cdots & \phi_N(\mathbf{r}_N) \end{vmatrix} \tag{11}$$

Alongside the Fock operator:

$$\hat{F}(\mathbf{r}) = \hat{h}_i(\mathbf{r}) + \sum_j \left(\hat{J}_j(\mathbf{r}) - \hat{K}_j(\mathbf{r})\right) \tag{12}$$

The SE was rewritten and solved using the Hartree-Fock (HF) method:

$$\hat{F}(\mathbf{r})\,\phi_0(\mathbf{r}) = E_0\,\phi_0(\mathbf{r}) \tag{13}$$

The Fock operator, $\hat{F}(\mathbf{r})$, is constructed from three main contributions: the one-electron Hamiltonian, $\hat{h}_i(\mathbf{r})$, which accounts for the kinetic energy and the interaction between electrons and nuclei, the Coulomb operator, $\hat{J}_i(\mathbf{r})$, describing electron–electron repulsion, and the exchange operator, $\hat{K}_i(\mathbf{r})$, which arises from the

antisymmetry of the wavefunction. Although the HF approximation provides a useful framework for electronic structure calculations, it does not yield the exact electronic energy of a system because a single Slater determinant neglects electron correlation. To address this limitation, various post-HF approaches have been developed. These include Möller–Plesset (MP) perturbation theory,[201] Configuration Interaction (CI),[202–204] and Coupled Cluster (CC) theory.[205–207]

2.2 Density Functional Theory

The DFT is an alternative approach to wave-function methods previously proposed, which expresses the ground-state (GS) energy of a system as a functional of the electronic density, $\rho(\mathbf{r})$, rather than the many-electron wavefunction. This establishes a direct relationship between the ground-state wavefunction, Ψ_{GS}, and the corresponding electron density in an N-electron system, leading to the following expression for the ground-state energy:

$$E_0 = \int \cdots \int \left[\Psi^*(\mathbf{r}_1, \mathbf{r}_2, \ldots, \mathbf{r}_N)\, \hat{H}\, \Psi(\mathbf{r}_1, \mathbf{r}_2, \ldots, \mathbf{r}_N)\, d\mathbf{r}_3 \ldots d\mathbf{r}_N \right] \tag{14}$$

The nuclear kinetic energy can be neglected by splitting the new Hamiltonian into different parts, as per the Born-Oppenheimer approximation:

$$\hat{H}_{\mathrm{el}}(\mathbf{r}, \mathbf{R}) = \hat{T}(\mathbf{r}) + \hat{V}(\mathbf{r}) + \hat{V}(\mathbf{R}) + \nu(\mathbf{r}) \tag{15}$$

Leading the description of the Hamiltonian as the total energy of a system expressed as the sum of several contributions: the electronic kinetic energy, $\hat{T}(\mathbf{r})$, the Coulomb repulsion between electrons, $\hat{V}(\mathbf{r})$, the Coulomb repulsion between nuclei, $\hat{V}(\mathbf{R})$, and the electron–nucleus Coulomb attraction, $\nu(\mathbf{r})$, which is commonly referred to as the external potential. By substituting this modified Hamiltonian into the ground-state energy expression, the first three contributions can be grouped into the

so-called *universal functional*, $F[\rho(\mathbf{r})]$, which is distinct from the external potential, $v(\mathbf{r})$, yielding the following expression for the total energy:

$$E_0 = \int \cdots \int F_x[\rho(\mathbf{r})] + \int_{-\infty}^{\infty} \rho(\mathbf{r})\, v(\mathbf{r})\, d\mathbf{r} \tag{16}$$

While wavefunction-based methods struggle with multi-electron equations, the challenge in density-based approaches is determining the exact electron density, which corresponds to the system's minimum energy. To simplify this, Kohn and Sham proposed[208], expressing the total density as a sum of orbital densities:

$$F_x[\rho(\mathbf{r})] = \hat{T}[\rho(\mathbf{r})] + \frac{1}{2} \int \int \frac{\rho(\mathbf{r}_1)\, \rho(\mathbf{r}_2)}{|\mathbf{r}_1 - \mathbf{r}_2|}\, d\mathbf{r}_1\, d\mathbf{r}_2 + E_{XC}[\rho(\mathbf{r})] \tag{17}$$

This functional can be decomposed into three components: the electronic kinetic energy, $\hat{T}[\rho(\mathbf{r})]$, which remains unchanged; the classical electron–electron repulsion expressed in terms of the density, $\frac{1}{2} \iint \frac{\rho(\mathbf{r}_1)\, \rho(\mathbf{r}_2)}{|\mathbf{r}_1 - \mathbf{r}_2|}\, d\mathbf{r}_1 d\mathbf{r}_2$; and the exchange-correlation energy, $E_{\mathrm{XC}}[\rho(\mathbf{r})]$, accounting for exchange and correlation effects among electrons with the same spin. The system is described by a set of non-interacting orbitals, known as Kohn–Sham orbitals, which comply with the corresponding Schrödinger equation:

$$\hat{H}_{\mathrm{KS}}\, \Phi_i^{\mathrm{KS}}(\mathbf{r}_i) = \varepsilon_i\, \Phi_i^{\mathrm{KS}}(\mathbf{r}_i) \tag{18}$$

2.2.1 Functionals

One of the earliest and most widely used approximations in DFT is the Local Density Approximation (LDA). In this framework, the exchange–correlation (XC) energy at a point in space is assumed to behave like that of a uniform electron gas with the same local electron density.[209–211] The total XC energy is obtained by evaluating the electron density on a spatial grid and integrating the corresponding local XC energy

density:

$$E_{\mathrm{XC}}^{\mathrm{LDA}}[\rho] = E_{\mathrm{X}}^{\mathrm{LDA}}[\rho] + E_{\mathrm{C}}^{\mathrm{LDA}}[\rho]. \tag{19}$$

The exchange component is known analytically from Dirac's[212] uniform electron gas expression:

$$E_{\mathrm{X}}^{\mathrm{LDA}}[\rho] = -\frac{3}{2}\left(\frac{3}{\pi}\right)^{1/3} \int \rho(\mathbf{r})^{4/3}\, d\mathbf{r}. \tag{20}$$

The correlation term historically lacked a closed-form expression and was therefore represented through parametrisations based on quantum Monte Carlo data.[213] A commonly used analytical form is:

$$E_{\mathrm{C}}^{\mathrm{LDA}}[\rho] = \ln\left(1 + \frac{b}{r_s} + \frac{b}{r_s^2}\right), \tag{21}$$

Where a and b are constants fitted at the MP2 level, and $r_s = \left(\frac{3}{4\pi\rho}\right)^{1/3}$ is the Wigner–Seitz radius.[214]

An extension of the LDA, known as the Local Spin-Density Approximation (LSDA), treats the spin-up (ρ^α) and spin-down (ρ^β) densities separately, making it suitable for open-shell systems.[215]

$$E_{\mathrm{XC}}^{\mathrm{LSDA}}[\rho^\alpha] = E_{\mathrm{X}}^{\mathrm{LSDA}}[\rho^\alpha] + E_{\mathrm{C}}^{\mathrm{LSDA}}[\rho^\alpha, \rho^\beta] = E_{\mathrm{X}}^{\mathrm{LSDA}}[\rho^\alpha] + \int \rho^\alpha(\mathbf{r})\, R_{\mathrm{C}}[\rho^\alpha, \rho^\beta]\, d\mathbf{r}. \tag{22}$$

LDA performs well for systems with slowly varying electron densities, such as solids. However, its local nature also introduces notable limitations, including the systematic over-binding of molecules and the underestimation of bond lengths. These shortcomings highlighted the need for more flexible and accurate descriptions

of the exchange–correlation energy.

A step forward was the development of gradient-dependent approaches. The exact form of the exchange–correlation potential, v_{XC}, remains unknown, and a hierarchy of increasingly sophisticated approximations has been constructed to make practical use of DFT. Among these, the Generalised Gradient Approximation (GGA) has become one of the most widely adopted.[216–218] GGAs incorporate not only the local electron density but also its spatial gradient, enabling a more nuanced treatment of systems where the electronic density varies significantly:

$$E_{\text{xc}}^{\text{GGA}}[\rho] = \int f(\rho(\mathbf{r}), \nabla\rho(\mathbf{r}), x)\ d\mathbf{r}, \quad x = |\frac{\nabla\rho}{\rho^{4/3}}|. \tag{23}$$

While GGAs such as Perdew-Burke-Ernzerhof (PBE) and B3LYP broaden the applicability of DFT, they still provide an incomplete description of long-range correlation and dispersion. Further refinements include the meta-GGA functionals, which additionally depend on the kinetic energy density, $\tau(\mathbf{r})$, and the Laplacian of the density, $\nabla^2\rho(\mathbf{r})$:

$$E_{\text{xc}}^{\text{meta-GGA}}[\rho] = \int f(\rho(\mathbf{r}), \nabla\rho(\mathbf{r}), \tau(\mathbf{r}))\ d\mathbf{r}, \quad \tau(\mathbf{r}) = \tfrac{1}{2}\sum_{i=1}^{N_{\text{occ}}} |\nabla\varphi_i(\mathbf{r})|^2 \tag{24}$$

Functionals such as M06-2X fall into this category; M06-2X is a hybrid meta-GGA that incorporates 32 empirically optimised parameters and includes a significantly larger fraction of non-local exchange (54% HF exchange), enabling substantially improved performance for main-group thermochemistry and noncovalent interactions.[219]

Building on the concept of the adiabatic connection,[220–222] GGAs have been combined with a fraction of exact exchange, giving rise to a new class of functionals known as hybrid-GGAs. These functionals are particularly popular as they achieve a reasonable compromise between computational efficiency and accuracy. A general expression for a hybrid functional is:

$$E_{\mathrm{XC}}^{\mathrm{hybrid}} = a_{\mathrm{x}} E_{\mathrm{X}}^{\mathrm{HF}} + (1 - a_{\mathrm{x}}) E_{\mathrm{X}}^{\mathrm{DFT}} + E_{\mathrm{C}}^{\mathrm{DFT}}. \tag{25}$$

Where a_{x} determines the fraction of exact exchange included. Among them, the B3LYP functional, proposed by Becke,[223] has become one of the most widely used methods in quantum chemistry. Its popularity stems from its ability to provide reliable results at a significantly lower cost than more demanding post-HF approaches. Nevertheless, B3LYP provides a poor depiction of long-range interactions because it lacks an explicit treatment of dispersion forces and includes only a limited fraction of exact exchange. Resulting in the poor description of NCIs, it systematically underestimates binding in studies where long-range correlation such as van der Waals play a central role.[224] A complementary strategy is to enhance existing functionals with dispersion corrections. Grimme's DFT-D3 model[225] adds an explicit atom–atom dispersion potential:

$$E_{\mathrm{disp}} = -\sum_{A>B} \sum_{n=6,8,\ldots} s_n, \frac{C_n^{AB}}{R_{AB}^n}, f_n(R_{AB}), \quad f_n(R_{AB}) = \left[1 + 6\left(\frac{R_{AB}}{s_{r,n} R_0^{AB}}\right)^{-\alpha_n}\right]^{-1}. \tag{26}$$

Here, C_n^{AB} denotes the mean isotropic dispersion coefficient for atom pair AB, and R_{AB} is the interatomic distance. The parameters s_n act as scaling factors, while $f_n(R_{AB})$ is a damping function designed to prevent unphysical divergences at short range. When applied to hybrid functionals such as B3LYP, this dispersion correction substantially improves the accuracy for systems where long-range interactions are essential. The ωB97XD functional is another example of a hybrid-GGA functional which combines range separation with an empirical dispersion model, thereby improving the treatment of both long-range exchange and van der Waals interactions.[226]

Double-hybrid functionals[227] combine the strengths of DFT with elements of cor-

related wavefunction theory. While hybrid functionals integrate a fixed fraction of exact HF exchange with DFT exchange and correlation, double hybrids introduce an additional term that accounts for dynamical correlation through a perturbative second-order (PT2) contribution, typically analogous to MP2. This extension significantly enhances the description of thermochemistry, NCIs, and reaction barrier heights, often bringing the accuracy close to that of post-HF methods while maintaining substantially lower computational cost. A general form of the double-hybrid exchange–correlation energy can be written as:

$$E_{\mathrm{XC}}^{\mathrm{DH}} = a_{\mathrm{x}} E_{\mathrm{X}}^{\mathrm{HF}} + (1 - a_{\mathrm{x}}) E_{\mathrm{X}}^{\mathrm{DFT}} + (1 - a_{\mathrm{c}}) E_{\mathrm{C}}^{\mathrm{DFT}} + a_{\mathrm{c}} E_{\mathrm{C}}^{\mathrm{PT2}}, \tag{27}$$

Where a_{x} determines the proportion of exact exchange and a_{c} scales the perturbative correlation term. The introduction of the PT2 component places double hybrids at the top of the ladder, as they simultaneously reduce self-interaction error, improve long-range correlation, and offer a more accurate, physically grounded description of dispersion compared with lower-rung functionals.

2.2.2 Basis Sets

To apply the variational method for solving the Schrödinger equation, a suitable trial wavefunction must be chosen. A common approach is the Linear Combination of Atomic Orbitals (LCAO),[228], where the molecular orbital ϕ is expressed as a linear combination of basis functions Ψ_μ with optimised coefficients $c_{\mu i}$:

$$\varphi_i(\mathbf{r}) = \sum_{\mu=1}^{N_{\mathrm{AO}}} c_{\mu i}\, \Psi_\mu(\mathbf{r}; \mathbf{R}_\mu) \tag{28}$$

Since the exact form of Ψ_μ is unknown, these are represented by basis sets. Early attempts used Slater-type orbitals (STO), which resemble hydrogenic eigenfunctions:

$$\eta^{\mathrm{STO}}_{n,l,m}(\mathbf{r}) = N\, r^{\,n-1} e^{-\zeta r}\, Y^{m}_{l}(\theta,\phi) \tag{29}$$

Although STOs provide a good physical description, they are computationally demanding because two-electron integrals cannot be solved analytically, restricting their use to semi-empirical methods. To address this, Gaussian-type orbitals (GTOs) were later introduced.[229] Their functional form, $e^{-\alpha r^2}$, allows analytical evaluation of integrals:

$$\eta^{\mathrm{GTO}}_{n_x,n_y,n_z}(\mathbf{r}) = x^{n_x} y^{n_y} z^{n_z}\, e^{-\alpha r^2} \tag{30}$$

However, a single GTO poorly represents orbital behaviour near the nucleus. This limitation is overcome by combining multiple primitive Gaussians into contracted Gaussian functions (CGFs):

$$\eta^{\mathrm{CGO}}_{\tau} = \sum_{a} d^{\tau}_{a}\, \eta^{\mathrm{GTO}}_{a} \tag{31}$$

This describes and replicates the behavior of orbitals with much greater accuracy and has been extensively incorporated in the development of modern basis sets.[230–232]

Further investigations into basis set design led to the development of split-valence basis sets, in which core and valence electrons are treated differently. Core electrons, tightly bound and largely unaffected by interatomic interactions, are typically described by a single basis function. Valence electrons, however, require greater flexibility, often necessitating multiple basis functions along with diffuse and polarisation functions to capture their behaviour accurately. Diffuse functions extend the reach of the orbitals farther from the nucleus, which is essential for properly modelling anionic species and systems with long-range or weak NCIs. Polarisation functions introduce higher-angular-momentum orbitals that allow desymmetrisation of the

atomic orbitals, providing a more accurate representation of bonding, particularly in polarised covalent bonds and interactions governed by subtle NCIs. Together, these enhancements enable a detailed and reliable description of electronic structure across a wide range of chemical environments.

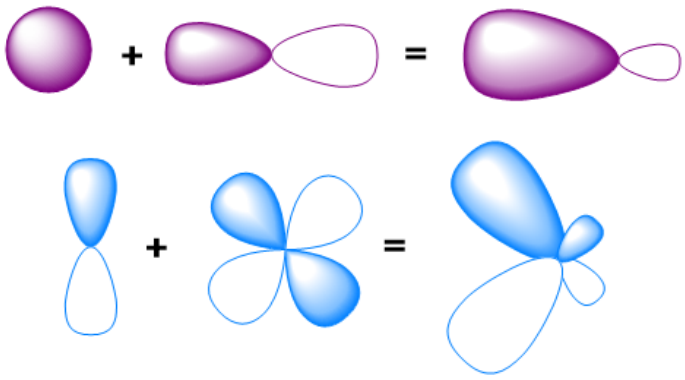

Figure 2.1: Conceptualised depiction of polarisation of a s basis function by a p basis function (purple) and polarisation of a p basis function by a d basis function (blue).

Several well-established families of basis sets fall into this category, including the split-valence Pople basis sets,[233,234], the correlation-consistent (cc) basis sets introduced by Dunning and coworkers,[235] and the Karlsruhe-type basis sets.[236] Each of these families employs its own system of nomenclature, designed to convey the number of functions included and the way they are constructed.

Pople-type basis sets,[230–232] use a compact numerical notation to signify how many primitive Gaussians describe the core and valence orbitals, and how the valence space is split to enhance flexibility. For instance, 6-311G[237] is an example of a triple-ζ split-valence basis set, the leading 6 describes the core orbital represented by a contraction of six primitive Gaussians. The 311 component specifies the split-valence space, one valence shell is formed from a contraction of three primitives, followed by two additional valence shells that each consist of a single primitive. In Pople's notation, diffuse augmentation is signaled by the addition of one or more + symbols in front of the G. A single + marks the inclusion of diffuse functions on non-hydrogen atoms, while ++ indicates the addition of diffuse functions to hydrogen atoms. Polarisation functions are denoted separately by asterisks appended to the basis-set label, a

singular * means that only the heavier elements are assigned polarisation functions, whereas ** extends these functions to the hydrogen atom. Consequently, a double-ζ split-valence basis set that incorporates both diffuse and polarisation functions on all atoms would be written as 6-31++G**. This layered description provides greater flexibility for modeling polarisation and charge redistribution.

Dunning introduced the cc basis sets. As examplified by cc-pVDZ (cc, polarised valence double-ζ) uses two basis functions for each valence orbital and includes a balanced set of polarisation functions specifically designed to recover electron correlation in a controlled manner. Higher members of the series, cc-pVTZ, cc-pVQZ, and beyond, systematically enlarge the basis by adding additional angular momentum shells, allowing smooth convergence toward the complete basis set limit. These features make Dunning basis sets especially valuable in high-accuracy quantum chemical calculations and provide a useful contrast to the more compact Pople-type constructions.

Of particular relevance to the methods applied in this thesis are the Karlsruhe basis sets, which adopt the notation $def2-NVP(D)$. In this scheme, N specifies the level of split-valence character (for example, TZ for triple-ζ, QZ for quadruple-ζ, and so forth), while the letters P and D denote the inclusion of polarisation and diffuse functions, respectively. The treatment of polarisation functions is further distinguished by the way they are applied: writing (P) indicates that only heavy atoms are supplemented, P denotes a single set of polarisation functions for all atoms, and PP refers to the use of two sets of polarisation functions across all atoms. This structured naming convention makes it straightforward to identify both the flexibility of the valence space and the extent to which additional functions are used to capture more subtle electronic effects.

2.3 NCIs Characterisation Methods

2.3.1 Quantum Theory of Atoms in Molecules

The Quantum Theory of Atoms in Molecules (QTAIM)[238–240] provides a framework for analysing the topology of the electron density distribution, $\rho(x, y, z)$, to extract a range of atomic and molecular properties. Through this analysis, one can determine the connectivity within a molecule, which is represented by line paths (previously referred to as bond paths). These line paths are associated with chemical bonds as well as with various NCIs[241]. Another important outcome of QTAIM analysis is the identification of Critical Points (CPs), defined as positions in space where the gradient of the density, $\nabla\rho$, vanishes. The nature of each CP is classified according to the curvature of the electron density at that point. The analysis is carried out by evaluating the eigenvalues $(\lambda_1, \lambda_2, \lambda_3)$, constructed from the second partial derivatives of the electron density at each point in space $\frac{\partial^2\rho}{\partial x^2}$, of the Hessian matrix $H(\rho)$:

$$H(\rho) = \begin{pmatrix} \frac{\partial^2\rho}{\partial x^2} & \frac{\partial^2\rho}{\partial x\partial y} & \frac{\partial^2\rho}{\partial x\partial z} \\ \frac{\partial^2\rho}{\partial y\partial x} & \frac{\partial^2\rho}{\partial y^2} & \frac{\partial^2\rho}{\partial y\partial z} \\ \frac{\partial^2\rho}{\partial z\partial x} & \frac{\partial^2\rho}{\partial z\partial y} & \frac{\partial^2\rho}{\partial z^2} \end{pmatrix} . = \begin{pmatrix} \lambda_1 & 0 & 0 \\ 0 & \lambda_2 & 0 \\ 0 & 0 & \lambda_3 \end{pmatrix} \tag{32}$$

CPs can be systematically classified using the (ω, σ) notation, ω corresponding to the number of non-zero eigenvalues of the Hessian matrix and σ being the sum of their signs. Within this scheme, four types of CPs are identified. A Nuclear Attractor Critical Point (NACP), denoted as $(3, -3)$, occurs when all three eigenvalues are negative, corresponding to a local maximum of the electron density and typically located at atomic nuclei. Ring Critical Points (RCPs), with signature $(3, +1)$, occur when two eigenvalues are positive and one is negative, and are associated with ring structures in molecules. Finally, Cage Critical Points (CCPs), denoted as $(3, +3)$, correspond to a local minimum of the electron density, with all three eigenvalues positive. Bond Critical Points (BCPs), classified as $(3, -1)$, which are referenced and

discussed in detail in the work presented in this thesis, are characterised by two negative curvatures and one positive curvature. Together, define a saddle point of the electron density. A BCP lies along the bond path between two nuclei and represents the minimum value of the electron density along this path. The properties derived from BCPs, such as the electron density value $\rho(r)$ and the Laplacian $\nabla^2\rho(r)$, provide essential insight into the strength and nature of chemical bonding, making them invaluable for analysing covalent and NCIs alike, the latter being a central theme of this thesis.

With that being said, in QTAIM, the electron density at the BCP, ρ_{BCP}, is directly related to the strength of the interaction, while the Laplacian, $\nabla^2\rho_{\mathrm{BCP}}$, obtained as the sum of the three eigenvalues, provides further classification. Typically, $\nabla^2\rho_{\mathrm{BCP}} < 0$ is associated with shared-shell interactions such as polar covalent bonds, whereas $\nabla^2\rho_{\mathrm{BCP}} > 0$ is characteristic of closed-shell interactions, including ionic bonds, hydrogen bonds, and weak NCIs. Additional insight is gained from the electronic energy density at the BCP, $K(\rho_{\mathrm{BCP}})$, defined as the sum of the local kinetic and potential contributions, $G(\rho_{\mathrm{BCP}})$ and $V(\rho_{\mathrm{BCP}})$, respectively:

$$K(\rho_{\mathrm{BCP}}) = G(\rho_{\mathrm{BCP}}) + V(\rho_{\mathrm{BCP}}) \tag{33}$$

To summarise, the nature of various interactions can be described as follows: covalent bonds are characterised by $V(\rho_{\mathrm{BCP}}) \ll 0$, $G(\rho_{\mathrm{BCP}}) \ll |V(\rho_{\mathrm{BCP}})|$, $K(\rho_{\mathrm{BCP}}) \ll 0$, and $\nabla^2\rho_{\mathrm{BCP}} < 0$, while NCIs are characterised by $V(\rho_{\mathrm{BCP}}) < 0$, $G(\rho_{\mathrm{BCP}}) \approx |V(\rho_{\mathrm{BCP}})|$, $K(\rho_{\mathrm{BCP}}) \approx 0$, and $\nabla^2\rho_{\mathrm{BCP}} \approx 0$.

2.3.2 Natural Bonding Orbitals

A Natural Bond Orbital (NBO)[242–244] represents a set of orthonormal, localised orbitals with maximal electron occupancy, designed to describe an N-electron molecular system that closely resembles a Lewis structure. These orbitals offer a localised depiction of the wavefunction, often referred to as the Natural Lewis Structure (NLS)

representation. Mathematically, each NBO is constructed from optimised linear combinations of Natural Atomic Orbitals (NAOs), resulting in what are known as Natural Hybrid Orbitals (NHOs):

$$h_A \sum_k a_k \Theta_k^{(A)} \tag{34}$$

Under these conditions, orbitals are classified as 1-centre, $n_A = h_A$, or 2-centre, $\Omega_{AB} = a_A h_A + a_B h_B$, with core (CR) and LP orbitals in the first group, and σ and π bonding orbitals (BD) in the second. To ensure orthogonality, each bonding NBO has an anti-bonding counterpart, $\Omega^*_{AB} = a_B h_A - a_A h_B$. Analysis of these orbitals yields the second-order perturbation energies $E(2)$, which quantify stabilisation from charge transfer between donor NBO i and acceptor NBO j, where q_i is the occupancy of the donor NBO, $F(i,j)$ are the off-diagonal NBO Fock matrix elements, and ϵ_i and ϵ_j are the diagonal elements of the NBO Fock matrix, representing the orbital energies:

$$E^{(2)} = \Delta E^{(2)}_{ij} = q_i \frac{F(i,j)^2}{\epsilon_i - \epsilon_j} \tag{35}$$

By evaluating the $E(2)$ corresponding to a given interaction, one can quantify its strength and simultaneously investigate its orbital characteristics for classification. For instance, XB interactions are characterised by the $E(2)$ associated with the CT from a LP orbital on the XB-acceptor to an antibonding σ^* orbital on the XB-donor atom X:

$$\mathrm{LP(XB_{acceptor})} \longrightarrow \sigma^*_{\mathrm{X}}\,(\mathrm{XB_{donor}}) \tag{36}$$

3 Monovalent XB-Based Scaffolds

3.1 Introduction

The application scope of XB-based scaffolds in organocatalysis has certainly been noteworthy since their initial reporting two decades ago.[121] Both neutral and cationic XB-based organocatalytic systems have been successfully applied across a variety of classic organic transformations.[89] Despite sustained effort, the precise nature of the XB interaction remains elusive, constraining progress in XB catalysis, particularly for asymmetric applications. This chapter establishes a theoretical framework to address this gap by systematically evaluating diverse XB-based scaffolds, focusing on key determinants of catalytic performance, including σ-hole depth, XB-donor identity, substrate binding mode, and scaffold electronic and steric effects.

Previously experimentally explored XB-based scaffolds by Gliese *et al.*[125] were evaluated within the C–C bond-forming step of the Michael addition of indole to *trans*-crotonophenone (Figure 3.1). In the context of α,β-unsaturated carbonyl substrate activation, binding modes are treated as mechanistic descriptors allowing a systematic comparison of activation pathways. Specifically, the well-established O-activation pathway was compared to the relatively underexplored π-type activation mode.[157] This analysis included the structurally minimal yet robust I_2 catalyst,[154] whose mechanistic nature continues to spark ongoing discussion.

The study was extended to the ROP of *L*-lactide (Figure 3.2), an industrially and biomedically important transformation for the synthesis of biodegradable poly(lactic

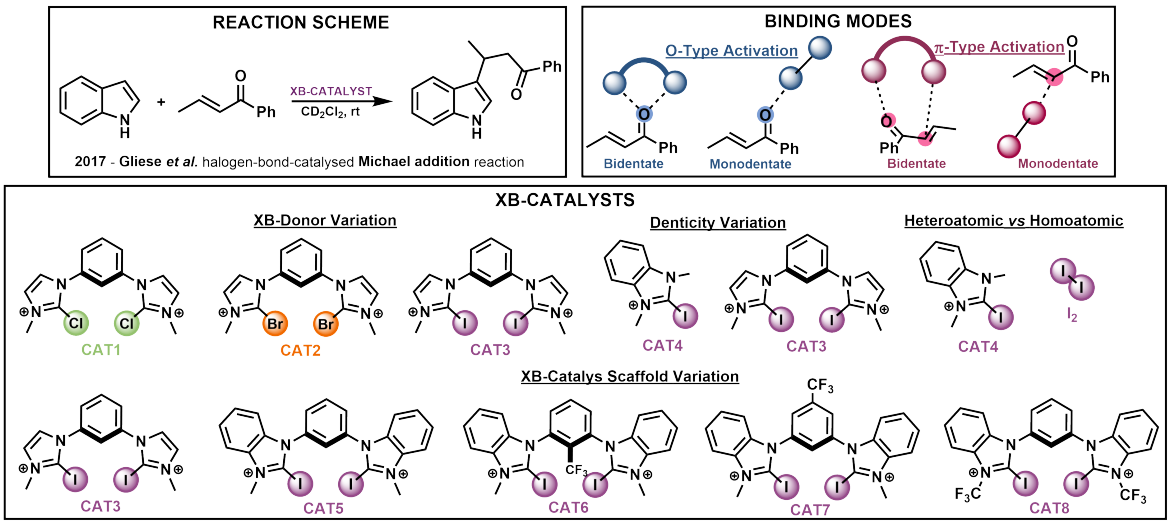

Figure 3.1: XB-based catalyst scaffolds and O- and π-type substrate binding modes for the C–C bond-forming step of the Michael addition of indole to *trans*-crotonophenone.

acid) (PLA).[189] XB-based catalysts have previously been applied to this process, notably using ICl_3.[123,245] In this context, XB-mediated binding modes serve as a key descriptor framework for mechanistic pathways, with variations in catalyst-substrate binding geometries correlating with divergent initiation profiles. These effects are examined in the presence of external bases (Figure 3.2), critical for polymerisation initiation and modulation.

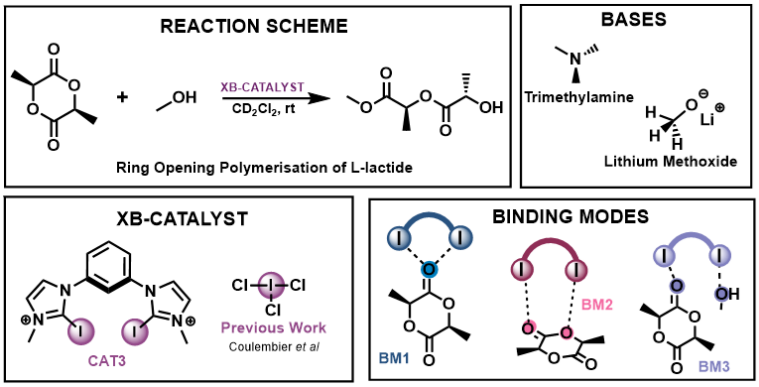

Figure 3.2: ROP of *L*-Lactide catalysed by CAT3 in the presence of different bases, with binding modes BM1-3 considered.

3.2 Computational Details

The structures and systems under evaluation were optimised at the ωb97xd /def2-svp[246,247] computational level at room temperature. Harmonic vibrational frequencies were computed at the same level used for the geometry optimisations to confirm the nature of the stationary points as local minima. Single-point calculations were performed to improve the energy description at the computational level of ωB97x-D/def2-tzvp[195,246,248] computational level for the systems under study, namely, monomers, catalysts, and catalyst-substrate complexes. Structure optimisations and energy calculations were performed using the Gaussian09 software.[249] The effective core potential def2-SVP basis set[195] has been used for the iodine atoms, where the tightly bound core electrons are replaced by an effective core potential, treating them as an effective potential, while more relevant valence electrons are treated explicitly.

Solvent effects were included in the optimisation by means of a continuum method, the Solvation Model based on Density (SMD) approach[250] in Gaussian09, using dichloromethane (DCM) as the solvent. The use of an implicit solvent model allows us to consider the electrostatic and non-electrostatic cavitation, solvation, and structural effects of the solvent while, at the same time, allowing for an undisturbed and in-depth analysis of any inter- and intramolecular interactions governing structural stabilisation of the catalyst-substrate complexes.

Relative energies (ΔE) were calculated as the difference between the energy of the optimised complex (E_{complex}) and the energy of each monomer (E_{monomer}) in its optimised geometry as shown in Eq 1.

$$\Delta E = E_{\text{complex}} - \sum E_{\text{monomer}} \tag{1}$$

The reported free energies ($\Delta G_{\text{def2tzvp}}$) in this thesis were computed by adding the

thermal correction (TC_{def2svp}) from the small basis set calculations to the electronic energy obtained from the higher level single point calculations (E_{def2tzvp}), as shown in Eq 1.

$$G_{\text{def2tzvp}} = E_{\text{def2tzvp}} + TC_{\text{def2svp}} \tag{2}$$

Relative energies (ΔG) were calculated as the difference between the energy of the optimised complex (G_{complex}) and the energy of each monomer (G_{monomer}) in its optimised geometry as shown in Eq 2.

$$\Delta G = G_{\text{complex}} - \sum G_{\text{monomer}} \tag{3}$$

The Molecular Electrostatic Potential (MEP) of the isolated monomers was calculated on the electron density isosurface of 0.001 a.u. This isosurface was shown to resemble the van der Waals surface.[239] These calculations were carried out using Gaussian09 software, and the numerical results were analysed using the Multiwfn program[251] and plotted using Jmol.[252]

The NBO[253] methodology version 7 was used to evaluate the strength of individual interactions by measuring the charge transfer between occupied and unoccupied orbitals within different fragments. The calculations were performed at the same level of theory as the geometry optimisations: ωb97xd /def2-svp. The NBO calculations yield the E(2) value, which will be thoroughly discussed in this thesis. As explained in the Computational Methods chapter, E(2) is defined as second-order perturbative energy, determined by the analysis of all possible interactions between Lewis-type NBO donors and non-Lewis-type NBO acceptors, with their energetic importance estimated through second-order perturbation theory. *"For each donor NBO (i) and acceptor NBO (j), the donor–acceptor stabilisation energy $E(2)$ associated with $i \rightarrow j$ delocalisation is calculated as $E(2) = \Delta E_{ij}(2) = \dfrac{q_i F(i,j)^2}{\varepsilon_j - \varepsilon_i}$, where q_i represents the donor orbital occupancy (2 for closed shell, 1 for open shell), ε_i and ε_j denote the diag-*

onal elements (orbital energies), and $F(i,j)$ stands for the off-diagonal NBO Fock matrix element." [253]

The QTAIM methodology [254,255] was used to analyse the electron density of the systems within the AIMAll software, and the electron density at the bond critical points (BCPs) was extracted from the various systems upon complexation. The calculations were performed at the same level of theory as the geometry optimisations: ωb97xd /def2-svp.

3.3 Results & Discussion

3.3.1 Michael Addition of Indole to *trans*-Crotonophenone

3.3.1.1 Electronic Properties

The study began with MEP calculations to characterise the electronic features of the XB catalyst scaffolds, focusing on the effects of the XB-donor atom and its polarisability on the σ-hole size. The MEP analysis provides a direct measure of the charge distribution around the XB-donor atoms, allowing for a comparison of the respective σ-hole size and intensity, which are key descriptors of XB-donor strength and substrate-stabilising ability.

Using the optimised geometries of each catalyst, we compared the relative V_{max} values (the MEP *maxima* expressed in kcal/mol associated with the σ-hole) for a representative set of bidentate XB-donor catalysts (CAT1–3), each representing a different XB-donor atom. The results, summarised in Figure 3.3, show a clear expected increase in V_{max} (kcal/mol) with the polarisability of the XB-donor atom. CAT3 contains the most polarisable XB-donor atom iodine and exhibits the highest V_{max} (kcal/mol), corresponding to the most pronounced σ-hole and the strongest potential for XB interactions. This observed trend is consistent with previous theoretical insights, confirming that XB-donor atom polarisability governs the strength of XB interactions in organocatalysis. The relatively intense σ-hole on CAT3 reflects its

capacity for stronger substrate activation through NCIs.

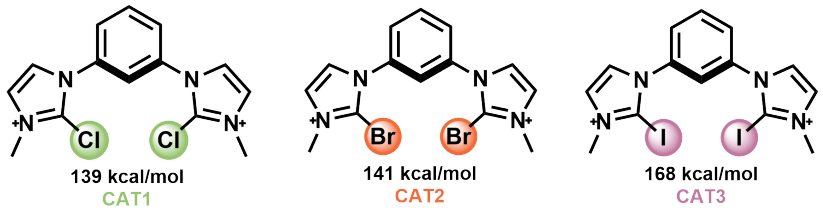

Figure 3.3: MEP on the 0.001 a.u. electron density isosurface and the *maxima* (V_{max}) values of the MEP in kcal/mol for the catalysts under study (CAT1–3).

Following the investigation into the influence of the XB-donor atom on the electrostatic potential of XB-based catalytic scaffolds, attention was subsequently directed toward exploring how variations in electronic and structural features of the catalytic framework affect the size and intensity of the σ-hole. To ensure consistency across comparisons and to isolate the effects of structural modulation, iodine was selected as the fixed XB-donor atom for this study. Iodine's high polarisability and its established efficiency in forming strong XBs make it an ideal benchmark XB-donor for assessing scaffold-induced electronic variations.

The influence of various critical structural parameters was evaluated, including denticity of the scaffold, spatial placement of substituents, and the electron-withdrawing capacity of the catalyst framework. These factors were systematically investigated on a varied set of XB-based catalysts, as shown in Figure 3.4. Catalysts CAT3–CAT6 correspond to systems previously reported in the literature, whereas CAT7 and CAT8 were designed and explored here solely through theoretical modelling. In addition, molecular iodine (I_2) was included for comparison, as it represents the first iodine-based catalyst described in XB catalysis. MEP calculations were used to quantify the changes in σ-hole size, using the V_{max} (kcal/mol) associated with the σ-hole, as a descriptor of XB strength.

A clear trend emerges in σ-hole intensity when comparing homoatomic I_2 against the heteroatomic scaffolds (CAT3–CAT8): the latter all exhibit substantially higher V_{max} values due to electron-withdrawing groups that polarise the iodine centers (Figure 3.4).

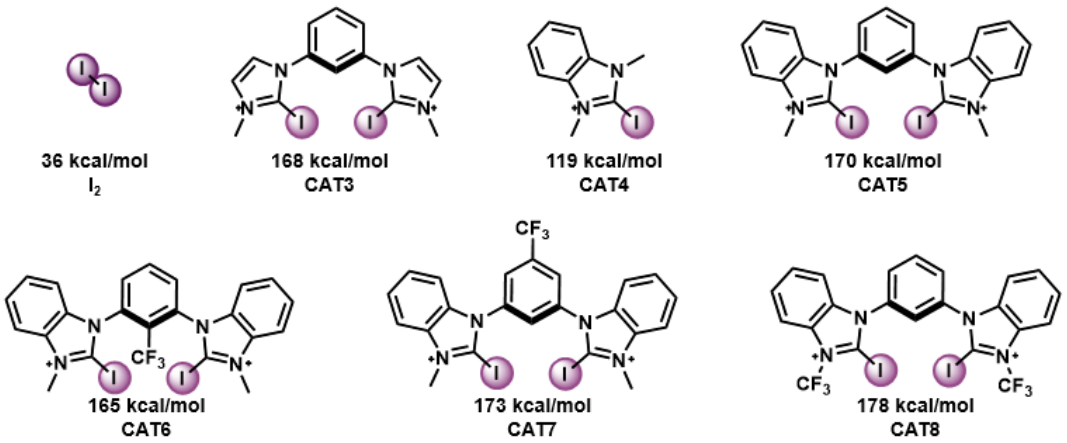

Figure 3.4: MEP on the 0.001 a.u. electron density isosurface and the *maxima* (V_{max}) values of the MEP in kcal/mol for the catalysts under study (CAT3–8 and I_2).

The effects of electronic modulation were further investigated for bidentate CAT3, CAT5, and CAT6 by systematically varying scaffold electron-withdrawing capacity (Figure 3.4). Replacing the imidazolium moiety in CAT3 with the more electron-deficient benzimidazolium unit in CAT5 resulted in a modest increase in σ-hole magnitude (168 to 170 kcal mol^{-1}). This reflects the fundamental role of scaffold electron withdrawal in enhancing XB-donor electrophilicity.

However, an intriguing deviation from this trend was observed in CAT6, where the introduction of a trifluoromethyl (–CF_3) substituent in the ortho position relative to the benzimidazolium ring led to a reduction in σ-hole size to 165 kcal/mol. This reduction suggests that local steric or inductive effects imposed by the (–CF_3) substituent may counteract the broader electron-withdrawing effects of the scaffold, potentially diminishing the ability of the XB-donor atom to maintain an intense σ-hole (Figure 3.5).

Motivated by this deviation, the positional influence of the (–CF_3) substituent on σ-hole size was further investigated through the computational proposition of CAT7 and CAT8 (Figure 3.4), where the placement of the CF_3 group was varied within the benzimidazolium-containing framework. MEP analysis revealed the modulating effects of CF_3 group placement on σ-hole magnitude, highlighting the combined importance of modulating effects of CF_3 group placement on σ-hole magnitude, high-

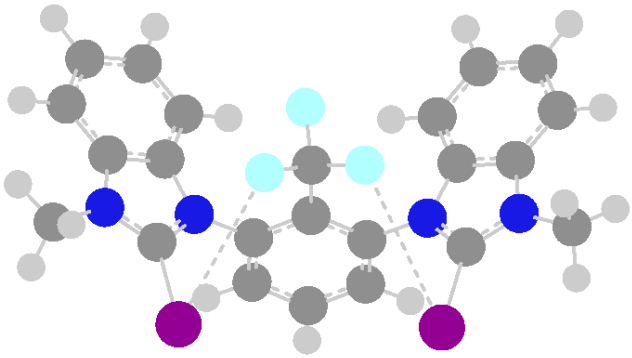

Figure 3.5: NCIs between the XB-donor atom and CF_3 substituent found in CAT6.

lighting the combined importance of electron-withdrawing capacity and substituent positioning scaffold on σ-hole size.

3.3.1.2 Reactivity Studies

The transition state energy for the C–C coupling step (TS1) in the Michael addition of indole to *trans*-crotonophenone was computed and compared across the range of the previously mentioned XB-based catalysts (Figure 3.3 and 3.4). Building upon the electronic properties study through MEP analysis, as discussed in section 3.3.1.1 Electronic Properties, the study was extended to the catalytic implications of varying the electronic properties of XB-donor atoms and scaffolding on the transition state energies. In the initial stage of this mechanistic investigation, we focused on the O-activation mode, an interaction pathway widely-documented in the literature for HB-based organocatalysis[256] and experimentally supported by Gliese *et al.* for XB-based applications. As illustrated in Figure 3.1, the O-activation pathway involves the formation of a stabilising NCI between the XB-donor of the catalyst and the carbonyl oxygen atom of the *trans*-crotonophenone substrate, mimicking the classic HB-based substrate activation motif.

Consistent with the trends observed in the MEP analysis, the computed activation barriers for TS1 (Figure 3.6) reflect a clear dependence on the polarisability of the XB-donor atom. Across CAT1–3 (Cl/Br/I XB-donors), the transition state energy

decreases with increasing halogen polarisability. Iodine-based CAT3, showing the lowest energy barrier (Figure 3.6) due to its deepest σ-hole, thus confirming the advantageous role of highly polarisable XB-donors in stabilising the TS energy.

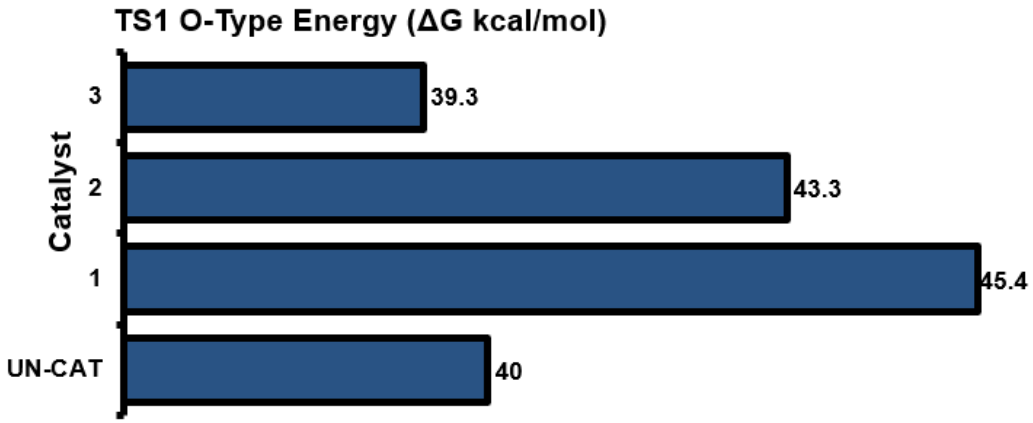

Figure 3.6: TS energy (ΔG kcal/mol) for the O-activated TS1 of the Michael addition of indole to *trans*-crotonophenone under the catalysis of CAT1-3.

Turning to iodine-based scaffolds (CAT4, CAT6-8, I_2), the energy barriers calculated for CAT4, CAT6, and I_2 were observed to be higher than the uncatalysed reaction (Figure 3.7), suggesting that the XB-interaction within the O-activated TS1 of the Michael addition is relatively weak and ineffective, contradictory to experimental findings reported in literature.[125] Similar to the relatively low σ-hole observed for CAT6 (Figure 3.4), the transition state energy (Figure 3.7) followed a similar trend.

Consequently, in light of the contradictory transition state energies calculated for the O-activation mode, as well as the high activation barrier (due to the entropy penalty too), an alternative mechanistic pathway was considered to further elucidate the nature of substrate activation in XB-based catalytic systems. Recent work by Robidas *et al.*[157] proposed a π-type activation mechanism for the stabilisation of α,β-unsaturated carbonyl compounds, where the double bond acts as a nucleophilic site, contrasting the traditional lone-pair O-activation.

The underexplored substrate binding model offers an additional perspective on substrate activation through a direct stabilisation interaction with the π-system of

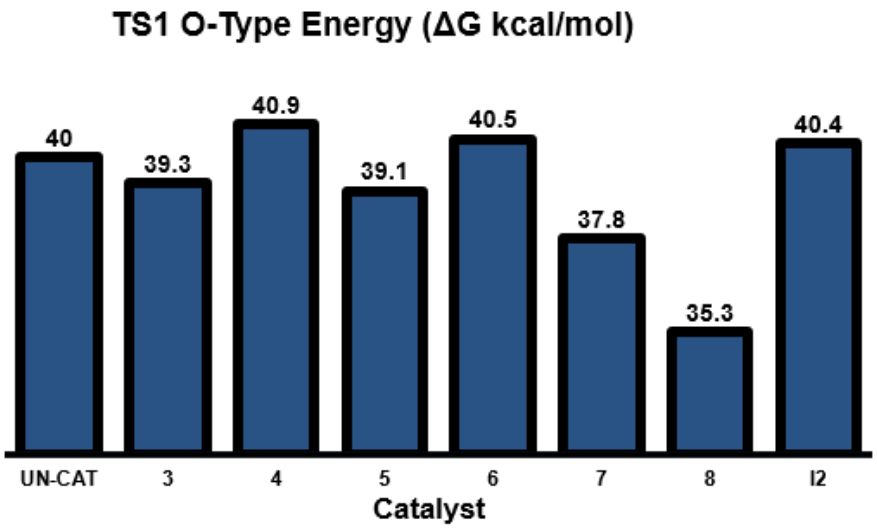

Figure 3.7: TS energy (ΔG kcal/mol) for the O-activated TS1 of the Michael addition of indole to *trans*-crotonophenone under the catalysis of CAT3–8 and I_2.

the unsaturated substrate moiety. The alternative binding motif was evaluated in the context of iodine-based XB-catalysts, namely I_2, CAT3, CAT4, CAT6 and CAT8.

Bidentate CAT3, CAT6, and CAT8 enable dual-site activation where one iodine atom binds the carbonyl oxygen lone pair, while the second binds at the π-bond α-carbon, resulting in a hybrid binding mode. Monodentate CAT4 and I_2 bind solely at the α-carbon (Figure 3.8).

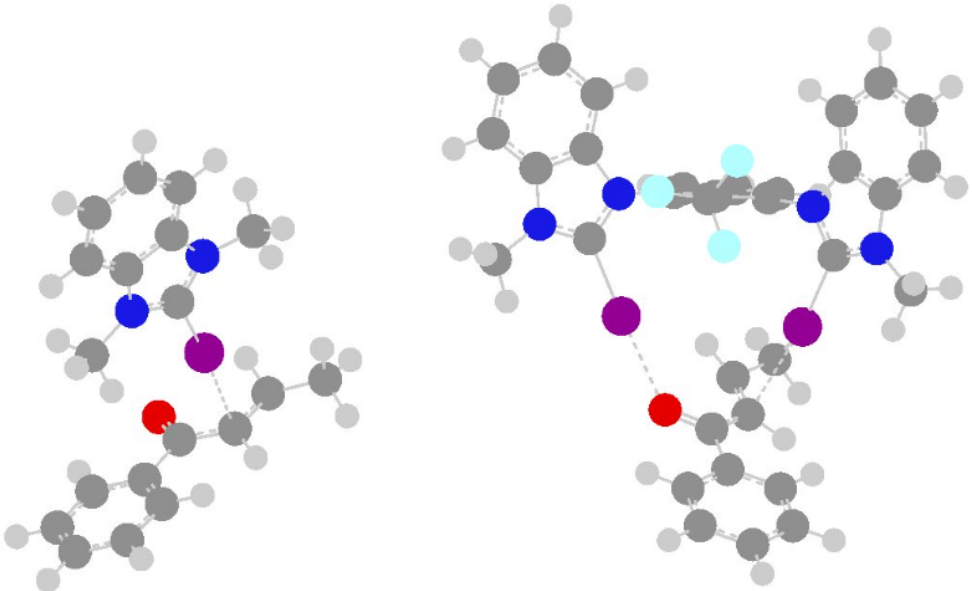

Figure 3.8: π-type substrate activation shown in monodentate systems (left) and bidentate systems (right)

.

Notably, majority of catalysts examined, I_2, CAT3, CAT6, and CAT8, energetically favour π-type activation over O-activation (Figure 3.9). CAT4, being the exception, displayed a lower and thereby a more energetically favourable activation barrier for the O-activation mode.

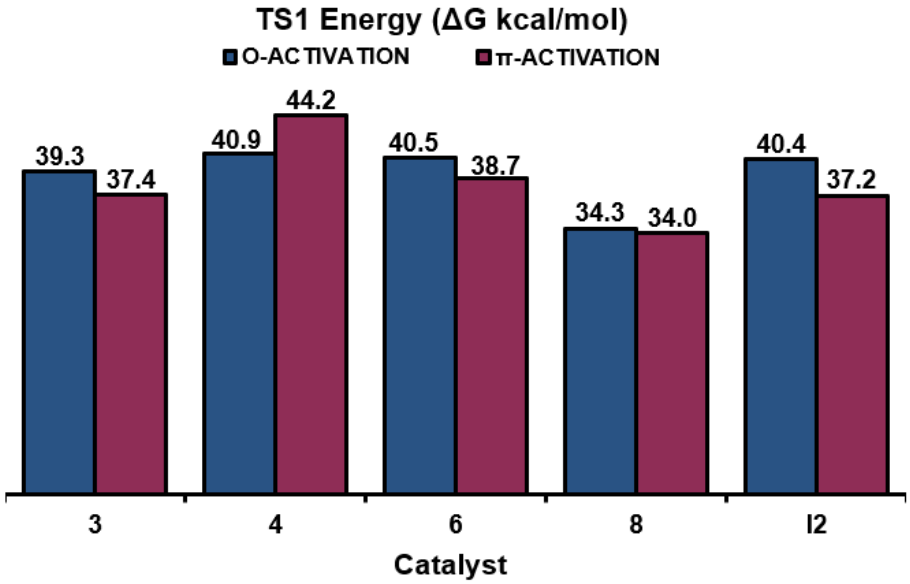

Figure 3.9: TS energy (ΔG kcal/mol) for the O- and π-type activated TS1 of the Michael addition of indole to *trans*-crotonophenone under the catalysis of XB-based catalysts.

Collectively, these trends support that the hybrid π-type substrate stabilisation mode is the energetically preferred pathway and the model which produces a TS1 energy trend most consistent with experimentally derived conversions (%). As shown in Figure 3.10, unlike O-type TS1 energy, the π-type TS1 energy trends align with the experimental conversion (%) trends reported by Gliese *et al.*[125]

Collectively, these trends support the hybrid π-type substrate stabilisation mode as the energetically preferred pathway. This model also produces a TS1 energy trend that is most consistent with the experimentally derived conversion (%) data. As shown in Figure 3.10, the π-type TS1 energy trends align with the experimental conversion (%) trends reported by Gliese *et al.*,[125] unlike the O-type TS1 energy trends.

Transition state energies reveal clear preferences. Most catalysts (I_2, CAT3, CAT6,

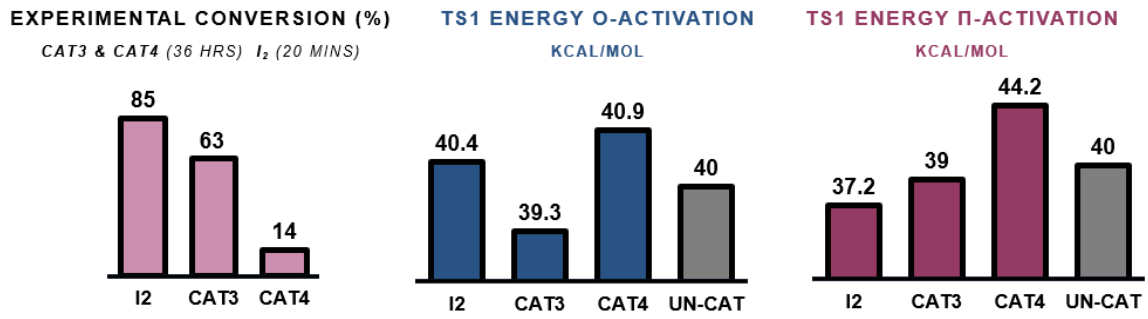

Figure 3.10: Trends shown for experimentally derived conversions (%), O-activation TS energy (kcal/mol) and π-type activation TS energy (kcal/mol) for TS1 of Michael Addition of Indole to *trans*-Crotonophenone via XB-based catalysts (left to right).

CAT8) favour π-activation over O-activation. Bidentate scaffolds (CAT3, CAT6, CAT8) specifically prefer the π-activation mode, while monodentate CAT4 favours classical O-activation.

For I_2, O-activation predicts inactivity due to high barriers, whereas π-activation reduces the barrier below the uncatalysed reaction, in line with its robust activity reported experimentally.[125,154] This deviating observation was subsequently rationalised in Section 3.3.1.4 I_2-Driven Mechanistic Pathways.

To further understand the structural implications of catalyst-substrate interactions in XB-based catalysis, a geometry-based study was undertaken, focusing on conformational distortions within the catalytic scaffold upon TS1 assembly. Specifically, the analysis focused on the energy required for the rotation of the dihedral angle α within the bidentate framework, a geometric parameter particularly sensitive to substrate engagement and activation (Figure 3.11). This analysis was used to quantify the framework distortion energy (FDE), defined as the energetic penalty associated with deforming the catalyst framework from its relaxed ground-state geometry into the conformation required for transition-state formation.[257]

The catalyst's geometry from the fully optimised TS1 structures of the Michael addition reaction was directly compared to the corresponding geometry of the catalyst in its isolated, unbound monomeric form. By isolating the catalyst geometry in its TS1 conformation and comparing it to the optimised free catalyst structure, the extent of

structural reorganisation required for catalysis could be assessed independently of direct catalyst-substrate interaction energies. The objective was to assess the extent of structural reorganisation required for catalysis and to quantify the energetic penalty associated with this conformational adjustment.

The metric ΔE, illustrated in Figure 3.11, was defined as the energy difference between the catalyst in its TS-bound conformation and its monomeric, ground-state geometry. Mathematically, this is expressed as $\Delta E = E_{TS(cat)} - E_{monomer(cat)}$ Where a positive ΔE indicates that the catalyst must adopt a higher-energy conformation upon substrate binding, reflecting an inherent energetic cost associated with catalytic activation.

The conformational strain, reflected in ΔE, varies significantly depending on the mode of substrate activation. Across the series of catalysts examined, ΔE values were consistently lower for π-type activation modes relative to their O-activation mode counterparts. This suggests that the transition from the unbound catalyst to the substrate-bound geometry is less energetically demanding in the π-activated systems. Indicating that π-type activation is associated with lower reaction activation barriers for TS1 (Figure 3.9) and reduced conformational distortion of the catalytic scaffold.

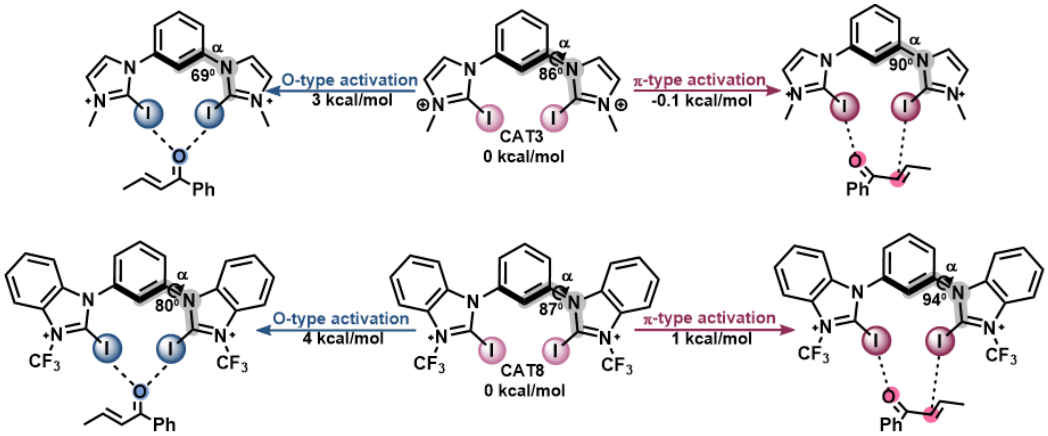

Figure 3.11: ΔE (kcal/mol) for the O- and π-Type Activated Bidentate Catalytic Systems Transitioning from the Monomeric to Substrate-Bound TS1 State.

These findings provide important structural insight into the mechanistic divergence

between the two activation pathways.O-activation demands significant catalyst deformation (ΔE penalty) despite strong localised XB at the carbonyl oxygen, while the π-type mode minimises structural rearrangement. Critically, this hybrid dual-site anchoring positions the substrate more tightly and optimally for nucleophilic attack, providing justification on its relatively lower TS1 barriers.

3.3.1.3 Characterisation of NCIs

To further elucidate the nature and strength of the XB-interactions underpinning the catalytic behavior discussed in section 3.3.1.2 Reactivity Studies, a detailed quantification of the NCIs between the XB-donor atom (X) and the carbonyl oxygen atom (O) of the *trans*-crotonophenone substrate was performed, using two complementary computational approaches. Figure 3.12 illustrates the interaction between the halogen atom (X) of the catalyst and the carbonyl oxygen (O) of the substrate in the O-activation mode, highlighting the key features of the XB interaction. The QTAIM analysis enabled the identification of BCPs, points of locally concentrated electron density that indicate an electronic interaction between two atoms, and their corresponding ρ values, which serve as direct indicators of the presence and strength of an XB interaction. In all cases examined, a BCP was observed between the XB-donor atom and the carbonyl oxygen, thereby confirming the existence of a stabilising halogen bond in the O-activation mode.

Complementary to QTAIM, NBO analysis provided further insights into the donor-acceptor interactions governing the XB interaction. Second-order perturbation theory revealed stabilising LP (O) $\rightarrow$ BD*(X-R) interactions, corresponding to the charge transfer (CT) process of the lone pair (LP) electron density from the oxygen atom LP (O) to the antibonding orbital of the halogen-containing moiety BD*(X-R), as expected in the O-activation mode. The magnitude of these interactions correlated with the polarisability of the XB-donor atom, with iodine-based systems exhibiting the highest stabilisation energies (Figure 3.12).

A similar characterisation was performed for the XB interaction in the O-activated

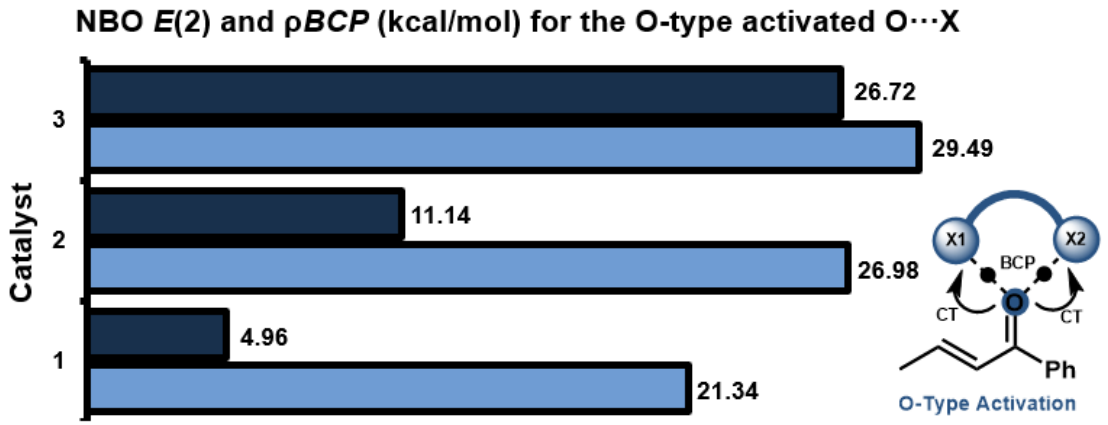

Figure 3.12: NBO $E(2)$ (dark blue) and ρ_{BCP} (light blue) in kcal/mol for the O···X Interaction within the O-Activated TS1 of the Michael Addition of Indole to *trans*-Crotonophenone under the Catalysis of CAT1-3.

TS1 of the substituted scaffold systems (Figure 3.13). Collectively, the QTAIM and NBO results were found to be consistent with MEP and TS1 transition state energies discussed in Sections 3.3.1.1 Electronic Properties and 3.3.1.2 Reactivity Studies, respectively.

Overall, the quantitative agreement between the two methods not only confirms the presence of a true XB in the activated TS1 catalyst-substrate complex but also affirms the central role of the XB-donor atom polarisability and scaffold substituents in shaping the strength and character of the XB-based interaction.

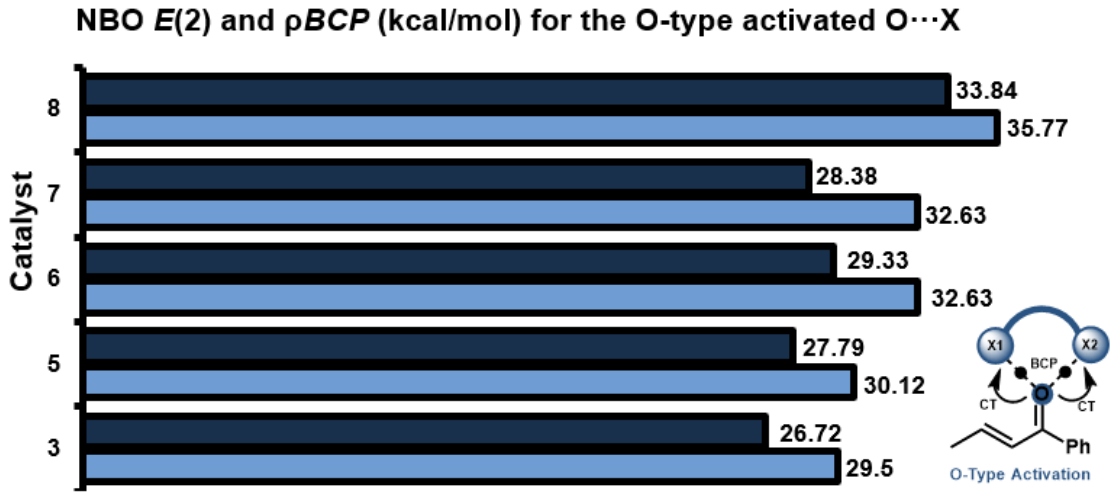

Figure 3.13: NBO $E(2)$ (dark blue) and ρ_{BCP} (light blue) in kcal/mol for the O···X Interaction within the O-Activated TS1 of the Michael Addition of Indole to *trans*-Crotonophenone under the Catalysis of CAT3-8.

CAT6 emerged as a notable outlier in the otherwise strong correlation between computed activation barriers and the descriptors of XB strength (Figure 3.4, Figure 3.7, and Figure 3.13). Although QTAIM analysis indicated a comparatively strong electron density at the BCP, ρ_{BCP}, and NBO analysis revealed a clear LP(O) $\rightarrow$ BD*(X–R) donor–acceptor interaction with a measurable second-order perturbation energy $E(2)$, these indicators did not fully align with the unexpectedly high O-type activation barrier predicted for in the CAT6-catalysed TS1 (40.5 kcal/mol). Regardless, the general trend in XB interaction strength derived from both QTAIM and NBO analyses remained consistent with available experimental observations.[125] Specifically, the relative order of catalytic activity was preserved across the series CAT3 < CAT5 < CAT6.

The substrate stabilising interaction in the O-activation and π-type modes was quantified and compared. The bidentate CAT3 and CAT8 revealed enhanced substrate stabilisation interactions in the π-type activation mode (Figures 3.14 and 3.15), as evidenced by the $E(2)$ and ρ_{BCP} between the O and the X atoms. The monodentate I_2 followed the same trend, as shown by the relatively higher $E(2)$ and ρ_{BCP} between the O and the X atoms in the π-type activated system. The opposite was observed for monodentate CAT4, which had relatively higher $E(2)$ and ρ_{BCP} between the O and the X atoms in the O-activated mode (Figures 3.14 and 3.15).

The bidentate XB-based organocatalysts exhibit a clear preference for the π-type activation mode due to their ability to simultaneously activate both active sites of the *trans*-crotonophenone substrate, the carbonyl oxygen and the α-carbon. Monodentate I_2 and CAT4 interact with the substrate solely through carbonyl oxygen (O-activation) or the α-carbon (π-type activation). In CAT4, the substrate stabilisation is stronger in the O-activation mode (Figure 3.14 and Figure 3.15). Conversely, I_2 exhibits stronger substrate stabilisation in the π-type activation mode (Figure 3.14 and Figure 3.15).

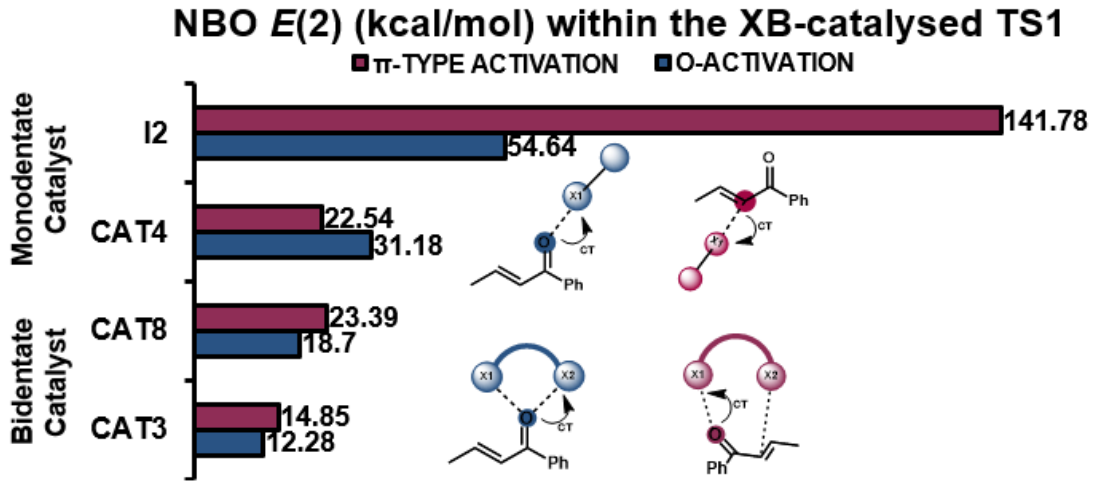

Figure 3.14: NBO $E(2)$ (kcal/mol) for the O···X Interaction within the bidentate catalytic systems (A) and the O/C···X interactions within bidentate catalytic systems (B) in the O- (blue) and π-type (red) activated TS1 of the Michael addition of indole to *trans*-crotonophenone.

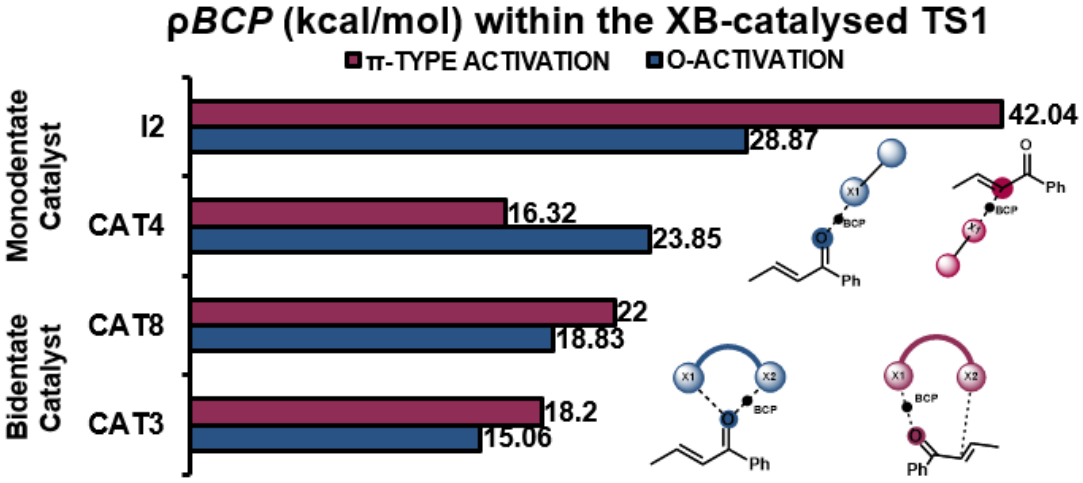

Figure 3.15: ρ_{BCP} (kcal/mol) for the O···X Interaction within the bidentate catalytic systems (A) and the O/C···X interactions within bidentate catalytic systems (B) in the O- (blue) and π-type (red) activated TS1 of the Michael addition of indole to *trans*-crotonophenone.

3.3.1.4 I_2-Driven Mechanistic Pathways

The catalytic utility of molecular iodine in a wide range of organic transformations is well documented.[258,259] Despite its structural simplicity and lack of elaborate functionalisation, I_2 has been repeatedly shown to operate as a highly effective catalyst. However, the precise mechanism through which I_2 facilitates such transformations has remained a subject of ongoing debate, with several competing explanations

proposed in the literature over recent decades.[260]

Motivated by the unexpectedly strong NCIs observed between I_2 and the α-carbon of *trans*-crotonophenone in the π-activation mode, significantly exceeding those observed for the monodentate heteroatomic CAT4 (Figures 3.14 and 3.15), a comprehensive mechanistic investigation was undertaken. Despite CAT4 exhibiting a relatively deeper σ-hole in the MEP analysis (Figure 3.4), enhanced substrate-stabilisation occurred through the I_2 π-activation mode. Complete reaction pathways for both O- and π-activation modes in the I_2-catalysed Michael addition of indole to *trans*-crotonophenone were fully optimised and energetically evaluated.

As shown in Figure 3.16, relative to O-activation the π-type activated mechanism demonstrated significantly lower energy barriers for both the C–C bond-forming TS (TS1) and the subsequent proton transfer step (TS2). The activation barrier calculated for TS1 in the O-activation mode was calculated at 40.4 kcal/mol, whereas the π-type pathway exhibited a barrier of 37.2 kcal/mol, resulting in a $\Delta\Delta G$ of 3.2 kcal/mol in favour of the π-activation route. A more pronounced difference was observed for TS2, where the O-activated barrier was calculated to be 34.1 kcal/mol and π-type activation 23.7 kcal/mol, resulting in a $\Delta\Delta G$ of 10.4 kcal/mol.

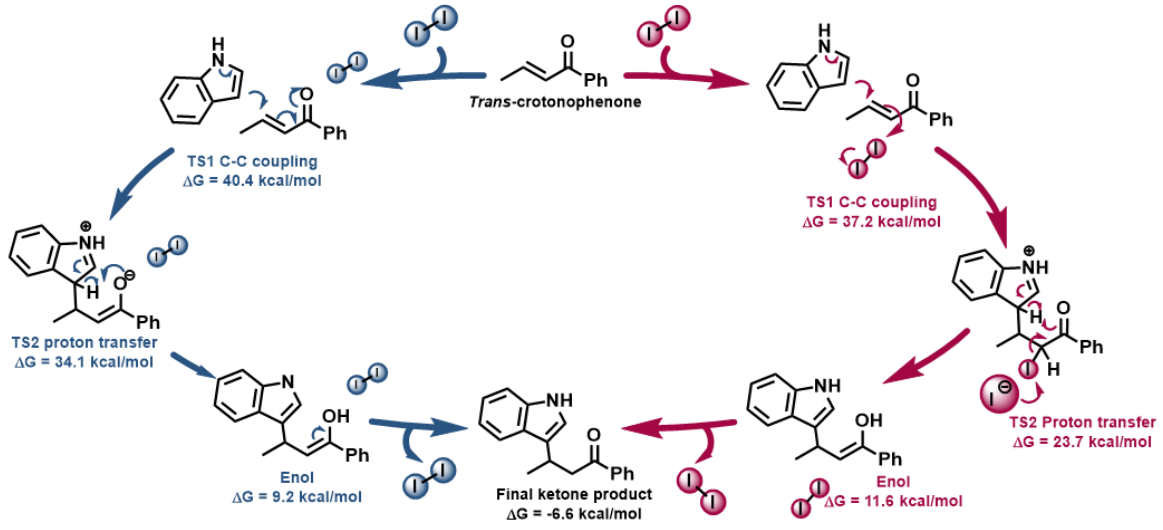

Figure 3.16: Mechanism of the O- (blue) and π-type (red) activated Michael addition reaction of indole to *trans*-crotonophenone under the catalysis of I_2, including the corresponding ΔG (kcal/mol).

Following an in-depth analysis of critical structural parameters, including bond lengths, hybridisation angles, and NCI descriptors, using the QTAIM methodology was carried out (Figure 3.17). Particular focus was brought to electron density at the BCP ρ_{BCP}, the Laplacian of the electron density $\nabla^2\rho(r)$, and the total energy density (H) to determine the precise nature of the interaction throughout the catalytic cycle. Comparative analysis was conducted using geometrically optimised control compounds to establish a baseline, as shown in Figure 3.17.

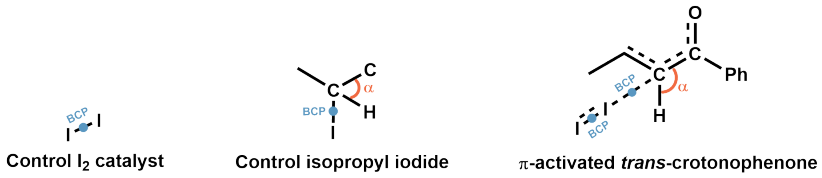

Figure 3.17: Electronic features and bond length measured at the ρ_{BCP} (red) as well as the angle of hybridisation α (blue) of the π-type activated *trans*-crotonophenone under the catalysis of I_2.

Significant changes in bond length, ρ_{BCP}, and H values were observed for I_2 in the Int1 step (Table 3.1), suggesting a shift in I_2 bond nature from covalent to noncovalent. The transitional nature in the bond nature of the I_2, when bound to the π-type activated substrate, can be described as a hybrid interaction profile, in which I_2 exhibits both electrophilic and XB-donor behaviour.

I-I	TS1	Int1	TS2	Int2	Control
Bond length (Å)	3.032	3.69	3.51	2.74	2.69
ρ_{BCP} (a.u.)	0.038	0.011	0.016	0.066	0.072
$\nabla^2\rho_{BCP}$ (a.u.)	0.048	0.027	0.035	0.014	0.0033
H value	-0.0066	0.00080	-0.00029	-0.016	-

Table 3.1: Structural and electronic features of the I_2 catalyst bound to the π-type activated *trans*-crotonophenone substrate in the full mechanistic pathway of the Michael addition reaction, compared to the control isolated I_2 catalyst.

Subsequently, a complementary investigation was conducted on the interaction between I_2 and the α-carbon of π-type activated substrate, using the C–I bond in a geometrically optimised isopropyl iodide as the control (Figure 3.17). The most pronounced change in bonding nature was again observed in Int1 (Table 3.2), where the C-I interaction displayed features which resemble weakly covalent bonding, a

shortened bond length, a negative $\nabla^2\rho(r)$, a negative H value, and a hybridisation angle of a sp^3-hybridised centre at the α-carbon.

C-I	TS1	Int1	TS2	Int2	Control
Bond length (Å)	2.42	2.20	2.22	3.022	2.20
ρ_{BCP} (a.u.)	0.07	0.11	0.10	0.02	0.11
$\nabla^2\rho_{BCP}$ (a.u.)	0.044	-0.026	-0.0088	0.045	-0.063
H value	-0.014	-0.0460	-0.037	-0.0002	-
α (°)	115.16	110.68	112.27	118.48	110.54

Table 3.2: Structural and QTAIM analysis of the I_2 catalyst bound to the π-type activated *trans*-crotonophenone substrate in the full mechanistic pathway of the Michael addition reaction, compared to the control isopropyl iodide molecule.

The ability of I_2 to form covalent bonds with unsaturated hydrocarbons is well-established in literature, specifically in the context of electrophilic iodination in polar solvents.[261,262] In the iodofluorination of α,β-unsaturated esters, formation of an iodonium ion through covalent bonding at the α-position has been widely reported,[263] supporting the weakly covalent bonding behavior observed in the π-type activated TS1 of the I_2-catalysed Michael addition reaction. Moreover, iodine's uniquely low reduction potential among the halogen series facilitates the conversion from I_2 to I^-, effectively lowering the thermodynamic barrier for redox and bonding transitions.[264] The observed transformation of I_2, from neutral molecular iodine to an I^-, therefore aligns with its expected redox behaviour in unsaturated systems such as the α,β-unsaturated carbonyl-containing substrate in this study.

The mechanistic and electronic characterisation presented here provides evidence that π-type activated I_2-catalysed Michael addition proceeds through a transitional bonding nature, where the I_2-substrate interaction changes from a weakly covalent to NCI along the reaction coordinate, enabling lower activation barriers. These findings not only deepen the understanding of the π-type activated mechanism but also offer a potential explanation for the robust catalytic activity of I_2 in organic transformations.

3.3.2 Ring-opening polymerisation of *L*-lactide

3.3.2.1 Reactivity Studies

Having established the mechanistic preference of the π-type activation mode in the XB-catalysed Michael addition, a series of catalyst-substrate binding modes were applied to the ring-opening polymerisation (ROP) of *L*-lactide. Three distinct binding modes for CAT3 with *L*-lactide were evaluated (Figure 3.18), to assess their influence on *L*-lactide activation and ROP control.

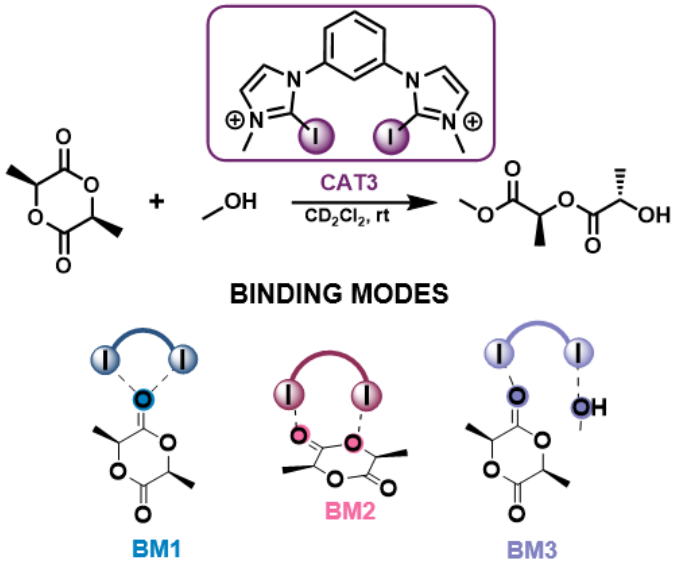

Figure 3.18: Binding mode assemblies BM1-3 of the XB-activated ROP of *L*-lactide.

Binding Mode 1 (BM1) represents the classical and widely studied O-activation mode pathway. In this configuration, the *L*-lactide monomer is activated through a bidentate XB-based interaction through a single anchor point at the carbonyl oxygen atom. Binding Mode 2 (BM2) employs a bidentate XB-based interaction, diverging from BM1 in its dual-anchor point interaction with the carbonyl and ester oxygen atoms of the *L*-lactide monomer. Binding Mode 3 (BM3) involves a bidentate XB-based dual-anchor point interaction with the carbonyl oxygen of the *L*-lactide monomer and the hydroxyl group of the methanol initiator. This configuration mimics cooperative activation, where both the monomer and initiator are pre-organised through XB interactions.

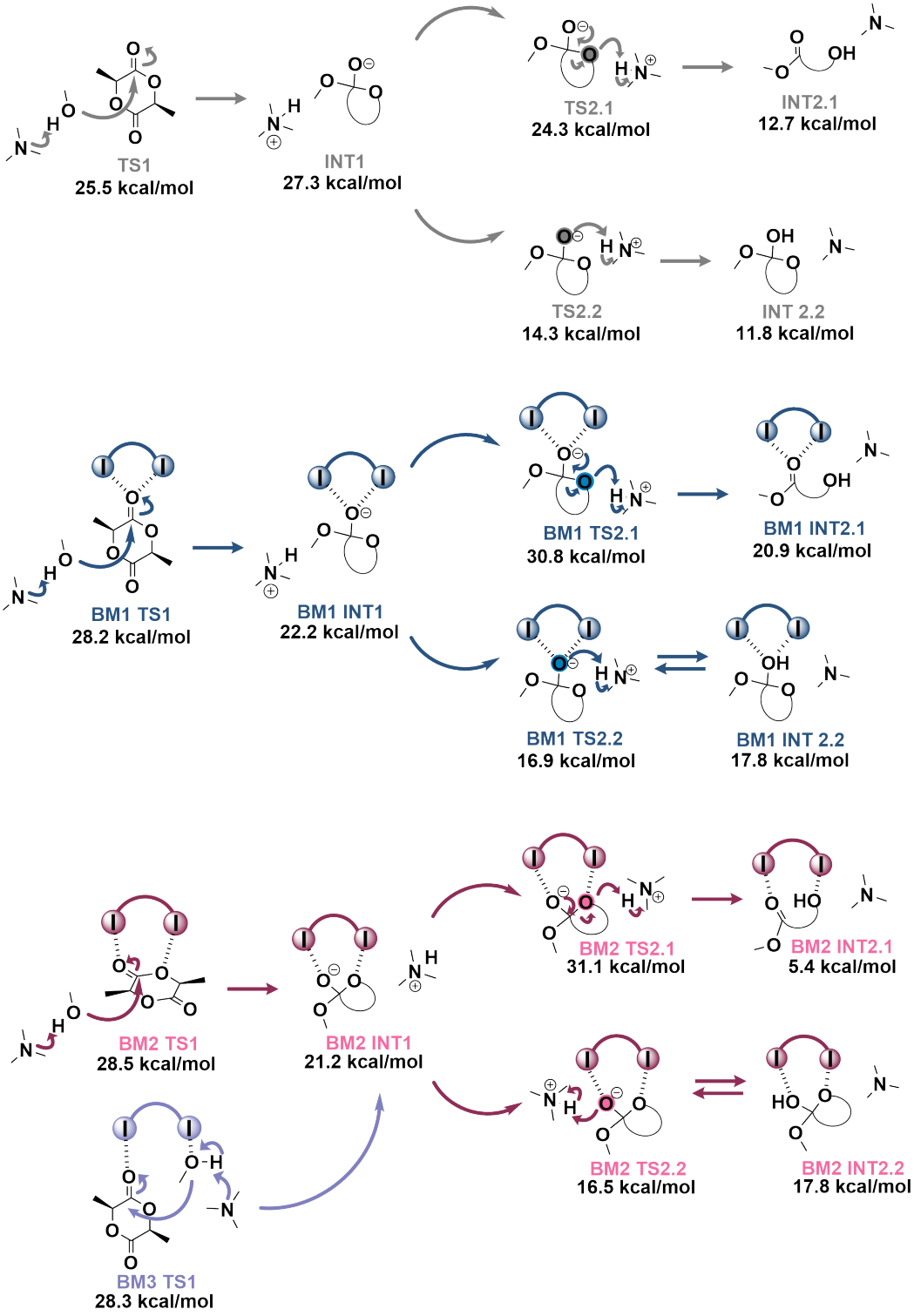

Figure 3.19: PES (ΔG kcal/mol) of the ROP of *L*-lactide initiated by trimethylamine base in the absence (grey) and presence of CAT3 through various catalyst-substrate binding mode assemblies, BM1 (blue), BM2 (pink) and BM3 (purple).

Together, these three binding modes represent distinct mechanistic models through which XB-based CAT3 stabilises the ROP of *L*-lactide. By examining their relative

energetic effect on the ROP of *L*-lactide, the relationship between binding mode architecture and catalytic performance is revealed. The study included the co-catalytic role of Brønsted and Lewis basic additives, which are commonly employed in experimental ROP protocols to promote monomer activation and facilitate the nucleophilic ring-opening step. Two bases were selected for this purpose, trimethylamine a neutral Brønsted base known for its capacity to abstract protons and modulate electrophilicity through HB and lithium methoxide, a stronger, ionically dissociated Lewis base that offers both nucleophilic and anionic coordination capabilities.

The free potential energy surface for the three binding modes, as well as for the uncatalysed, was calculated, Figure 3.19. The ROP of *L*-lactide in the absence of XB-based CAT3 proceeds in an uncontrolled fashion, limiting control over product formation. The conjugate acid of trimethylamine thermodynamically favours protonation of the alkoxide intermediate through TS2.2, 14.3 kcal/mol, rather than the ester oxygen through TS2.1, 24.3 kcal/mol, resulting in INT2.2, 11.8 kcal/mol being more stable and thereby preferred to the intended open chain product INT2.1, 12.7 kcal/mol.

In the presence of CAT3, while the overall thermodynamic profile of the ROP reaction does not significantly shift, marked by the marginal decrease in the absolute transition state energies, the role of CAT3 becomes evident in modulating the reaction pathway and enhancing product selectivity. This is evidenced by the relatively energetically stable open chain product BM2 INT2.1, 5.4 kcal/mol, in comparison to BM2 INT2.2, 17.8 kcal/mol, rendering the competing pathway BM2 TS2.2 more reversible, giving kinetic access to BM2 TS2.1. Although CAT3 does not lower the absolute energy barriers of the ROP reaction in the presence of trimethylamine base, it steers the reaction toward the open chain product BM2 INT2.1.

The ROP of *L*-lactide was further evaluated using lithium methoxide as the base, both in the absence and presence of the CAT3, with the aim of further elucidating the interplay between catalyst-substrate binding modes and base identity (Figure

3.20).

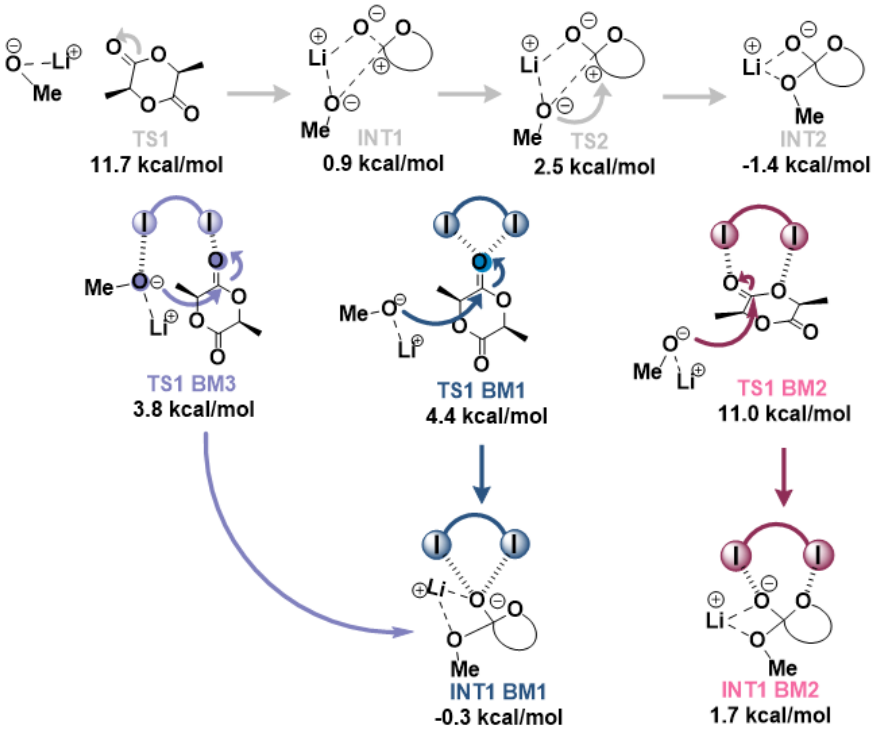

Figure 3.20: PES (ΔG kcal/mol) of the ROP of *L*-lactide initiated by lithium methoxide base in the absence (grey) and presence of CAT3 through various catalyst-substrate binding mode assemblies, BM1 (blue), BM2 (pink) and BM3 (purple).

The uncatalysed mechanism follows a stepwise pathway, whereas the CAT3-catalysed reaction proceeds in a concerted manner across all binding modes examined. In the presence of lithium methoxide base, CAT3-catalysed ROP is energetically more favourable relative to the uncatalysed pathway, as shown by the lower activation barriers, with BM3 remaining the most kinetically favourable binding mode, as previously found using trimethylamine base (Figures 3.19 and Figure 3.20).

Overall, these findings demonstrate the potential of XB-based catalytic frameworks, particularly those of bidentate design, in mediating and controlling the ROP of *L*-lactide in the presence of base. The dispersed interaction mode offered by bidentate catalytic scaffolds, exemplified by BM2 and BM3, enables multiple non-covalent anchor points between the catalyst and reactants. A dual-anchor point catalyst-substrate assembly allows for simultaneous stabilisation of different regions of the reaction complex, thereby facilitating both activation and directional control of

the polymerisation pathway. Furthermore, the study highlights the importance of co-catalytic base selection. While both trimethylamine and lithium methoxide were found to contribute to reaction control, the latter enhanced the kinetics of the system.

3.3.2.2 Characterisation of NCIs

Quantitative characterisation of each catalyst-monomer binding mode BM1-3 complex in the pre-TS assembly was carried out in the absence of base. The geometrically optimised structures were evaluated on the strength of the stabilising NCIs between the catalyst and the monomer. The stabilising XB interactions were quantitatively assessed using the QTAIM, focusing particularly on the electron density at the BCP ρ_{BCP}, which serves as a descriptor of XB strength and localisation (Figure 3.21).

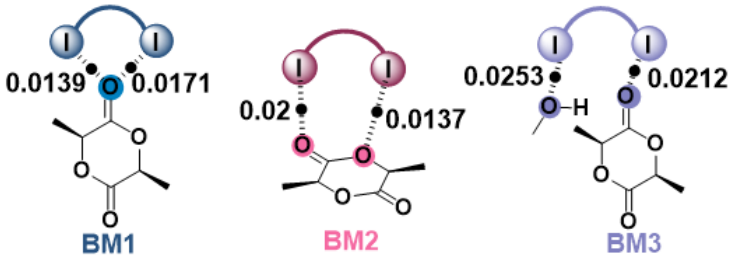

Figure 3.21: ρ_{BCP} (a.u.) for the O···X interaction within the catalyst-monomer binding mode assemblies BM1-3.

BM3 exhibited the highest ρ_{BCP} values, 0.0253 a.u. and 0.0212 a.u., and the most dispersed stabilisation profile, engaging multiple nucleophilic sites on both the *L*-lactide monomer and the methanol initiator. BM1, while bidentate in nature, exhibited lower ρ_{BCP} values, 0.0139 a.u. and 0.0171 a.u., indicative of weaker *L*-lactide monomer stabilisation. BM2 offered slightly more spatial dispersion than BM1; the dispersion stabilisation at different anchor points was limited to the *L*-lactide monomer, leaving the methanol initiator unstabilised. This observation challenges the conventional catalyst-substrate binding assembly BM1, indicating that substrate stabilisation is most effective through a spatially distributed network of XB-based anchor points, as observed in BM2 and BM3. These values support the

trends obtained in the PES study, as discussed in Section 3.3.2.1 Reactivity Studies, and further exemplify the varied efficiency of different catalyst-monomer binding configurations.

4 Hypervalent XB-Based Scaffolds

4.1 Introduction

Modulation of the XB-donor valency has emerged as a key design strategy. The transition from monovalent to hypervalent scaffolds has consequently produced a new class of XB catalysts with enhanced Lewis acidity and activation capability.[194,265–268]

Building on the electronic, structural, and binding orientation insights established in Chapter 3, Monovalent XB-based Scaffolds, the study was extended to experimentally validated hypervalent XB-based scaffolds.[265,266] The relatively rigid hypervalent scaffold features two σ-holes on the XB-donor surface, as illustrated in Figure 4.1, enabling multidirectional and cooperative NCIs. Recent advances, particularly involving iodolium ions, have demonstrated substantial improvement in catalytic activity and selectivity across diverse transformations.[194,265–268]

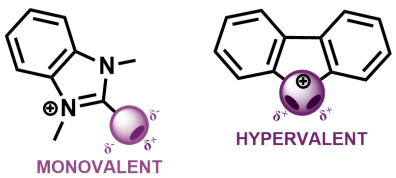

Figure 4.1: Positioning of the σ-hole in monovalent (left) and hypervalent (right) XB-based scaffolds.

The Michael addition of indole to *trans*-crotonophenone was used as a benchmark reaction (Figure 4.2) to directly assess how O-activation and π-type substrate binding extend from monovalent to hypervalent XB-based scaffolds.[157] Systematic scaffold

modulation was performed through steric and electronic variation, introducing electron-withdrawing and -donating substituents (–CF_3, –CH_3, *t*Bu, –OH, –OMe, –NO_2, –CN) to interrogate inductive and mesomeric effects.[269,270] Sulfur oxidation was further examined as a means of enhancing rigidity and electronic control.

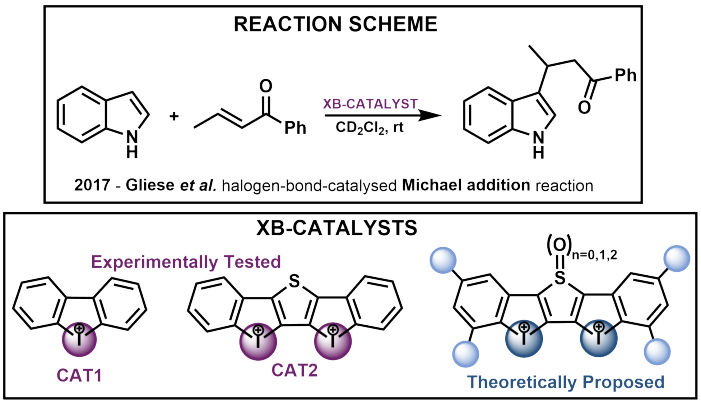

Figure 4.2: Michael addition of indole to *trans*-crotonophenone and theoretically proposed XB-based scaffold modulations (highlighted in light blue) positioned ortho and para to the XB-donor atom.

This study elucidates how enhanced XB strength and scaffold rigidity in hypervalent systems govern catalyst–substrate binding energetics, stabilisation, and catalytic performance. By direct comparison with monovalent analogues, it identifies the structural and electronic features that define optimal hypervalent XB catalyst design and assesses how binding-mode preferences and energetic trends evolve with increased valency.

4.2 Computational Details

The structures and systems under evaluation were optimised at the ωb97xd /def2-svp[246,247] computational level in room temperature. Harmonic vibrational frequencies were computed at the same level used for the geometry optimisations to confirm the nature of the stationary points as local minima. Single-point calculations were performed to improve the energy description at the computational level of ωB97x-D/def2-tzvp[195,246,248] computational level for the systems under study, namely, monomers, catalysts, and catalyst-substrate complexes. Structure optimisations

and energy calculations were performed using Gaussian 16.[249] The effective core potential def2-SVP basis set[195] has been used for the iodine atoms, where the tightly bound core electrons are replaced by an effective core potential, treating them as an effective potential, while more relevant valence electrons are treated explicitly.

Solvent effects were included in the optimisation by means of a continuum method, the SMD approach[250] in Gaussian16, using DCM as the solvent.

The reported free energies ($\Delta G_{\text{def2tzvp}}$) in this thesis were computed by adding the thermal correction (TC_{def2svp}) from the small basis set calculations to the electronic energy obtained from the higher level single point calculations (E_{def2tzvp}), as shown in Eq 1.

$$G_{\text{def2tzvp}} = E_{\text{def2tzvp}} + TC_{\text{def2tzvp}} \tag{1}$$

Relative energies (ΔG) were calculated as the difference between the energy of the optimised complex (G_{complex}) and the energy of each monomer (G_{monomer}) in its optimised geometry as shown in Eq 2.

$$\Delta G = G_{\text{complex}} - \sum G_{\text{monomer}} \tag{2}$$

The MEP of the isolated monomers was calculated on the electron density isosurface of 0.001 a.u. This isosurface was shown to resemble the van der Waals surface.[239] These calculations were carried out using Gaussian16 software, and the numerical results were analysed using the Multiwfn program[251] and plotted using Jmol.[252]

The NBO[253] methodology version 7 was used to evaluate the strength of individual interactions by measuring the charge transfer between occupied and unoccupied orbitals within different fragments. The calculations were performed at the same level of theory as the geometry optimisations: ωb97xd /def2-svp.

The QTAIM methodology[254,255] was used to analyse the electron density of the

systems within the AIMAll software, and the electron density at the BCPs was extracted from the various systems upon complexation. The calculations were performed at the same level of theory as the geometry optimisations: ωb97xd /def2-svp.

4.3 Results & Discussion

4.3.1 Michael Addition of Indole to *trans*-Crotonophenone

4.3.1.1 Electronic Properties

The electronic effects of scaffold modification were quantified by MEP analysis to evaluate σ-hole depth and distribution on the iodine(III) XB donor, key descriptors governing halogen-bond strength and catalytic efficiency. As shown in Figure 4.3, introduction of an electron-withdrawing group (EWG) –CF3, at the ortho-para position, CAT3b, relative to unfunctionalised CAT2, increases the σ-hole electropositivite potential Vmax from 262 kcal/mol to 285 kcal/mol. The introduction of electron-donating group (EDG) –CH3, CAT4a and CAT4b, reduced the electropositive potential Vmax, 257 kcal/mol and 254 kcal/mol respectively, indicating a diminished capacity to engage in strong XB interactions. Furthermore, steric perturbation introduced by the bulky tert-butyl group, CAT5a and CAT5b, led to the partial obstruction of the lateral σ-holes and reduced electropositive potential Vmax values, 251 kcal/mol and 248 kcal/mol, respectively.

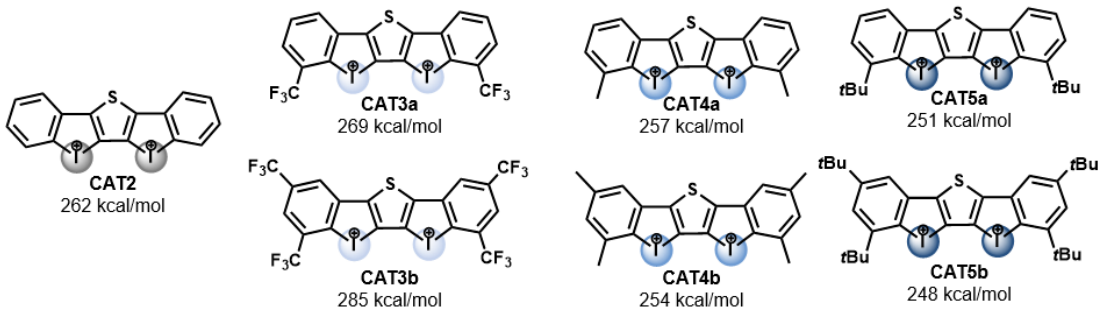

Figure 4.3: MEP on the 0.001 a.u. electron density isosurface and the maxima ($V_{\max}$) values of the MEP in kcal/mol for CAT2-5b.

The promising σ-hole enhancement effect of EWG substituents, CAT3a and CAT3b, served as a rationale for further electronic fine-tuning of the catalyst framework. Subsequently, a series of alternative, strongly EWGs, -NO_2 and -CN, were incorporated and systematically evaluated (Figure 4.4).

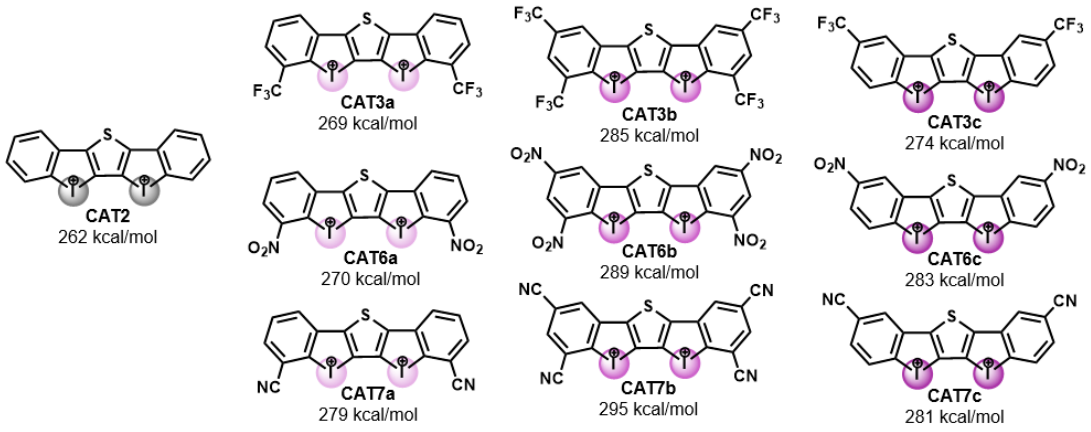

Figure 4.4: MEP on the 0.001 au electron density isosurface and the maxima (V_{max}) values of the MEP in kcal/mol for the para, ortho, ortho-para substituted CAT3a-CAT7c.

Para-functionalisation enhances σ-hole depth more effectively than ortho-functionalisation. This effect is particularly pronounced in the CAT3 and CAT6 series, relative to the ortho-functionalisation, para-functionalised variants exhibit increases in σ-hole depth of +5.0 kcal/mol (CAT3a and CAT3c) and +13 kcal/mol (CAT6a and CAT6c). Unlike the para-functionalised scaffolds (CAT3c, CAT6c and CAT7c) the ortho-functionalised scaffolds (CAT3a, CAT6a and CAT7a) can potentially engage in intramolecular NCIs with the XB-donor atom, in principle resulting in the reduction of σ-hole intensity.

Increasing EWG strength further deepens the σ-hole, with CAT6b and CAT7b exhibiting +4 kcal/mol and +10 kcal/mol increases relative to CAT3b. Unlike the trends for the ortho-functionalised scaffolds, the trends for the para-substituted series (CAT3c, CAT6c and CAT7c) are consistent with the expected EWG strength trends found in literature, -NO_2 > -CN > -CF_3.[271]

As previously demonstrated, the functionalisation of the catalytic scaffold with a –CF_3 group has a pronounced impact on catalytic performance, primarily due to its

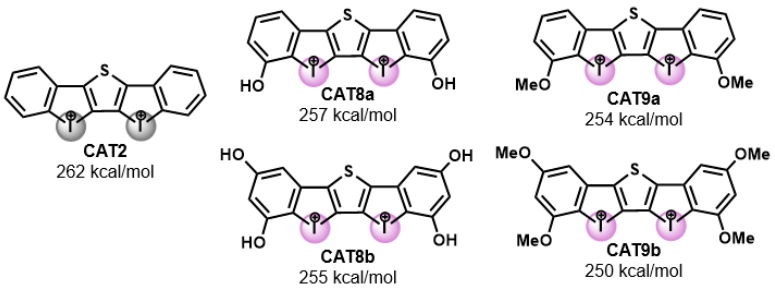

Figure 4.5: MEP on the 0.001 au electron density isosurface and the maxima (V_{max}) values of the MEP in kcal/mol for CAT2 and CAT8a-CAT9b.

strong inductively electron-withdrawing character. This behaviour arises from the polarisation of the Ar–C bond,[271] which contributes to an increased electropositive potential at the σ-hole of the iodine centre. Subsequently, further investigation was undertaken to explore the electronic effects of electronic conjugation, particularly in relation to the directional nature of XB interactions governed by the electron-deficient belt located at iodine's π-orbitals, which favour near-linear geometries ($\sim$180°).[107,272] To probe the influence of electronic donation through conjugation, functional groups, –OH (CAT8) and –OMe (CAT9), were selected. These groups are known to exhibit both mesomeric electron-donating effects (+M) and, to a lesser extent, inductive electron-withdrawing behaviour (-I).[273] The interplay of these effects on modulating the σ-hole depth was evaluated. Relative to the unfunctionalised scaffold CAT2 (Figure 4.5), both the CAT8 and CAT9 series exhibit consistent reductions in σ-hole V_{max}, indicating that mesomeric electron donation outweighs inductive withdrawal, resulting in σ-hole reduction.

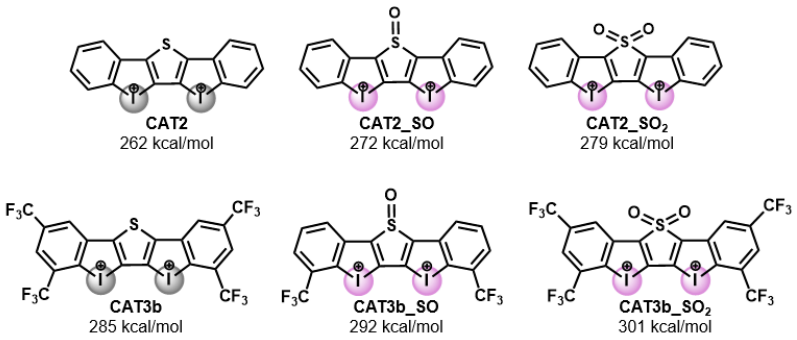

Figure 4.6: MEP on the 0.001 au electron density isosurface and the maxima (V_{max}) values of the MEP in kcal/mol for CAT2 and CAT3b, varying in sulfur oxidation.

Previous literature reports indicate that sulfur oxidation in dithienothiophenes markedly increases electron deficiency, leading to deeper σ-holes and enhanced catalytic potential.[190,266] Drawing inspiration from these findings, sulfur oxidation was applied to the current XB-based scaffolds. Specifically, this approach was implemented on both CAT3b and the unfunctionalised reference scaffold, CAT2. As shown in Figure 4.6, sulfur oxidation increases σ-hole depth. Most notably, the doubly oxidised derivative of the CAT3b scaffold, CAT3b–SO_2, had a relatively high V_{max} value associated with the σ-hole of 301 kcal/mol. Similarly, the doubly oxidised derivative of the CAT2 unfunctionalised scaffold, CAT2–SO_2, had an increased V_{max} value associated with the σ-hole of 272 kcal/mol. These results demonstrate that sulfur oxidation leads to enhancement in electron deficiency, thereby resulting in deeper σ-holes.

4.3.1.2 Reactivity Studies

Motivated by the mechanistic relevance of both π-type and O-activation modes,[114,157], the preferred binding orientations of experimentally validated[265,267] CAT1 and CAT2 were systematically investigated. Additionally, a series of functionalised CAT2 scaffolds has been included in the study, as seen in Section 4.3.1.1 Electronic Properties.

In the case of the monodentate CAT1, a series of binding modes were systematically investigated as shown in Figure 4.7, in addition to the previously explored O- (M3) and π-type (M2) activation modes. Additional configurations, M1 and M4, were considered. Both inspired by π-type activation (M2), targeting alternative points of interaction along the conjugated π-system of the indole substrate (π_{indole}). Computational attempts to identify TSs proved unsuccessful for both M1 and M4, indicating that such π_{indole}-based binding modes do not facilitate the reaction. Furthermore, the activation barriers calculated (Figure 4.8) for the π-type (M2) and O-type (M3) binding modes, 42.5 kcal/mol and 39.9 kcal/mol, respectively, were found to be higher than that of the uncatalysed reaction barrier at 40.0 kcal/mol. These results

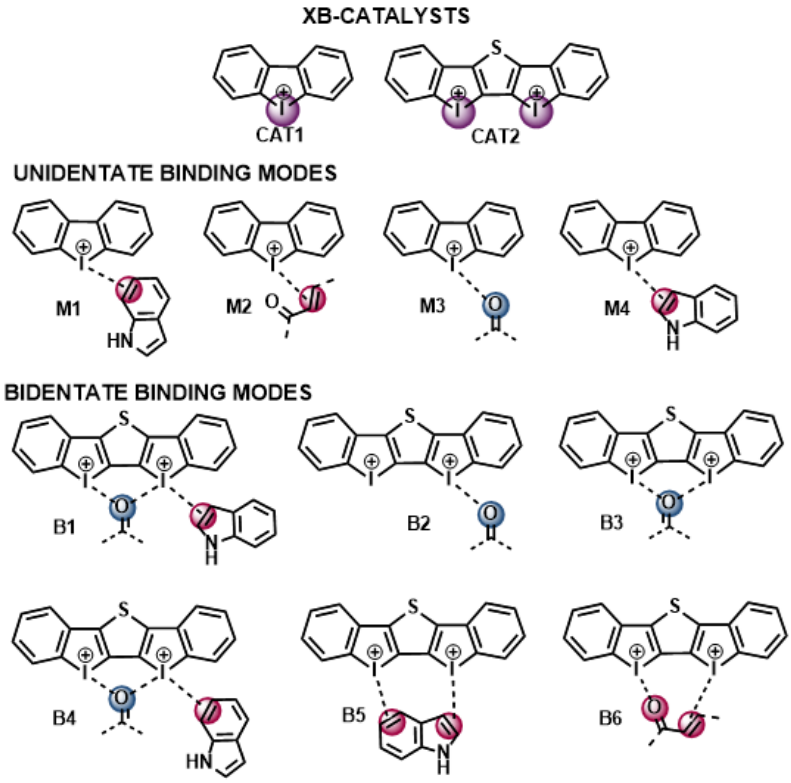

Figure 4.7: Summary of all the catalyst-substrate binding modes explored within the monodentate CAT1 and bidentate CAT2.

suggest that CAT1 fails to exert any catalytic effect on the reaction, aligning with experimental observations reported in the literature, wherein CAT1 was found to be catalytically inactive.[267]

For the bidentate CAT2-CAT5, two variations of the O-type activation mode (B2 and B3) were examined alongside a classical π-type activation mode (B6). Additionally, a series of alternative binding configurations (B1, B4, and B5) were devised based on the π_{indole} activation strategy, aiming to explore extended interactions with the conjugated π-system of the indole substrate (Figure 4.7). The π_{indole}-based, B1, B4, and B5, were found to be ineffective, as the TS could not be computationally located under the conditions studied. In the case of relatively rigid hypervalent XB-based scaffolds, which impose geometric and electronic constraints, π-focused NCIs are insufficient for enabling effective substrate stabilisation. Among the remaining, TS-accessible binding modes (B2, B3, and B6), only the O-type B3 consistently lowers the activation barrier relative to the uncatalysed barrier of 40 kcal/mol (Figure 4.8).

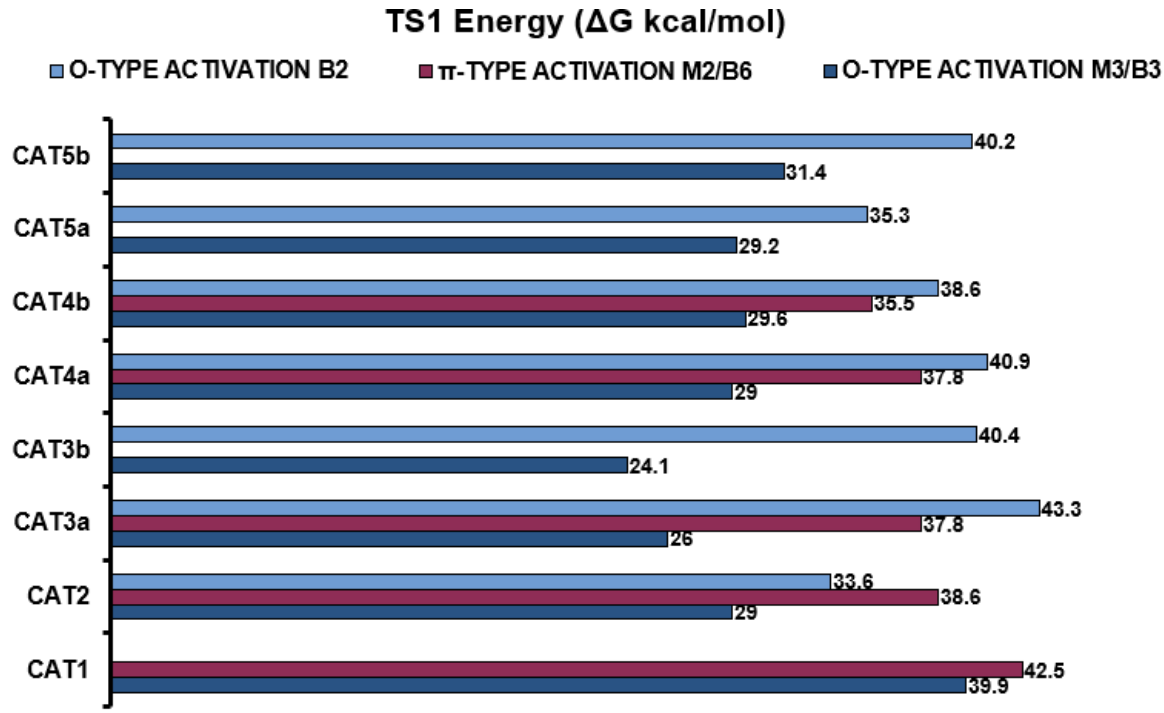

Figure 4.8: TS energy (ΔG kcal/mol) for TS1 of the Michael addition of indole to *trans*-crotonophenone under the catalysis of CAT1-5b with various binding modes considered; O-type B2 (light blue), O-type M3/B3 (dark blue) and π-type M2/B6 (red).

Building on the established preference for the O-type B3 binding mode within the bidentate systems (CAT2–CAT5), binding mode B3 was adopted as the structural basis for further energetic investigation on the remaining modulated bidentate systems. Referring to Figure 4.9, the electron-deficient scaffolds, CAT3a and CAT3b, reduced the activation barrier beyond that observed for the unfunctionalised CAT2 (29.0 kcal/mol), with barrier reductions of -3.0 kcal/mol and -4.9 kcal/mol, respectively. Conversely, CAT4a-CAT5b led to relatively higher transition state energies.

Scaffolds of increasingly electron-withdrawing modulations, CAT3, CAT6 and CAT7 underscore the efficiency of ortho-para-functionalisation, as exemplified by activation barriers 24.1 kcal/mol, 25.4 kcal/mol, and 25.1 kcal/mol, respectively (Figure 4.10). The calculated transition state energies reveal a modest but consistent preference for ortho-functionalisation over para-substitution. This effect is particularly notable in CAT3 (ΔΔG = -0.7 kcal/mol) and CAT6 (ΔΔG = -1.1 kcal/mol). Moreover, a general trend in catalytic performance emerges based on the nature of the EWG,

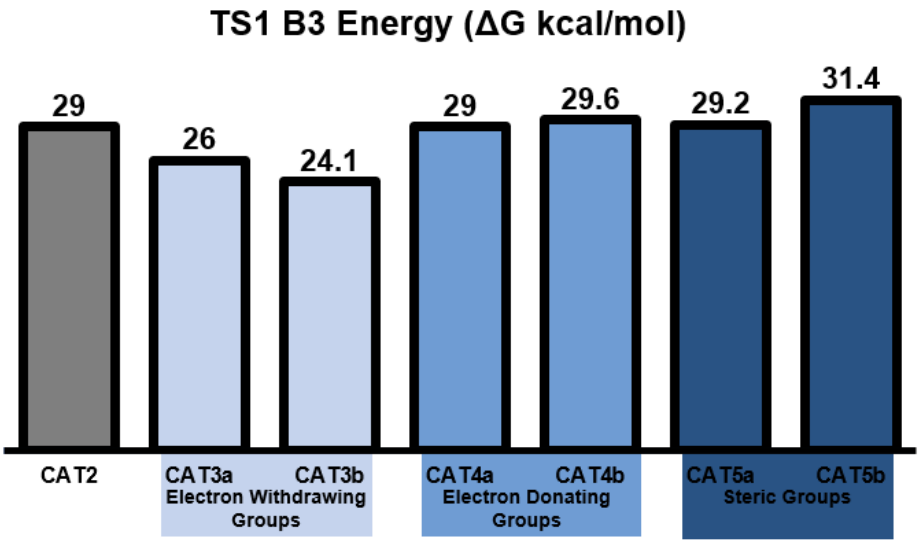

Figure 4.9: TS energy (ΔG kcal/mol) for TS1 of the Michael addition of indole to *trans*-crotonophenone under the catalysis of CAT2-5b, binding mode B3.

following the order -CF_3 > -CN > -NO_2. The preference for ortho-substitution may originate from a more favourable spatial orientation of the electrophilic site relative to the reactive centre of the substrate, thereby improving catalytic engagement. All EWG-functionalised scaffolds (CAT3a–b, CAT3c, CAT6, and CAT7) reduce the activation barrier by 12.6–15.9 kcal/mol, underscoring the role of EWG strength and positioning in enhancing the efficiency of hypervalent XB-based catalysts.

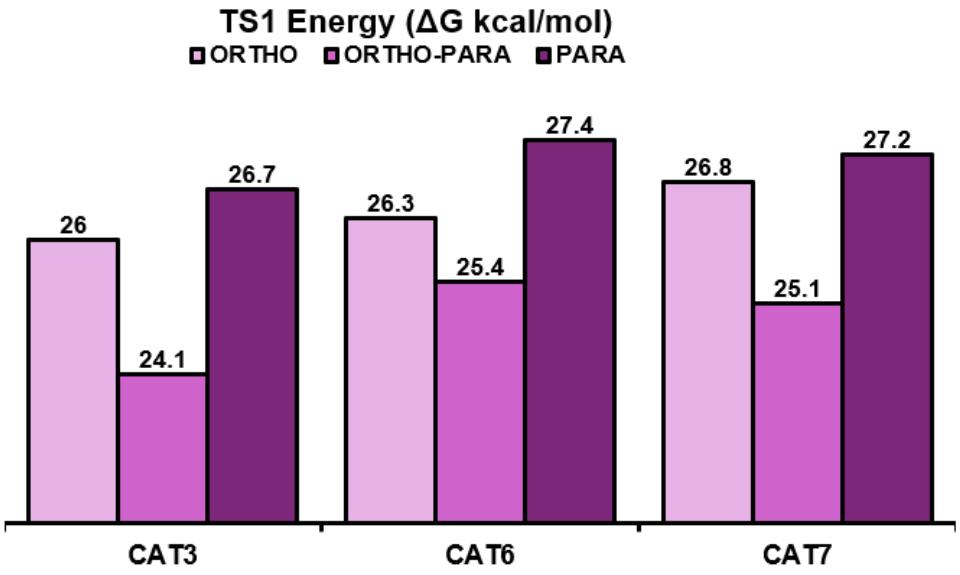

Figure 4.10: TS energy (ΔG kcal/mol) for TS1 of the Michael addition of indole to *trans*-crotonophenone under the catalysis of CAT3, CAT6 and CAT7, binding mode B3.

Mesomerically donating substituents, –OH (CAT8a-b) and –OMe (CAT9a-b), reduce σ-hole depth (Figure 4.5). To assess whether this translates into altered reactivity, activation barriers were calculated for CAT8a–9b (Figure 4.11). Relative to unfunctionalised, CAT2, CAT8a and CAT9a show minimal barrier changes, whereas CAT9b exhibits a 2.7 kcal/mol increase. These results indicate that although mesomeric donation substantially decreases σ-hole depth, its impact on reaction energetics is more nuanced.

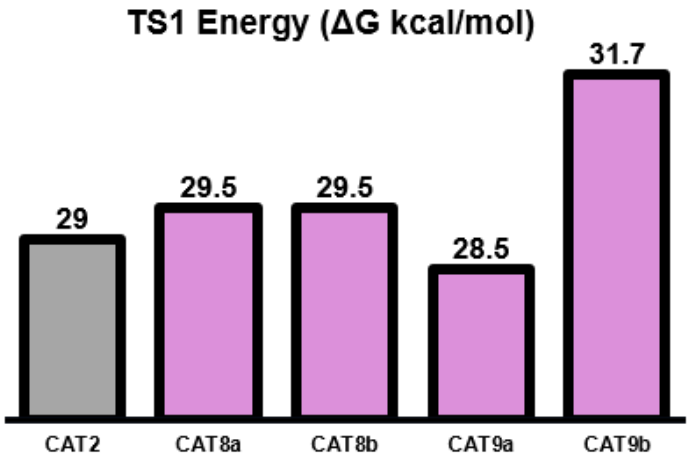

Figure 4.11: TS energy (ΔG kcal/mol) for TS1 of the Michael addition of indole to *trans*-crotonophenone under the catalysis of CAT2 and CAT8a-9b, binding mode B3.

Activation barrier calculations for sulfur-oxidised scaffolds align closely with the MEP trends (Figure 4.6). The doubly oxidised CAT2–SO_2 exhibits the lowest barrier among all catalysts at 20.9 kcal/mol (Figure 4.12), corresponding to a 19.1 kcal/mol reduction in transition state energy relative to the uncatalysed reaction (40 kcal/mol).

The energetic improvements were not linear across the oxidation sequence. The first oxidation step, from CAT3b to CAT3b–SO, resulted in a modest reduction in transition state energy of just 0.6 kcal/mol. The second oxidation, from CAT3b to CAT3b–SO_2, produced a more substantial decrease of 3.2 kcal/mol. This non-linear progression suggests diminishing returns following initial oxidation, aligning with the expected electronic behaviour captured by Hammett parameters for sulfoxides and sulfones.[274] Collectively, these results illustrate that sulfur oxidation is a poten-

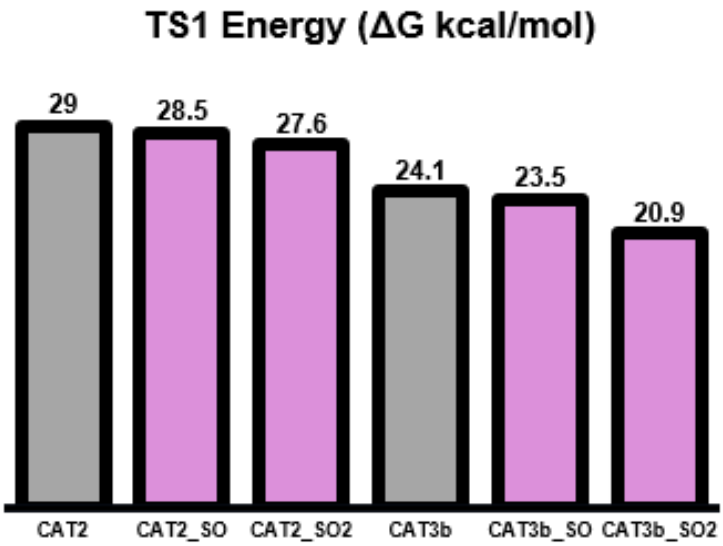

Figure 4.12: TS energy (ΔG kcal/mol) for TS1 of the Michael addition of indole to *trans*-crotonophenone under the catalysis of CAT2 and CAT3b, varying in sulfur oxidation, binding mode B3.

tially promising strategy for tuning the electron deficiency and thereby the efficiency of hypervalent XB-based catalysts.

4.3.1.3 Characterisation of NCIs

QTAIM analysis was performed to characterise and verify the NCIs present in the catalyst–substrate complexes. The ρ_{BCP} values for the O$\cdots$I XB were plotted against interatomic distance, revealing a strong linear correlation ($R^2 = 0.97$), Figure 4.13. This confirms the expected inverse relationship between distance and electron density at the BCP seen in NCIs, with shorter O$\cdots$I contacts corresponding to stronger interactions.

Catalyst–substrate stabilisation was further analysed by NBO calculations, which quantify CT interactions through second-order perturbation energies, $E(2)$ (Figure 4.14). The dominant interaction arises from donation of the substrate O lone pair O (LP) into the σ-hole of the XB donor, represented antibonding orbital, I (BD*). The $E(2)$ energies for substrate-stabilising O(LP)$\rightarrow$I(BD*) CT interactions are summarised in Figure 4.15.

EWG-functionalised scaffolds generally exhibit stronger substrate stabilising CT,

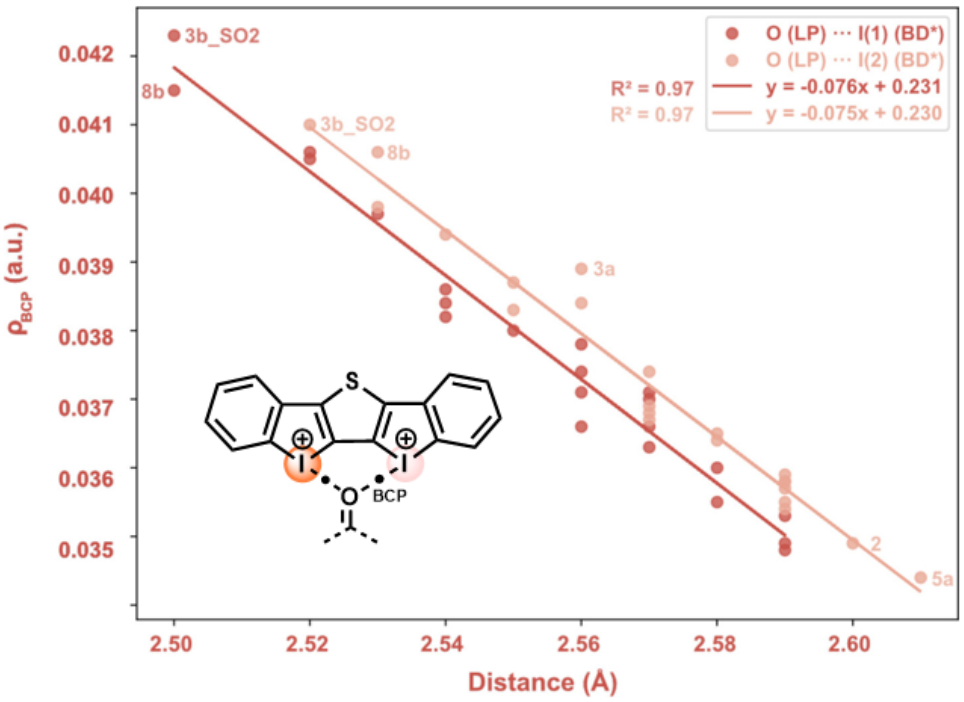

Figure 4.13: Correlation between ρ_{BCP} (a.u.) and the distance between interacting atoms (Å).

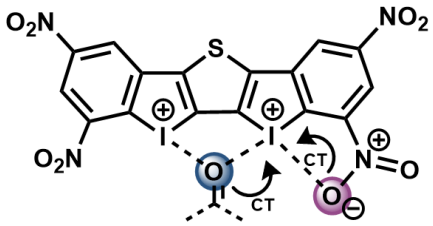

Figure 4.14: Schematic representation of intermolecular O (LP)$\cdots$I (BD*) in B3 binding mode (blue) and intramolecular O (LP)$\cdots$I (BD*) interactions (purple) CT in the ortho-substituted scaffolds, exemplified by CAT6b.

CAT6b had the highest $E(2)$ value (55.82 kcal/mol), marginally exceeding CAT3b–SO_2 (54.61 kcal/mol, despite the latter exhibiting the lowest activation barrier (Figure 4.12).

NBO analysis was extended to intramolecular interactions within ortho-functionalised scaffolds (Figure 4.14). In CAT3b, the fluorine lone pair F(LP) engages in intramolecular CT with an $E(2)$ value of 8.27 kcal.mol, CAT6b exhibits substantially stronger intramolecular CT of 24,0 kcal/mol between the nitro-group oxygen O(LP) and the XB-donor BD* orbital. No analogous intramolecular interaction is observed for the

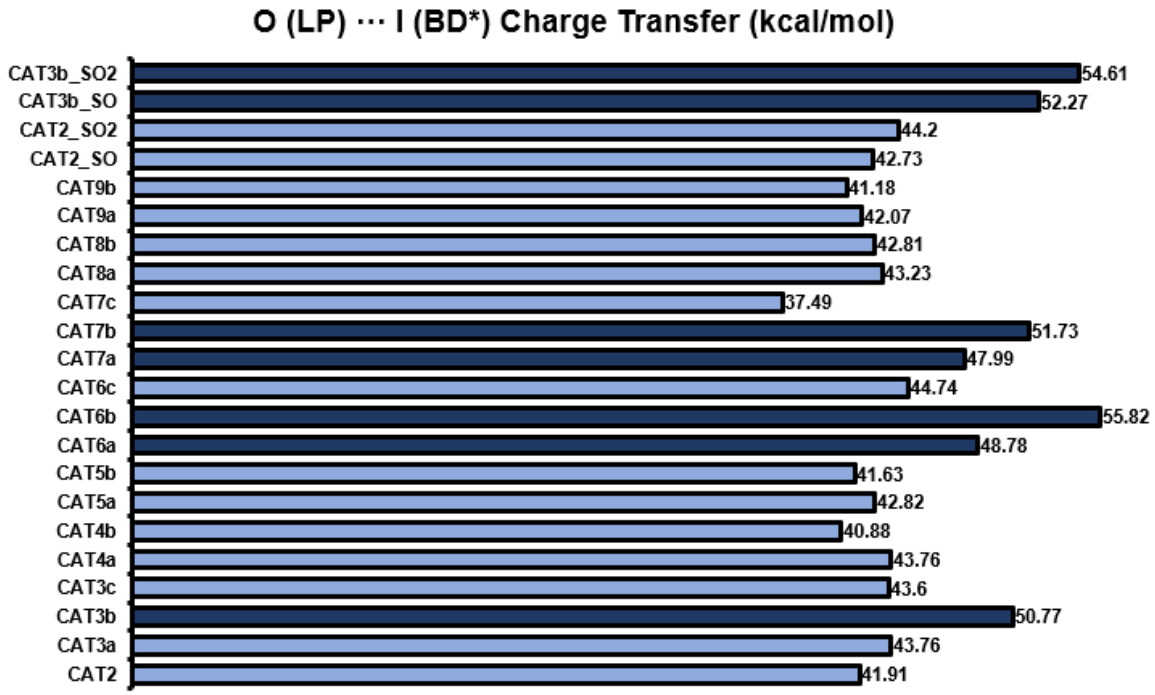

Figure 4.15: Total *E(2)* values (kcal/mol) corresponding to the CT O(LP)· · · I(BD*) in B3 binding mode for catalysts under study.

cyano-substituted CAT7b (Figure 4.16). As discussed in Section 4.2.1.1 Electronic Properties, the σ-hole trends for ortho-functionalised scaffolds (CAT3a–b, CAT6a–b, CAT7a–b; Figure 4.4) deviate from the expected EWG strength order (–NO_2 > –CN > –CF_3) reported in literature.[271] The $E(2)$ values associated with intramolecular NCIs between the ortho-positioned substituent and the XB-donor atom offer a plausible explanation for the electronic observations found in ortho-functionalised scaffolds, such as smaller σ-hole depth and divergence from expected EWG strength order (Figure 4.4 and Figure 4.16).

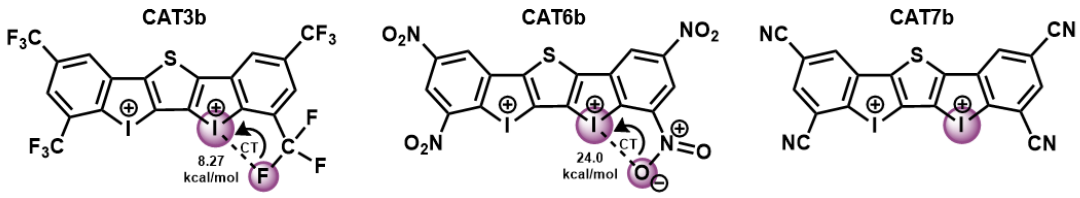

Figure 4.16: *E(2)* values (kcal/mol) corresponding to the intramolecular CT (purple) from the ortho-positioned functional group to the I(BD*) in CAT3b, CAT6b and CAT7b.

Moreover, these results highlight the importance of substituent positioning. Ortho-

positioned substituents can engage in intramolecular NCIs with the XB-donor atom in hypervalent XB-based scaffolds, thus influencing the electronic properties of the XB-donor atom. The spatial arrangement of substituents relative to the XB-donor atom is critical for modulating the activity of hypervalent XB-based scaffolds and should be carefully considered.

5 | Counterion-Induced Conformational Effects in Catalysts

5.1 Introduction

This chapter examines the role of NCIs in substrate stabilisation, focusing on cooperative intramolecular effects involving the XB-donor atom and on how counterions influence the conformational landscape of the catalytic scaffold. Building on recent work by Bugaut *et al.*,[275] who proposed intramolecular cooperativity through proximal HB-donor motifs in monovalent cationic XB catalysts, this study investigates the hypothesised hydrogen-bond-enhanced halogen bonding (HBeXB) model. Understanding this cooperative enhancement is important for rational catalyst design, as it provides a means to modulate interaction strength, improve substrate binding, and ultimately enhance catalytic performance.

Intramolecular HB is introduced to amplify XB strength by modulating the electronic environment of the XB-donor atom.[275] Cooperative HB/XB effects are well documented across both biological and synthetic systems, where HB can reinforce, preorganise, or otherwise enhance XB interactions. In synthetic chemistry, this cooperation has been observed in several scenarios, including parallel HB and XB interactions with a common substrate, HB-preorganised XB scaffolds that promote favourable geometries, HB-assisted XB that strengthens donor–acceptor interactions, and XB-assisted HB assemblies that improve overall catalytic activity. Collectively, these

examples demonstrate that such NCIs can substantially increase binding strength and reactivity. The design and optimisation of catalysts incorporating the cooperative effect has therefore emerged as a promising strategy, with bifunctional HB/XB architectures offering well-defined geometric and electronic control over substrate stabilisation.[276–281]

While intramolecular NCIs can potentially enhance the XB, the overall strength and directionality are further governed by the catalytic scaffolds charge distribution and, consequently, by the presence of counterions. The transition from neutral to cationic XB-based catalyst systems has emerged as a widely adopted design approach, as cationic systems generate deeper σ-holes and stronger XB interactions, leading to enhanced catalytic performance.[95,282–284] Charge neutrality in such systems necessitates counterions, which are often neglected in computational studies due to cost or assumed weak coordination. However, growing evidence demonstrates that counterions can engage in meaningful NCIs, including HB, ion pairing, and π–π interactions, substantially influencing catalyst conformation and electronic structure.[285–290] Additionally, omitting counterions in continuum solvation models can introduce artefacts arising from imbalanced charge distributions.[291]

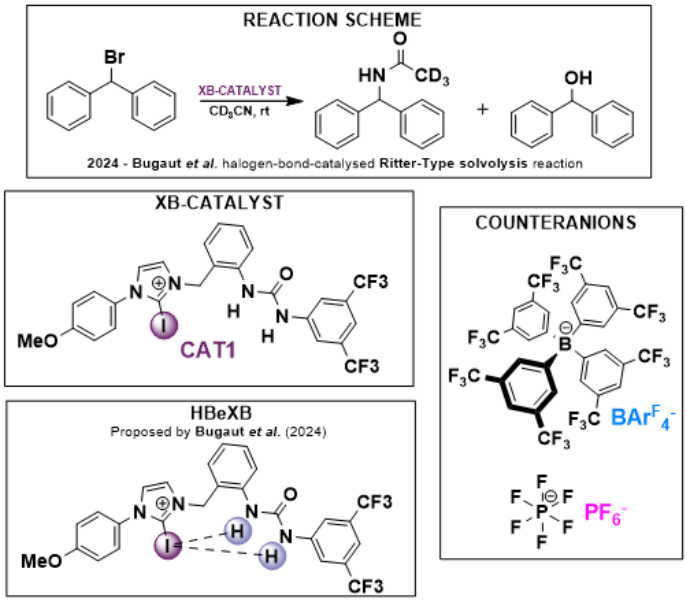

Figure 5.1: CAT1 catalysed Ritter-type solvolysis highlighting counterion effects (PF_6^-, $BArF_4^-$) and the proposed HBeXB interaction.

Motivated by the growing recognition of counterion effects and the strict conformational requirements for intramolecular cooperativity in bifunctional catalytic scaffolds, this study systematically examines the experimentally validated CAT1 scaffold bearing HB-donor functionalities (Figure 5.1).[275] Non-coordinating counterions of differing size, PF_6^- and $BArF_4^-$, are evaluated for their influence on the conformational landscape and accessibility of the XB donor site. The presence and strength of the proposed HBeXB interaction and its impact on the free-energy profile of a Ritter-type solvolysis are examined in terms of XB-donor accessibility and σ-hole depth. Collectively, these results reveal the decisive role of counterions in governing catalyst geometry and reactivity, underscoring the need for their explicit inclusion in computational models of XB catalysis.

5.2 Computational Details

The structures and systems under evaluation were optimised at the M06-2X/def2-svp computational level with Grimme's D3 dispersion correction at room temperature.[292–297] This accounts for atom–pairwise dispersion contributions, including three-body terms. This correction is essential for obtaining a quantitatively accurate description of XB-based interactions, sensitive to dispersion and polarisation effects, providing a balanced and cost-effective approach for modelling NCIs in the iodine-containing systems under evaluation. Harmonic vibrational frequencies were computed at the same level used for the geometry optimisations to confirm the nature of the stationary points as local minima. Single-point calculations were performed to improve the energy description at the computational level of M06-2X/def2-tzvp[292–297] computational level for the systems under study, namely, monomers, catalysts, and catalyst-substrate complexes. Structure optimisations and energy calculations were performed using Gaussian 16.[249] The effective core potential def2-SVP basis set[195] has been used for the iodine atoms, where the tightly bound core electrons is replaced by an effective core potential, treating them as an

effective potential, while more relevant valence electrons are treated explicitly.

Solvent effects were included in the optimisation by means of a continuum method, the SMD approach[250] in Gaussian16 with refined SMD18 parameters for iodine atoms (2.74 Å)[298], using acetonitrile as the solvent.

The reported free energies ($\Delta G_{\text{def2tzvp}}$) in this thesis were computed by adding the thermal correction (TC_{def2svp}) from the small basis set calculations to the electronic energy obtained from the higher level single point calculations (E_{def2tzvp}), as shown in Eq 1.

$$G_{\text{def2tzvp}} = E_{\text{def2tzvp}} + TC_{\text{def2tzvp}} \tag{1}$$

Relative energies (ΔG) were calculated as the difference between the energy of the optimised complex (G_{complex}) and the energy of each monomer (G_{monomer}) in its optimised geometry as shown in Eq 2.

$$\Delta G = G_{\text{complex}} - \sum G_{\text{monomer}} \tag{2}$$

The MEP of the isolated monomers was calculated on the electron density isosurface of 0.001 a.u. This isosurface was shown to resemble the van der Waals surface.[239] These calculations were carried out using Gaussian16 software and the numerical results were analysed using the Multiwfn program[251] and plotted using Jmol.[252]

The NBO[253] methodology version 7 was used to evaluate the strength of individual interactions by measuring the charge transfer between occupied and unoccupied orbitals within different fragments. The calculations were performed at the same level of theory as the geometry optimisations: M06-2X/def2-svp.

The QTAIM methodology[254,255] was used to analyse the electron density of the systems within the AIMAll software, and the electron density at the BCPs (BCPs) was extracted of the various systems upon complexation. The calculations were

performed at the same level of theory as the geometry optimisations: M06-2X/def2-svp.

The conformational space of the catalyst in the absence and presence of counterions was searched using Conformer-Rotamer Ensemble Sampling Tool (CREST) version 2.11.[299], a package which works with the semi-empirical tight binding (xTB) program.[300] The conformational space of a given molecule is optimised and subsequently explored using a conformer search using the iMTD-GC algorithm utilising a combination of root-mean-square deviation (RMSD) metadynamics simulations and semiempirical calculations.[301] This RMSD calculations were performed using calculate_rmsd[302] package. The Hungarian algorithm[303] was used as the atomic reordering method and the Kabsch algorithm[304] was used as the system rotation method. The conformers generated were optimised using xTB version 6.4.0, with GFN2-xTB parametrised tight-binding model and the ALPB implicit solvation model.[305–307] The results were filtered using a RMSD of 8.0 Å and an energy difference of 5.0 kcal/mol. Following this, the Boltzmann populations were calculated at rt and further filtered if below 0.1% population.

5.3 Results & Discussion

5.3.1 Conformational Analysis

The study commenced with an exploration of the conformational landscape of the monovalent scaffold CAT1. Owing flexible nature of the CAT1 scaffold, conformational analysis is essential to assess how the relative spatial arrangement of key functional groups, namely the urea and azolium units, influences catalytic behaviour. The analysis revealed a diverse conformational ensemble, with the urea moiety adopting three primary arrangements: (anti,anti), (anti,syn), and (syn,anti). The relative orientation of the azolium with respect to the urea is described as *cis* when both groups are oriented in the same direction and *trans* when oppositely oriented

(Figure 5.2).

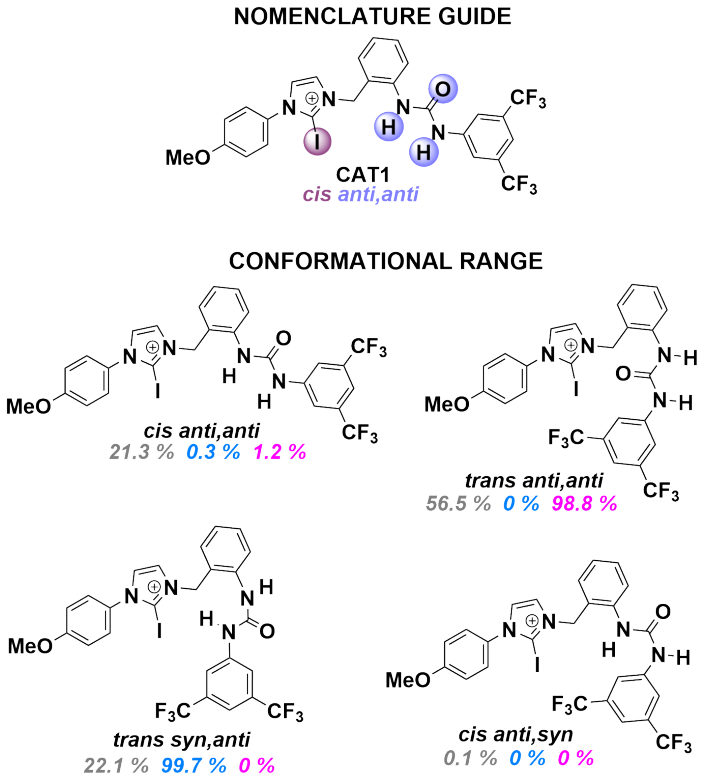

Figure 5.2: Orientations found for CAT1 in the absence and presence of counteranions $BArF_4^-$ and PF_6^-. Boltzmann population % displayed for isolated CAT1 (grey), in the presence of $BArF_4^-$ (blue) and PF_6^- (pink).

The conformational landscape of isolated CAT1 is summarised in Figure 5.2. Multiple conformers were identified, with four distinct arrangements exhibiting Boltzmann populations exceeding 0.1%. Consistent with literature, CAT1 shows a strong preference for the (anti,anti) urea conformation.[308] In addition, a general preference for a *trans*-orientation of the imidazolium moiety is observed. Overall, isolated CAT1 displays a relatively broad conformational ensemble comprising several closely populated structures.

To probe the influence of counterions on this flexibility, the analysis was extended to CAT1 complexed with PF_6^- and $BArF_4^-$, two commonly employed anions of differing size.[275,309] Complexation with either counterion substantially reduced the accessible conformational space, as shown in Figure 5.3. For $1{\cdot}PF_6^-$, two conformers were identified: a major structure featuring a *trans*-oriented azolium and an (anti,anti) urea motif, and a minor *cis* (anti,anti) arrangement. A comparable restriction was

observed for 1·$BArF_4^-$, which also exhibited two distinct conformers; the major species featuring a *trans* azolium orientation and a (syn,anti) urea conformation.

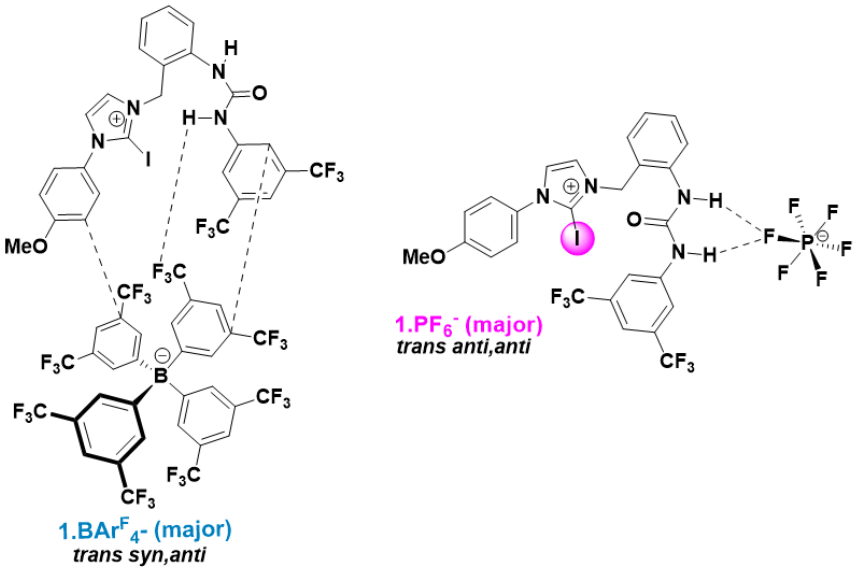

Figure 5.3: Visual depiction of the primary NCIs in the major CAT1 conformers in the presence of $BArF_4^-$ (blue) and PF_6^- (pink).

Counterions were found to exert a pronounced and differentiable influence on scaffold preorganisation. While PF_6^- largely preserves the *trans* (anti,anti) conformational preference also seen for the isolated CAT1, $BArF_4^-$ induces a conformational shift within the urea motif, highlighting the role of counterion identity in modulating catalyst geometry.

Table 5.1: Total CT (kcal/mol) and BCPs (a.u.) representative of the intermolecular interaction, N-H (BD*) ···· F (LP), N-H from the urea-motif in CAT1 **1** and F from the counterion.

System	Population (%)	Total BCP	CT
1·$\mathbf{PF_6^-}$ (major)	98.8	0.0438	15.01
1·$\mathbf{PF_6^-}$ (minor)	1.2	-	-
1·$\mathbf{BAr^F{}_4^-}$ (major)	99.7	0.0120	2.72
1·$\mathbf{BAr^F{}_4^-}$ (minor)	0.3	-	-

The origin of the conformational preferences and the role of counterion complexation was investigated through NBO and QTAIM analyses. Major conformer complexes exhibited stabilising intermolecular HBs between the CAT1 urea N–H and counterion

F atoms. The associated CT energies and BCP parameters are summarised in Table 5.1.

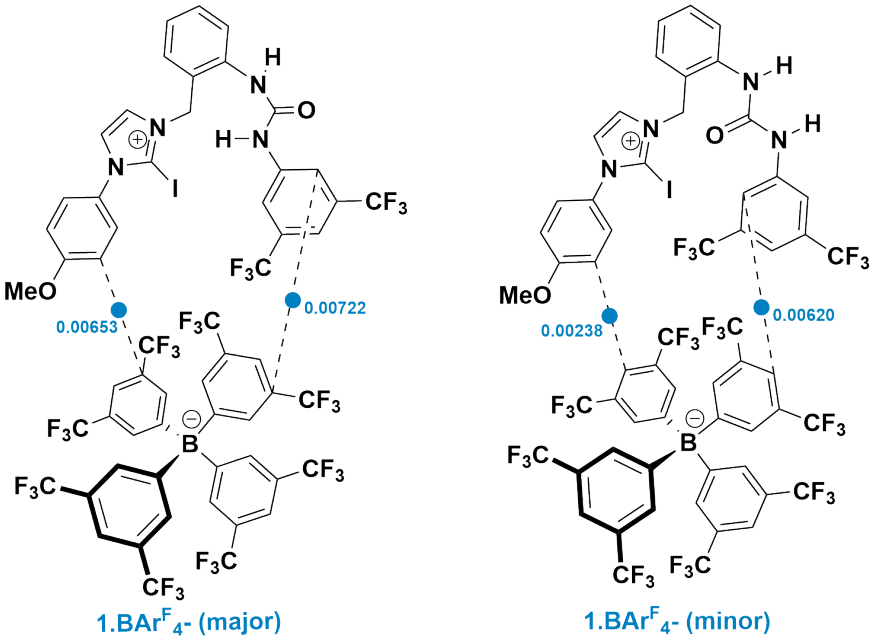

Figure 5.4: Visual depiction of the π-π stacking interactions between CAT1 and $BArF_4^-$. The ρ values (a.u.) at relevant BCPs are denoted in blue.

The $1{\cdot}PF_6^-$ (major) conformer is stabilised by a bidentate HB interaction between the CAT1 urea and PF_6^-, enabled by the (anti,anti) urea orientation and resulting in a CT of 15.01 kcal/mol. The $1{\cdot}PF_6^-$ (minor) conformer lacks such interactions and is therefore weakly populated (1.2%). Similarly, the $1{\cdot}BArF_4^-$ (major) conformer is stabilised by a single urea–counterion HB (99.7% population), whereas the minor conformer lacks comparable interactions and is negligibly populated (0.3%).

Additionally, $BArF_4^-$ interacted with CAT1 through π-π stacking interactions, as illustrated in Figure 5.4. QTAIM analysis was used to quantify the π-π stacking interactions. $1{\cdot}BArF_4^-$ (major) had BCP densities of 0.00653 and 0.00722 a.u., facilitated by a (syn,anti) urea orientation rather than the typical (anti,anti) arrangement. The $1{\cdot}BArF_4^-$ (minor) conformer exhibits weaker π–π stacking interactions (0.00238 and 0.00620 a.u.).

The HBeXB cooperative intramolecular interaction, specifically a HB between the urea and iodoazolium as shown in Figure 5.5, proposed by Bugaut *et al.*[275] was

explored using QTAIM and NBO analyses.

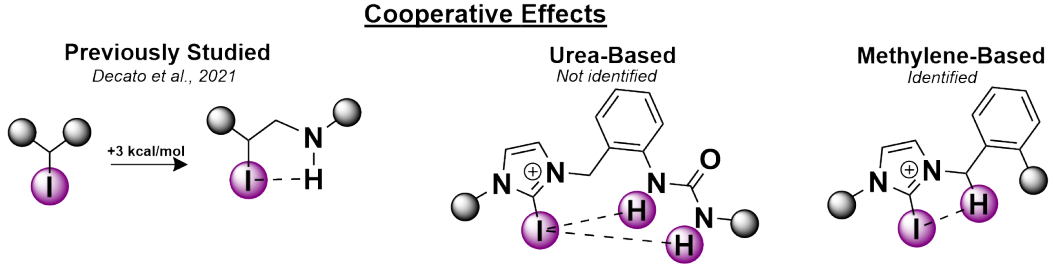

Figure 5.5: Previously identified amine-based cooperative effect (left). Experimentally proposed HBeXB urea- (middle) and theoretically proposed methylene-based (right) cooperative effects in CAT1.

The interaction was not found in either the major or minor conformers of 1·BArF$_4^-$ or 1·PF6$^-$. Instead, an alternative intramolecular HB between the iodoazolium unit and a methylene H atom was identified (Figure 5.5), adopting a parallel geometry analogous to cooperative amide-based systems.[310] QTAIM and NBO descriptors, related to the intramolecular HB between the iodoazolium unit and a methylene spacer, are outlined in Table 5.2.

Table 5.2: CT (kcal/mol) and BCPs (a.u.) representative of I (LP) ···· H (BD*) between the iodoazolium unit and the methylene spacer for the major and minor conformers of 1·BArF$_4^-$ or 1·PF6$^-$. V_{max} values (kcal/mol) representative of the XB-donor σ-hole.

System	BCP (a.u.)	CT (kcal/mol)	V_{max} (kcal/mol)
1·**PF**$_6^-$ (major)	0.0120	0.84	91.45
1·**PF**$_6^-$ (minor)	N/A	N/A	107.01
1·**BAr**$^F{}_4^-$ (major)	0.0120	1.03	92.98
1·**BAr**$^F{}_4^-$ (minor)	0.0122	1.48	112.41

To assess the electrostatic impact of the intramolecular HB between the iodoazolium unit and the methylene spacer, MEP analyses were performed on the major and minor conformers of 1·PF$_6^-$ and 1·BArF4$^-$. As shown in Table 5.2, this interaction does not significantly affect the σ-hole Vmax. As exemplified in the 1·PF$_6^-$ system, the intramolecular HB is present in the major conformer (CT = 0.84 kcal/mol) but absent in the minor conformer, yet the corresponding σ-hole Vmax values (91.45 and 107.01 kcal/mol respectively) show no enhancement attributable to this intramolecular interaction.

5.3.2 Ritter-Type Solvolysis

5.3.2.1 Electronic Properties

MEP calculations were performed for the major and minor conformers of 1·PF_6^- and 1·BArF4$^-$ (Figure 5.6), to evaluate how counterion-induced conformational changes affect the *V*max values of the XB donor, the urea HB donor, and subsequently the substrate-binding site. Relative to the isolated CAT1, V_{max} 94 kcal/mol, the major and minor conformers of 1·PF_6^- and 1·BArF4$^-$ complexes exhibit reduced σ-hole magnitude at the XB-donor site, reflecting the introduction of NCIs between CAT1 and the anion that modify both its electronic and steric environment.

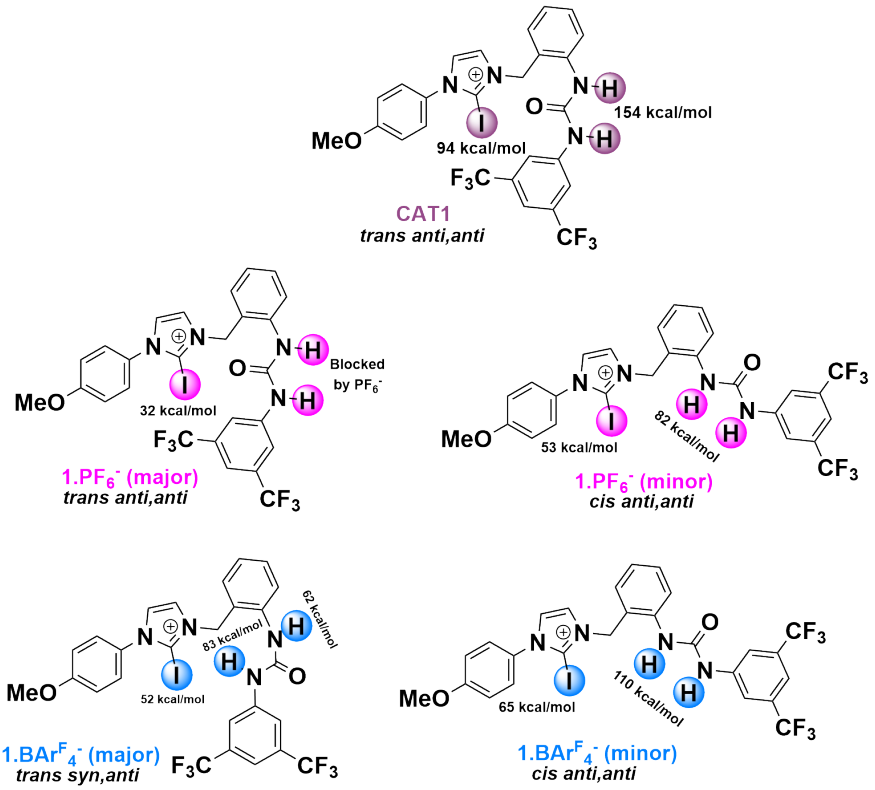

Figure 5.6: MEP on the 0.001 a.u. electron density isosurface, *maxima* (V_{max}) values of the MEP in kcal/mol representative of imidazolium XB donor, and the urea HB donors for 1·$BArF_4^-$ and 1·PF_6^-.

In 1·PF_6^- (major), the anion forms a compact HB interaction with the urea moeity on CAT1, limiting the substrate binding accessibility of the HB-donor active site on the urea. 1·PF_6^- (major) had a lower σ-hole magnitude than 1·PF_6^- (minor), 32 kcal/mol and 53 kcal/mol respectively. As discussed in Section 5.3.1 Conformational Analysis,

the minor conformer has weaker interactions with the anion relative to the major conformer (Table 5.1), thereby the electronic and steric effects imposed by the anion are reduced in the 1·PF_6^- (minor) complex.

In 1·$BArF_4^-$ (major), strong π-π interactions and a HB between CAT1 and anion result in a crowded environment around the iodoazolium motif, as discussed in Section 5.3.1 Conformational Analysis, resulting in a reduced σ-hole magnitude, V_{max} 51.80 kcal/mol. 1·$BArF_4^-$ (minor), characterised by fewer and relatively weaker CAT1-anion interactions, results in a more accesible binding pocket and larger σ-hole, V_{max} 65.03 kcal/mol. While counterion interactions can stabilise certain catalyst conformers, they may simultaneously diminish catalytic performance by reducing the accessibility and strength of key substrate interaction sites.

5.3.2.2 Reactivity Studies

The highest Boltzmann populated complexes, 1·PF_6^- (major) and 1·$BArF_4^-$ (major), were further examined in the context of the CAT1-catalysed Ritter-type solvolysis of benzhydryl bromide (Figure 5.7 and Figure 5.8).

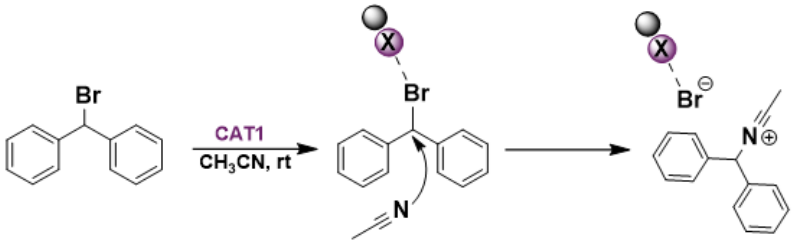

Figure 5.7: Concerted reaction pathway for the CAT1-catalysed Ritter-Type solvolysis with benzhydryl bromide.

To assess the influence of counterions on catalytic performance, three computational protocols were employed: (i) conformational searching and reactivity analysis without a counterion; (ii) conformational searching in the presence of a counterion, followed by reactivity analysis without it; and (iii) conformational searching and reactivity analysis both conducted in the presence of the counterion.

As shown in Figure 5.9, the PES profiles of isolated CAT1 and the PF_6^--complexed

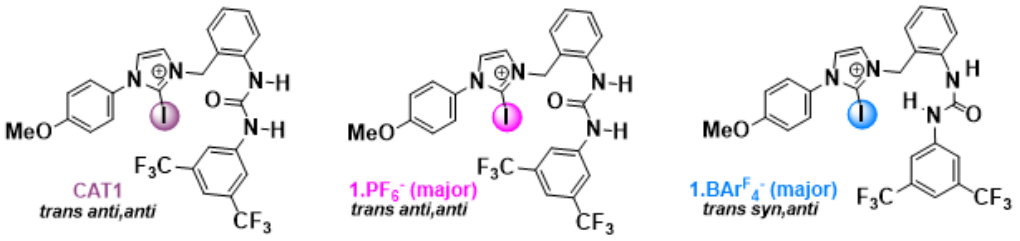

Figure 5.8: Highest Boltzmann populated conformers for isolated CAT1 (left), $1{\cdot}PF_6^-$ (middle) and $1{\cdot}BArF_4^-$ (right).

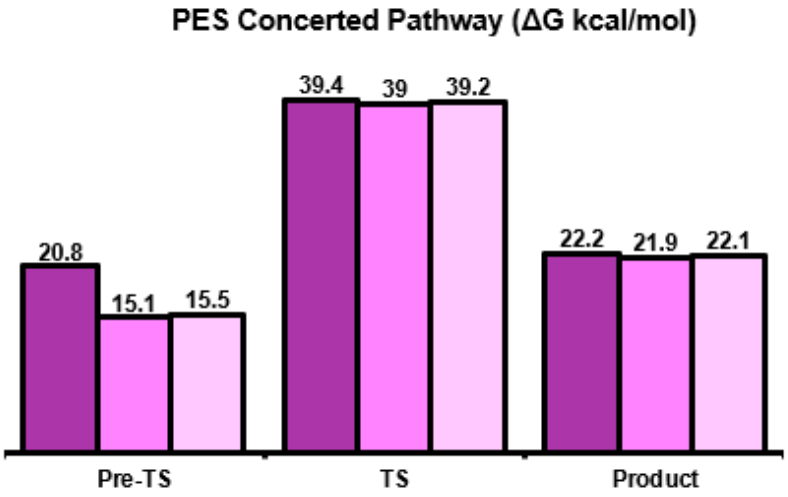

Figure 5.9: PES (ΔG kcal/mol) for the concerted pathway of an XB-based catalysed Ritter-Type Solvolysis using isolated CAT1 (purple) and $1{\cdot}PF_6^-$ (pink). Reactivity study without (dark pink) and with (light pink) the counterion shown.

species $1{\cdot}PF_6^-$ are closely aligned, consistent with their similar dominant conformations (Figure 5.8).

The $BArF_4^-$ complex displays a destabilised TS, with an increase of 2.3–2.8 kcal/mol relative to isolated CAT1, and a less favourable product by 6.5 kcal/mol (Figure 5.10). This energetic divergence reflects the substantially different conformational preference induced by $BArF_4^-$ complexation (Figure 5.8).

These findings highlight the significant influence of counterions on the conformational landscape of cationic catalysts and demonstrate that their inclusion during conformational analysis is essential for accurately capturing the structural and energetic features of XB-based systems. Comparison of protocols, (ii) conformational searching in the presence of a counterion, followed by reactivity analysis without it;

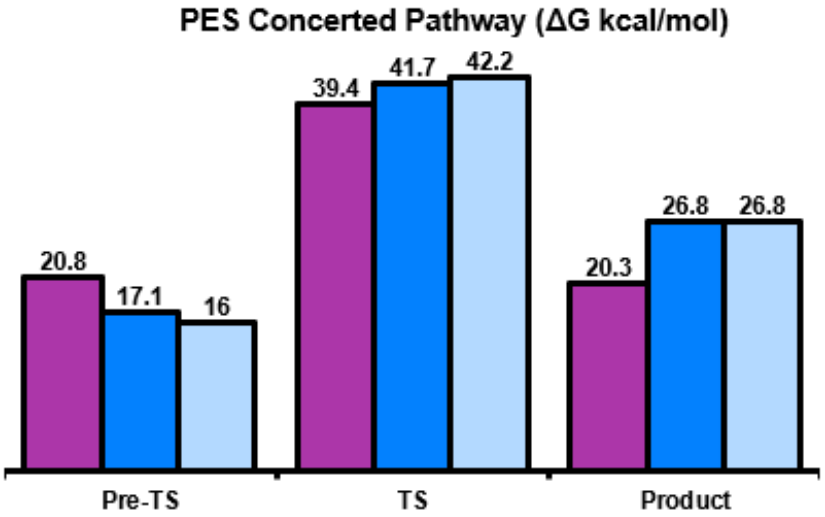

Figure 5.10: PES (ΔG kcal/mol) for the concerted pathway of an XB-based catalysed Ritter-Type Solvolysis using isolated CAT1 (purple) and 1·$BArF_4^-$ (blue). Reactivity study without (dark blue) and with (light blue) the counterion shown.

and (iii) conformational searching and reactivity analysis both conducted in the presence of the counterion, revealed consistent outcomes for both systems considered, 1·PF_6^- and 1·$BArF_4^-$. In each case, the resulting PES profiles differed by less than 1 kcal/mol along the reaction coordinate (Figures 5.9 and 5.10). These results indicate that incorporating the counterion during conformational ensemble generation is sufficient to capture the counterion driven catalyst geometries required for reliable reactivity predictions. Retaining the counterion throughout PES modelling provides only marginal gains in accuracy at substantially higher computational cost.

6 | Conclusion

6.1 Main Findings

The work presented in this thesis investigated XB-based scaffolds as an alternative and complementary approach to traditional HB-based organocatalysts. While initially motivated by conceptual parallels between HB and XB, the results demonstrate that XB-based systems possess a distinct design rationale, characterised by stronger directionality, greater tunability, and access to multiple activation modes. Consequently, XB-based catalysis should be regarded not as a simple analogue of HB catalysis, but as a separate strategy with unique principles, challenges, and opportunities.

The first stage of this research provided a foundational study of monovalent XB-based catalysts in the prototypical Michael addition of indole to *trans*-crotonophenone. Systematic computational analysis showed that σ-hole accessibility, governed by scaffold electronics, steric environment, and donor positioning, is the decisive factor for catalytic efficiency. The results highlighted that not only the strength but also the orientation and spatial arrangement of the XB-donor control substrate engagement. Importantly, flexible and bidentate monovalent scaffolds were found to favour π-type activation pathways over the long-assumed O-type activation, reframing mechanistic expectations for XB catalysis. The I_2-catalysed Michael addition, long debated in the literature, was shown to proceed via a dual interaction that is simultaneously noncovalent and partially covalent at the substrate α-carbon, explaining

iodine's exceptional catalytic performance.

These mechanistic insights were then extended to the ROP of L-lactide. XB-based scaffolds in cooperation with the base played a key role in stabilising intermediates and steering mechanistic pathways. A dispersed, cooperative activation mode, in which the catalyst simultaneously engaged the lactide carbonyl oxygen and the initiator hydroxyl group, emerged as the most favourable. This behaviour mirrors the preferences observed in the Michael addition and suggests that relatively flexible monovalent XB scaffolds are most effective when they stabilise multiple electron-rich regions in a distributed fashion.

Having established a foundation with monovalent systems, the thesis next explored hypervalent XB-based scaffolds. Hypervalency introduces stronger and more pronounced σ-holes, but also rigidity and enforced geometry, which fundamentally alter activation preferences. In contrast to flexible monovalent donors that favour π-type activation, hypervalent iodine(III) scaffolds consistently preferred O-type activation at the carbonyl oxygen. Systematic variation of scaffold electronics and substituent placement showed that catalytic efficiency arises from a balance between σ-hole strength, substituent positioning, and steric environment, rather than from simply maximising interaction strength. Hypervalent XB-donors therefore constitute a distinct design platform, where fine-tuning rigidity and orientation is as important as enhancing Lewis acidity.

The final stage of this thesis addressed a crucial but often overlooked aspect of charged XB-based systems: the roles of counterions and associated intramolecular interactions. Motivated by proposed cooperative HBeXB effects, extensive conformational analyses revealed that direct HBeXB cooperativity was not observed, but that intramolecular hydrogen bonding at the γ-position emerged as a stabilising feature. Although this interaction did not directly enhance σ-hole strength, it can be substituted with stronger HB-donors at this position to modulate catalyst geometry. Even more strikingly, counterions were shown to exert a profound influence. Rather

than acting as passive spectators, they stabilised particular conformers through HB and π–π interactions, narrowing the accessible conformational ensemble and modulating the accessibility of active sites. Reaction pathway calculations for a Ritter-type solvolysis confirmed that these counterion-induced conformational differences significantly affect both transition-state and product energies, demonstrating that explicit counterion inclusion is essential for realistic computational modelling of charged XB-based catalysts.

Together, these studies establish a continuous mechanistic hierarchy across XB-based catalysts, linking electronic structure and scaffold rigidity to activation mode, and culminating in a comprehensive understanding of environmental and cooperative effects.

6.2 Future Work

Building on these findings, future research in this area should focus on three interconnected themes: refining XB design principles, developing asymmetric XB catalysis, and exploiting counterion tuning as a deliberate design element.

The findings of this thesis underscore the unique potential of XB scaffolds as a foundation for organocatalyst design, while revealing the complexity of factors that govern their behaviour, from scaffold electronics and geometry to counterion effects and activation mode preferences. Building on these insights, several promising directions for future research can be identified. Future work may be broadly grouped into three themes: (i) refinement of XB design principles, (ii) development of asymmetric XB catalysis, and (iii) deliberate exploitation of counterions as design elements.

A central contribution of this thesis has been the identification of key design principles that distinguish XB-based catalysis from its HB analogue: the importance of σ-hole accessibility, scaffold rigidity versus flexibility, and the balance between electronic strength and orientational control. Future work should translate these principles into systematic design strategies for next-generation XB-based catalysts.

One particular avenue lies in the rational tuning of σ-hole properties through scaffold modification. This extends past the electronic adjustment of XB-donor strength through substituents, emphasising the importance of strategically placing intramolecular stabilising groups, in appropriate proximity to the XB-donor atom, as demonstrated throughout this thesis.

The mechanistic insights obtained here are particularly relevant for extending XB-based catalysis into enantioselective organocatalysis, a field that remains in its infancy but holds considerable promise. The strong directionality and tunability of XB-donors provide a natural platform for chiral induction, as XB can impose strict angular preferences while allowing fine electronic adjustment. The coexistence of O-type, π-type, and cooperative activation modes observed in this thesis suggests that activation mode in XB catalysis is inherently context-dependent, dictated by scaffold architecture, donor valency, substrate electronics, and steric environment. In chiral systems, XB catalyst design must therefore go beyond maximising σ-hole depth to control both the strength and geometry of multipoint interactions. The contrast between π-type activation in flexible monovalent systems and O-type activation in rigid hypervalent donors illustrates how scaffold architecture can be tuned to select the dominant activation pathway, offering a powerful tool for stereocontrol. Embedding the identified dual, distributed binding modes within a chiral environment represents a particularly promising strategy for achieving high enantioselectivity.

The identification of non-coordinating counterions as active participants in shaping catalyst geometry and reactivity marks another important avenue for future work. Computational studies should routinely include explicit counterions to capture their impact on conformational ensembles, σ-hole accessibility, and transition-state energetics, thereby improving alignment between theory and experiment. Experimentally, systematic variation of counterion size, coordinating ability, and geometry could be used to stabilise active conformations, modulate σ-hole depth, or restrict conformational freedom. In particular, pairing XB scaffolds with chiral anions offers

an underexplored strategy for exerting additional stereocontrol via counterion-tuned catalysis.

Bibliography

[1] S.J. Green. *Industrial Catalysis*. E. Benn limited, 1928. URL https://books.google.ie/books?id=F28KAQAAIAAJ.

[2] Jerzy Haber, Jochen H. Block, and Bernard Delmon. *Methods and Procedures for Catalyst Characterization*. Wiley, February 2008. ISBN 9783527610044. doi: 10.1002/9783527610044.hetcat0066. URL http://dx.doi.org/10.1002/9783527610044.hetcat0066.

[3] Gerhard Ertl. Wilhelm ostwald: Founder of physical chemistry and nobel laureate 1909. *Angewandte Chemie International Edition*, 48(36):6600–6606, August 2009. ISSN 1521-3773. doi: 10.1002/anie.200901193. URL http://dx.doi.org/10.1002/anie.200901193.

[4] in J. R. Anderson G. M. Schwab and M. Boudart (Eds.). *Catalysis*. Springer Berlin Heidelberg, 1984. ISBN 9783642932472. doi: 10.1007/978-3-642-93247-2. URL http://dx.doi.org/10.1007/978-3-642-93247-2.

[5] W. Ruske. A. history of chemistry. von j. r. partington. band iv. macmillan amp; co. ltd., london; st. martin's press, new york 1964. 1. aufl., xxxi, 1007 s., 91 abb., geb. £ 10.10.0. *Angewandte Chemie*, 77(7):360–360, April 1965. ISSN 1521-3757. doi: 10.1002/ange.19650770743. URL http://dx.doi.org/10.1002/ange.19650770743.

[6] in J.R. Anderson S. A. Topham and M. Boudart (Eds.). *Catalysis*. Springer

Berlin Heidelberg, 1996. ISBN 9783642610059. doi: 10.1007/978-3-642-61005-9. URL http://dx.doi.org/10.1007/978-3-642-61005-9.

[7] F. Haber and G. van Oordt. Über die bildung von ammoniak den elementen. *Zeitschrift für anorganische Chemie*, 44(1):341–378, January 1905. ISSN 0863-1778. doi: 10.1002/zaac.19050440122. URL http://dx.doi.org/10.1002/zaac.19050440122.

[8] Susan A. Topham. *The History of the Catalytic Synthesis of Ammonia*, page 1–50. Springer Berlin Heidelberg, 1985. ISBN 9783642932816. doi: 10.1007/978-3-642-93281-6_1. URL http://dx.doi.org/10.1007/978-3-642-93281-6_1.

[9] O. Lemmermann. Alwin mittasch: Geschichte der ammoniaksynthese. verlag chemie, berlin-weinheim, 1951. 196 seiten mit 12 bildtafeln und 4 abbildungen. ganzleinen dm 13, 20. *Zeitschrift für Pflanzenernährung, Düngung, Bodenkunde*, 55(3):258–258, 1951. ISSN 1522-2624. doi: 10.1002/jpln.19510550307. URL http://dx.doi.org/10.1002/jpln.19510550307.

[10] Alwin Mittasch and W. Frankenburg. *Early Studies of Multicomponent Catalysts*, page 81–104. Elsevier, 1950. ISBN 9780120078028. doi: 10.1016/s0360-0564(08)60375-2. URL http://dx.doi.org/10.1016/S0360-0564(08)60375-2.

[11] F. Asinger. *Methanol: The Basic Chemical and Energy Feedstock of the Future: Asinger's Vision Today*. Springer Berlin Heidelberg, 2014. ISBN 9783642397097. doi: 10.1007/978-3-642-39709-7. URL http://dx.doi.org/10.1007/978-3-642-39709-7.

[12] J K Paul. *Methanol technology and application in motor fuels*. Noyes Data Corp.,Park Ridge, NJ, 12 1977. URL https://www.osti.gov/biblio/6867728.

[13] Gerhard Ertl, H Knozinger, and J Weitkamp, editors. *Handbook of heterogeneous catalysis*. Wiley-VCH Verlag, Weinheim, Germany, July 1997.

[14] H.H. Storch. *The Fischer-Tropsch and Related Processes for Synthesis of Hydrocarbons by Hydrogenation of Carbon Monoxide*, page 115–156. Elsevier, 1948. doi: 10.1016/s0360-0564(08)60674-4. URL http://dx.doi.org/10.1016/S0360-0564(08)60674-4.

[15] Mary Ellen Bowden. *Chemical achievers*. Chemical Heritage Foundation, Philadelphia, PA, April 2005.

[16] Keith J. Laidler. The activated complex in heterogeneous catalysis. *Discussions of the Faraday Society*, 8:47, 1950. ISSN 0366-9033. doi: 10.1039/df9500800047. URL http://dx.doi.org/10.1039/DF9500800047.

[17] K. Ziegler. Consequences and development of an invention. In *Nobel Lectures, Chemistry 1963–1970*, pages 1–17. Elsevier, Amsterdam, Netherlands, 1972.

[18] G. Natta. From the stereospecific polymerization to the asymmetric autocatalytic synthesis of macromolecules. In *Nobel Lectures, Chemistry 1963–1970*, pages 18–39. Elsevier, Amsterdam, Netherlands, 1972.

[19] Jong Rack Sohn, Hae Won Kim, and Jong Taik Kim. Preparation of nio-zro2/so 4 -2 catalyst and its catalytic activity for ethylene dimerization. *Korean Journal of Chemical Engineering*, 4(1):1–7, March 1987. ISSN 1975-7220. doi: 10.1007/bf02698092. URL http://dx.doi.org/10.1007/BF02698092.

[20] T. Pearce and J. Perret. Steam-reforming process for hydrocarbons. Technical report, Imperial Chemical Industries Ltd., 1962.

[21] Geoffrey Wilkinson. Tertiary phosphine complexes of the platinum metals: Principles of their reaction mechanisms and uses in homogeneous catalysis. *Platinum Metals Review*, 12(2):50–53, April 1968. ISSN 0032-1400. doi: 10.1595/003214068x1225053. URL http://dx.doi.org/10.1595/003214068X1225053.

[22] Thomas J. Colacot and Narayan S. Hosmane. Organometallic sandwich compounds in homogeneous catalysis: An overview. *Zeitschrift für anorganische und*

allgemeine Chemie, 631(13–14):2659–2668, October 2005. ISSN 1521-3749. doi: 10.1002/zaac.200500224. URL http://dx.doi.org/10.1002/zaac.200500224.

[23] John N. Armor. A history of industrial catalysis. *Catalysis Today*, 163(1): 3–9, April 2011. ISSN 0920-5861. doi: 10.1016/j.cattod.2009.11.019. URL http://dx.doi.org/10.1016/j.cattod.2009.11.019.

[24] L Rosenthaler. Durch enzyme bewirkte asymmetrische synthesen. *Biochem. Z*, 14:238–253, 1908.

[25] H. B. Kagan. Nonlinear effects in enantioselective organometallic catalysis. *Oil amp; Gas Science and Technology - Revue de l'IFP*, 62(6):731–738, October 2007. ISSN 1294-4475. doi: 10.2516/ogst:2007051. URL http://dx.doi.org/10.2516/ogst:2007051.

[26] William S. Knowles. Asymmetric hydrogenations (nobel lecture) copyright© the nobel foundation 2002. we thank the nobel foundation, stockholm, for permission to print this lecture. *Angewandte Chemie International Edition*, 41 (12):1998, June 2002. ISSN 1521-3773. doi: 10.1002/1521-3773(20020617) 41:12<1998::aid-anie1998>3.0.co;2-8. URL http://dx.doi.org/10.1002/1521-3773(20020617)41:12<1998::AID-ANIE1998>3.0.CO;2-8.

[27] Ryoji Noyori. Asymmetric catalysis: Science and opportunities (nobel lecture) copyright© the nobel foundation 2002. we thank the nobel foundation, stockholm, for permission to print this lecture. *Angewandte Chemie International Edition*, 41(12):2008, June 2002. ISSN 1521-3773. doi: 10.1002/1521-3773(20020617) 41:12<2008::aid-anie2008>3.0.co;2-4. URL http://dx.doi.org/10.1002/1521-3773(20020617)41:12<2008::AID-ANIE2008>3.0.CO;2-4.

[28] K. Barry Sharpless. Searching for new reactivity (nobel lecture) copyright© the nobel foundation 2002. we thank the nobel foundation, stockholm, for permission to print this lecture. adapted with the permission of the editors from "coelacanths and catalysis": K. b. sharpless, tetrahedron 1994, 50,

4235. *Angewandte Chemie International Edition*, 41(12):2024, June 2002. ISSN 1521-3773. doi: 10.1002/1521-3773(20020617)41:12<2024::aid-anie2024>3.0.co;2-o. URL http://dx.doi.org/10.1002/1521-3773(20020617)41:12<2024::AID-ANIE2024>3.0.CO;2-O.

[29] L. Horner, H. Siegel, and H. Büthe. Asymmetric catalytic hydrogenation with an optically active phosphinerhodium complex in homogeneous solution. *Angewandte Chemie International Edition in English*, 7(12):942–942, December 1968. ISSN 0570-0833. doi: 10.1002/anie.196809422. URL http://dx.doi.org/10.1002/anie.196809422.

[30] W. S. Knowles and M. J. Sabacky. Catalytic asymmetric hydrogenation employing a soluble, optically active, rhodium complex. *Chemical Communications (London)*, (22):1445, 1968. ISSN 0009-241X. doi: 10.1039/c19680001445. URL http://dx.doi.org/10.1039/C19680001445.

[31] T. P. Dang and H. B. Kagan. The asymmetric synthesis of hydratropic acid and amino-acids by homogeneous catalytic hydrogenation. *Journal of the Chemical Society D: Chemical Communications*, (10):481, 1971. ISSN 0577-6171. doi: 10.1039/c29710000481. URL http://dx.doi.org/10.1039/C29710000481.

[32] Willy. Dumont, Jean C. Poulin, . Dang Tuan Phat, and Henri B. Kagan. Asymmetric catalytic reduction with transition metal complexes. ii. asymmetric catalysis by a supported chiral rhodium complex. *Journal of the American Chemical Society*, 95(25):8295–8299, December 1973. ISSN 1520-5126. doi: 10.1021/ja00806a015. URL http://dx.doi.org/10.1021/JA00806A015.

[33] B. D. Vineyard, W. S. Knowles, M. J. Sabacky, G. L. Bachman, and D. J. Weinkauff. Asymmetric hydrogenation. rhodium chiral bisphosphine catalyst. *Journal of the American Chemical Society*, 99(18):5946–5952, August 1977. ISSN 1520-5126. doi: 10.1021/ja00460a018. URL http://dx.doi.org/10.1021/ja00460a018.

[34] Ryoji. Noyori, Masako. Ohta, Yi. Hsiao, Masato. Kitamura, Tetsuo. Ohta, and Hidemasa. Takaya. Asymmetric synthesis of isoquinoline alkaloids by homogeneous catalysis. *Journal of the American Chemical Society*, 108(22): 7117–7119, October 1986. ISSN 1520-5126. doi: 10.1021/ja00282a054. URL http://dx.doi.org/10.1021/ja00282a054.

[35] Ryoji Noyori, Takeshi Ohkuma, Masato Kitamura, Hidemasa Takaya, Noboru Sayo, Hidenori Kumobayashi, and Susumu Akutagawa. Asymmetric hydrogenation of .beta.-keto carboxylic esters. a practical, purely chemical access to .beta.-hydroxy esters in high enantiomeric purity. *Journal of the American Chemical Society*, 109(19):5856–5858, September 1987. ISSN 1520-5126. doi: 10.1021/ja00253a051. URL http://dx.doi.org/10.1021/ja00253a051.

[36] R. Noyori, T. Ikeda, T. Ohkuma, M. Widhalm, M. Kitamura, H. Takaya, S. Akutagawa, N. Sayo, T. Saito, T. Taketomi, and H. Kumobayashi. Stereoselective hydrogenation via dynamic kinetic resolution. *Journal of the American Chemical Society*, 111(25):9134–9135, December 1989. ISSN 1520-5126. doi: 10.1021/ja00207a038. URL http://dx.doi.org/10.1021/ja00207a038.

[37] Rudolf Schmid. Homogeneous catalysis with metal complexes in a pharmaceuticals' and vitamins' company: Why, what for, and where to go? *CHIMIA*, 50(3):110, March 1996. ISSN 0009-4293. doi: 10.2533/chimia.1996.110. URL http://dx.doi.org/10.2533/chimia.1996.110.

[38] *Environmental Health Perspectives*, 10:261–268, April 1975. ISSN 1552-9924. doi: 10.1289/ehp.10-1475052. URL http://dx.doi.org/10.1289/ehp.10-1475052.

[39] J ANDERSON. Mechanism of some conversions over zsm-5 catalyst. *Journal of Catalysis*, 61(2):477–484, February 1980. ISSN 0021-9517. doi: 10.1016/0021-9517(80)90394-2. URL http://dx.doi.org/10.1016/0021-9517(80)90394-2.

[40] G. W. Spitznagel, K. Hüttenhofer, and J. K. Beer. *NO Abatement by Selective*

Catalytic Reduction, page 172–189. American Chemical Society, February 1994. ISBN 9780841214248. doi: 10.1021/bk-1994-0552.ch014. URL http://dx.doi.org/10.1021/bk-1994-0552.ch014.

[41] David W. C. MacMillan. The advent and development of organocatalysis. *Nature*, 455(7211):304–308, September 2008. ISSN 1476-4687. doi: 10.1038/nature07367. URL http://dx.doi.org/10.1038/nature07367.

[42] Mike Lancaster. *Green chemistry: an introductory text*. Royal society of chemistry, 2025.

[43] Paul T Anastas and John C Warner. *Green chemistry: theory and practice*. Oxford university press, 2000.

[44] James H Clark and Christopher N Rhodes. *Clean synthesis using porous inorganic solid catalysts and supported reagents*, volume 4. Royal Society of Chemistry, 2000.

[45] James H Clark. Catalysis for green chemistry. *Pure and Applied Chemistry*, 73 (1):103–111, 2001.

[46] Paul Southard Fiske. *Durch katalysatoren bewirkte asymmetrische synthese*. PhD thesis, ETH Zurich, 1911.

[47] V Prelog and M Wilhelm. Untersuchungen über asymmetrische synthesen vi. der reaktionsmechanismus und der sterische verlauf der asymmetrischen cyanhydrin-synthese. *Helvetica Chimica Acta*, 37(6):1634–1660, 1954.

[48] Horst Pracejus. Organische katalysatoren, lxi. asymmetrische synthesen mit ketenen, i. alkaloid-katalysierte asymmetrische synthesen von α-phenyl-propionsäureestern. *Justus Liebigs Annalen der Chemie*, 634(1):9–22, 1960.

[49] John C Sheehan and DH Hunneman. Homogeneous asymmetric catalysis. *Journal of the American Chemical Society*, 88(15):3666–3667, 1966.

[50] John C Sheehan and Takeshi Hara. Asymmetric thiazolium salt catalysis of the benzoin condensation. *The Journal of Organic Chemistry*, 39(9):1196–1199, 1974.

[51] Ulrich Eder, Gerhard Sauer, and Rudolf Wiechert. New type of asymmetric cyclization to optically active steroid cd partial structures. *Angewandte Chemie International Edition in English*, 10(7):496–497, 1971.

[52] Zoltan G Hajos and David R Parrish. Asymmetric synthesis of bicyclic intermediates of natural product chemistry. *The Journal of organic chemistry*, 39(12): 1615–1621, 1974.

[53] R Helder, JC Hummelen, RWPM Laane, JS Wiering, and Hans Wynberg. Catalytic asymmetric induction in oxidation reactions-synthesis of optically-active epoxides. *Tetrahedron Letters*, 17(21):1831–1834, 1976.

[54] Henk Hiemstra and Hans Wynberg. Addition of aromatic thiols to conjugated cycloalkenones, catalyzed by chiral. beta.-hydroxy amines. a mechanistic study of homogeneous catalytic asymmetric synthesis. *Journal of the American Chemical Society*, 103(2):417–430, 1981.

[55] P Davis, EJJ GRABOWSKI, and UH DOLLING. Catalytic asymmetric alkylations via phase-transfer catalysis. *J. Am. Chem. Soc*, 106:446–447, 1984.

[56] Matthew S Sigman and Eric N Jacobsen. Schiff base catalysts for the asymmetric strecker reaction identified and optimized from parallel synthetic libraries. *Journal of the American Chemical Society*, 120(19):4901–4902, 1998.

[57] Scott J Miller, Gregory T Copeland, Nikolaos Papaioannou, Thomas E Horstmann, and Elizabeth M Ruel. Kinetic resolution of alcohols catalyzed by tripeptides containing the n-alkylimidazole substructure. *Journal of the American Chemical Society*, 120(7):1629–1630, 1998.

[58] J Craig Ruble, Hallie A Latham, and Gregory C Fu. Effective kinetic resolution of secondary alcohols with a planar- chiral analogue of 4-(dimethylamino)

pyridine. use of the fe (c5ph5) group in asymmetric catalysis. *Journal of the American Chemical Society*, 119(6):1492–1493, 1997.

[59] Scott E Denmark, Stephen BD Winter, Xiping Su, and Ken-Tsung Wong. Chemistry of trichlorosilyl enolates. 1. new reagents for catalytic, asymmetric aldol additions. *Journal of the American Chemical Society*, 118(31):7404–7405, 1996.

[60] Takashi Ooi, Minoru Kameda, and Keiji Maruoka. Molecular design of a c 2-symmetric chiral phase-transfer catalyst for practical asymmetric synthesis of α-amino acids. *Journal of the American Chemical Society*, 121(27):6519–6520, 1999.

[61] Benjamin List, Richard A Lerner, and Carlos F Barbas. Proline-catalyzed direct asymmetric aldol reactions. *Journal of the American Chemical Society*, 122(10): 2395–2396, 2000.

[62] Kateri A Ahrendt, Christopher J Borths, and David WC MacMillan. New strategies for organic catalysis: the first highly enantioselective organocatalytic diels- alder reaction. *Journal of the American Chemical Society*, 122(17):4243–4244, 2000.

[63] Benjamin List. Direct catalytic asymmetric α-amination of aldehydes. *J. Am. Chem. Soc.*, 124(20):5656–5657, May 2002.

[64] Albrecht Berkessel and Harald Gröger. *Asymmetric Organocatalysis: From Biomimetic Concepts to Applications in Asymmetric Synthesis*. Wiley, January 2005. ISBN 9783527604678. doi: 10.1002/3527604677. URL `http://dx.doi.org/10.1002/3527604677`.

[65] Benjamin List. The direct catalytic asymmetric three-component mannich reaction. *J. Am. Chem. Soc.*, 122(38):9336–9337, September 2000.

[66] Jung Woon Yang, Carley Chandler, Michael Stadler, Daniela Kampen, and

Benjamin List. Proline-catalysed mannich reactions of acetaldehyde. *Nature*, 452(7186):453–455, March 2008.

[67] Carley Chandler, Patrizia Galzerano, Anna Michrowska, and Benjamin List. The proline-catalyzed double mannich reaction of acetaldehyde with N-Boc imines. *Angew. Chem. Int. Ed Engl.*, 48(11):1978–1980, 2009.

[68] Jung Woon Yang, Maria T Hechavarria Fonseca, Nicola Vignola, and Benjamin List. Metal-free, organocatalytic asymmetric transfer hydrogenation of alpha,beta-unsaturated aldehydes. *Angew. Chem. Int. Ed Engl.*, 44(1):108–110, December 2004.

[69] Benjamin List. Enamine catalysis is a powerful strategy for the catalytic generation and use of carbanion equivalents. *Acc. Chem. Res.*, 37(8):548–557, August 2004.

[70] Wendy S Jen, John J M Wiener, and David W C MacMillan. New strategies for organic catalysis: The first enantioselective organocatalytic 1,3-dipolar cycloaddition. *J. Am. Chem. Soc.*, 122(40):9874–9875, October 2000.

[71] N A Paras and D W MacMillan. New strategies in organic catalysis: the first enantioselective organocatalytic Friedel-Crafts alkylation. *J. Am. Chem. Soc.*, 123(18):4370–4371, May 2001.

[72] Nick A Paras and David W C MacMillan. The enantioselective organocatalytic 1,4-addition of electron-rich benzenes to α,β-unsaturated aldehydes. *J. Am. Chem. Soc.*, 124(27):7894–7895, July 2002.

[73] Sean P Brown, Nicole C Goodwin, and David W C MacMillan. The first enantioselective organocatalytic Mukaiyama-Michael reaction: a direct method for the synthesis of enantioenriched gamma-butenolide architecture. *J. Am. Chem. Soc.*, 125(5):1192–1194, February 2003.

[74] Gérald Lelais and {David W.C.} MacMillan. Modern strategies in organic catalysis: The advent and development of iminium activation. *Aldrichimica Acta*, 39(3):79–87, 2006. ISSN 0002-5100.

[75] Mauro Marigo, Tobias C Wabnitz, Doris Fielenbach, and Karl Anker Jørgensen. Enantioselective organocatalyzed alpha sulfenylation of aldehydes. *Angew. Chem. Int. Ed Engl.*, 44(5):794–797, January 2005.

[76] Yujiro Hayashi, Hiroaki Gotoh, Takaaki Hayashi, and Mitsuru Shoji. Diphenylprolinol silyl ethers as efficient organocatalysts for the asymmetric michael reaction of aldehydes and nitroalkenes. *Angew. Chem. Int. Ed Engl.*, 44(27): 4212–4215, July 2005.

[77] Mauro Marigo, Johan Franzén, Thomas B Poulsen, Wei Zhuang, and Karl Anker Jørgensen. Asymmetric organocatalytic epoxidation of alpha,beta-unsaturated aldehydes with hydrogen peroxide. *J. Am. Chem. Soc.*, 127(19): 6964–6965, May 2005.

[78] M P Almeida, F de Melo, M Hor-Meyll, A Salles, S P Walborn, P H Souto Ribeiro, and L Davidovich. Environment-induced sudden death of entanglement. *Science*, 316(5824):579–582, April 2007.

[79] Jay C Conrad, Jongrock Kong, Brian N Laforteza, and David W C MacMillan. Enantioselective alpha-arylation of aldehydes via organo-SOMO catalysis. an ortho-selective arylation reaction based on an open-shell pathway. *J. Am. Chem. Soc.*, 131(33):11640–11641, August 2009.

[80] David A Nicewicz and David W C MacMillan. Merging photoredox catalysis with organocatalysis: the direct asymmetric alkylation of aldehydes. *Science*, 322(5898):77–80, October 2008.

[81] Stefan P Schmid, Leon Schlosser, Frank Glorius, and Kjell Jorner. Catalysing (organo-)catalysis: Trends in the application of machine learning to enantioselective organocatalysis. *Beilstein Journal of Organic Chemistry*, 20:2280–2304,

September 2024. ISSN 1860-5397. doi: 10.3762/bjoc.20.196. URL http://dx.doi.org/10.3762/bjoc.20.196.

[82] Istvan Hargittai. The 2021 chemistry nobel laureates and asymmetric organocatalysis. *Structural Chemistry*, 33(1):303–305, December 2021. ISSN 1572-9001. doi: 10.1007/s11224-021-01857-0. URL http://dx.doi.org/10.1007/s11224-021-01857-0.

[83] Revannath L. Sutar and Stefan M. Huber. Catalysis of organic reactions through halogen bonding. *ACS Catalysis*, 9(10):9622–9639, September 2019. ISSN 2155-5435. doi: 10.1021/acscatal.9b02894. URL http://dx.doi.org/10.1021/acscatal.9b02894.

[84] Gautam R. Desiraju, P. Shing Ho, Lars Kloo, Anthony C. Legon, Roberto Marquardt, Pierangelo Metrangolo, Peter Politzer, Giuseppe Resnati, and Kari Rissanen. Definition of the halogen bond (iupac recommendations 2013). *Pure and Applied Chemistry*, 85(8):1711–1713, July 2013. ISSN 0033-4545. doi: 10.1351/pac-rec-12-05-10. URL http://dx.doi.org/10.1351/PAC-REC-12-05-10.

[85] Paola Peluso and Victor Mamane. Stereoselective processes based on -hole interactions. *Molecules*, 27(14):4625, July 2022. ISSN 1420-3049. doi: 10.3390/molecules27144625. URL http://dx.doi.org/10.3390/molecules27144625.

[86] John O. Edwards and Ralph G. Pearson. The factors determining nucleophilic reactivities. *Journal of the American Chemical Society*, 84(1):16–24, January 1962. doi: 10.1021/ja00860a005. URL https://doi.org/10.1021/ja00860a005.

[87] Wanutcha Lorpaiboon and Pakorn Bovonsombat. Halogen bond-induced electrophilic aromatic halogenations. *Organic & Biomolecular Chemistry*, 19(35):7518–7534, 2021. doi: 10.1039/d1ob00936b. URL https://doi.org/10.1039/d1ob00936b.

[88] Thomas M. Beale, Michael G. Chudzinski, Mohammed G. Sarwar, and Mark S. Taylor. Halogen bonding in solution: thermodynamics and applications. *Chem.*

Soc. Rev., 42(4):1667–1680, 2013. doi: 10.1039/c2cs35213c. URL https://doi.org/10.1039/c2cs35213c.

[89] Gabriella Cavallo, Pierangelo Metrangolo, Roberto Milani, Tullio Pilati, Arri Priimagi, Giuseppe Resnati, and Giancarlo Terraneo. The halogen bond. *Chemical Reviews*, 116(4):2478–2601, January 2016. doi: 10.1021/acs.chemrev.5b00484. URL https://doi.org/10.1021/acs.chemrev.5b00484.

[90] Pierangelo Metrangolo, Tullio Pilati, and Giuseppe Resnati. Halogen bonding and other noncovalent interactions involving halogens: a terminology issue. *CrystEngComm*, 8(12):946, 2006. doi: 10.1039/b610454a. URL https://doi.org/10.1039/b610454a.

[91] Paulo J. Costa, Rafael Nunes, and Diogo Vila-Viçosa. Halogen bonding in halocarbon-protein complexes and computational tools for rational drug design. *Expert Opinion on Drug Discovery*, 14(8):805–820, May 2019. doi: 10.1080/17460441.2019.1619692. URL https://doi.org/10.1080/17460441.2019.1619692.

[92] Ángel M. Montaña. The and holes. the halogen and tetrel bondings: Their nature, importance and chemical, biological and medicinal implications. *ChemistrySelect*, 2(28):9094–9112, September 2017. doi: 10.1002/slct.201701676. URL https://doi.org/10.1002/slct.201701676.

[93] Tore Brinck, Jane S. Murray, and Peter Politzer. Surface electrostatic potentials of halogenated methanes as indicators of directional intermolecular interactions. *International Journal of Quantum Chemistry*, 44(S19):57–64, March 1992. ISSN 1097-461X. doi: 10.1002/qua.560440709. URL http://dx.doi.org/10.1002/qua.560440709.

[94] Peter Politzer, Jane S. Murray, and Timothy Clark. Halogen bonding and other -hole interactions: a perspective. *Physical Chemistry Chemical Physics*, 15

(27):11178, 2013. doi: 10.1039/c3cp00054k. URL https://doi.org/10.1039/c3cp00054k.

[95] Florian Kniep, Stefan H. Jungbauer, Qi Zhang, Sebastian M. Walter, Severin Schindler, Ingo Schnapperelle, Eberhardt Herdtweck, and Stefan M. Huber. Organocatalysis by neutral multidentate halogen-bond donors. *Angewandte Chemie International Edition*, 52(27):7028–7032, 2013. ISSN 1433-7851. doi: 10.1002/anie.201301351.

[96] P Pelletier. Mémoire sur un nouvel alcali végétal (la strychnine) trouvé dans la fève de saint-ignace, la noix vomique, etc. *Ann. Chim. Phys.*, 10:142–177, 1819.

[97] Tore Brinck, Jane S. Murray, and Peter Politzer. Molecular surface electrostatic potentials and local ionization energies of group v–vii hydrides and their anions: Relationships for aqueous and gas-phase acidities. *International Journal of Quantum Chemistry*, 48(2):73–88, October 1993. ISSN 1097-461X. doi: 10.1002/qua.560480202. URL http://dx.doi.org/10.1002/qua.560480202.

[98] Jane S. Murray, Kim Paulsen, and Peter Politzer. Molecular surface electrostatic potentials in the analysis of non-hydrogen-bonding noncovalent interactions. *Proceedings / Indian Academy of Sciences*, 106(2):267–275, April 1994. ISSN 0253-4134. doi: 10.1007/bf02840749. URL http://dx.doi.org/10.1007/BF02840749.

[99] Pascal Auffinger, Franklin A. Hays, Eric Westhof, and P. Shing Ho. Halogen bonds in biological molecules. *Proceedings of the National Academy of Sciences*, 101(48):16789–16794, November 2004. ISSN 1091-6490. doi: 10.1073/pnas.0407607101. URL http://dx.doi.org/10.1073/pnas.0407607101.

[100] Firas F. Awwadi, Roger D. Willett, Kirk A. Peterson, and Brendan Twamley. The nature of halogenhalogen synthons: Crystallographic and theoretical studies. *Chemistry – A European Journal*, 12(35):8952–8960, November 2006.

ISSN 1521-3765. doi: 10.1002/chem.200600523. URL http://dx.doi.org/10.1002/chem.200600523.

[101] Jane S. Murray, Pat Lane, and Peter Politzer. Expansion of the -hole concept. *Journal of Molecular Modeling*, 15(6):723–729, December 2008. ISSN 0948-5023. doi: 10.1007/s00894-008-0386-9. URL http://dx.doi.org/10.1007/s00894-008-0386-9.

[102] Michal H. Kolář and Pavel Hobza. Computer modeling of halogen bonds and other -hole interactions. *Chemical Reviews*, 116(9):5155–5187, February 2016. ISSN 1520-6890. doi: 10.1021/acs.chemrev.5b00560. URL http://dx.doi.org/10.1021/acs.chemrev.5b00560.

[103] Naziha Tarannam, Rahul Shukla, and Sebastian Kozuch. Yet another perspective on hole interactions. *Physical Chemistry Chemical Physics*, 23(36):19948–19963, 2021. ISSN 1463-9084. doi: 10.1039/d1cp03533a. URL http://dx.doi.org/10.1039/D1CP03533A.

[104] Jonathan Thirman, Elric Engelage, Stefan M. Huber, and Martin Head-Gordon. Characterizing the interplay of pauli repulsion, electrostatics, dispersion and charge transfer in halogen bonding with energy decomposition analysis. *Physical Chemistry Chemical Physics*, 20(2):905–915, 2018. doi: 10.1039/c7cp06959f. URL https://doi.org/10.1039/c7cp06959f.

[105] B. Mallada, A. Gallardo, M. Lamanec, B. de la Torre, V. Špirko, P. Hobza, and P. Jelinek. Real-space imaging of anisotropic charge of -hole by means of kelvin probe force microscopy. *Science*, 374(6569):863–867, November 2021. doi: 10.1126/science.abk1479. URL https://doi.org/10.1126/science.abk1479.

[106] Lydia C. Gilday, Sean W. Robinson, Timothy A. Barendt, Matthew J. Langton, Benjamin R. Mullaney, and Paul D. Beer. Halogen bonding in supramolecular chemistry. *Chemical Reviews*, 115(15):7118–7195, July 2015. ISSN 1520-6890. doi: 10.1021/cr500674c. URL http://dx.doi.org/10.1021/cr500674c.

[107] Peter Politzer, Jane S. Murray, and Timothy Clark. Halogen bonding: an electrostatically-driven highly directional noncovalent interaction. *Physical Chemistry Chemical Physics*, 12(28):7748, 2010. doi: 10.1039/c004189k. URL https://doi.org/10.1039/c004189k.

[108] David Bulfield and Stefan M. Huber. Halogen bonding in organic synthesis and organocatalysis. *Chemistry – A European Journal*, 22(41):14434–14450, 2016. doi: 10.1002/chem.201601844.

[109] Mercedes Zurro, Sören Asmus, Julia Bamberger, Stephan Beckendorf, and Olga GarcíaMancheño. Chiral triazoles in anion-binding catalysis: New entry to enantioselective reissert-type reactions. *Chemistry – A European Journal*, 22 (11):3785–3793, January 2016. ISSN 1521-3765. doi: 10.1002/chem.201504094. URL http://dx.doi.org/10.1002/chem.201504094.

[110] Andreas Vargas Jentzsch, Daniel Emery, Jiri Mareda, Susanta K. Nayak, Pierangelo Metrangolo, Giuseppe Resnati, Naomi Sakai, and Stefan Matile. Transmembrane anion transport mediated by halogen-bond donors. *Nature Communications*, 3(1), June 2012. ISSN 2041-1723. doi: 10.1038/ncomms1902. URL http://dx.doi.org/10.1038/ncomms1902.

[111] Manuel Mahlau and Benjamin List. Asymmetric counteranion-directed catalysis: Concept, definition, and applications. *Angewandte Chemie International Edition*, 52(2):518–533, November 2012. ISSN 1521-3773. doi: 10.1002/anie.201205343. URL http://dx.doi.org/10.1002/anie.201205343.

[112] Julian Wolf, Meghana Poliyodath Mohanan, Revannath Sutar, Elric Engelage, and Stefan M. Huber. Highly enantioselective organocatalysis with bidentate halogen bond donors. *ChemRxiv*, July 2024. doi: 10.26434/chemrxiv-2024-2c5j2. URL http://dx.doi.org/10.26434/chemrxiv-2024-2c5j2.

[113] Lucas de Azevedo Santos, Teodorico C. Ramalho, Trevor A. Hamlin, and F. Matthias Bickelhaupt. Intermolecular covalent interactions: Nature and

directionality. *Chemistry – A European Journal*, 29(14):e202203791, January 2023. doi: 10.1002/chem.202203791. URL https://doi.org/10.1002/chem.202203791.

[114] Nika Melnyk, Marianne Rica Garcia, and Cristina Trujillo. Halogen-bond-based organocatalysis unveiled: Computational design and mechanistic insights. *ACS Catalysis*, pages 15505–15515, 2023. ISSN 2155-5435. doi: 10.1021/acscatal.3c04035.

[115] Sebastian M. Walter, Florian Kniep, Eberhardt Herdtweck, and Stefan M. Huber. Halogen-bond-induced activation of a carbon-heteroatom bond. *Angewandte Chemie International Edition*, 50(31):7187–7191, June 2011. doi: 10.1002/anie.201101672. URL https://doi.org/10.1002/anie.201101672.

[116] JasonE. Hein, JonathanC. Tripp, LarissaB. Krasnova, K.Barry Sharpless, and ValeryV. Fokin. Copper(i)-catalyzed cycloaddition of organic azides and 1-iodoalkynes. *Angewandte Chemie International Edition*, 48(43):8018–8021, October 2009. ISSN 1521-3773. doi: 10.1002/anie.200903558. URL http://dx.doi.org/10.1002/anie.200903558.

[117] Nathan L. Kilah, Matthew D. Wise, Christopher J. Serpell, Amber L. Thompson, Nicholas G. White, Kirsten E. Christensen, and Paul D. Beer. Enhancement of anion recognition exhibited by a halogen-bonding rotaxane host system. *Journal of the American Chemical Society*, 132(34):11893–11895, August 2010. ISSN 1520-5126. doi: 10.1021/ja105263q. URL http://dx.doi.org/10.1021/ja105263q.

[118] Florian Kniep, Stefan H. Jungbauer, Qi Zhang, Sebastian M. Walter, Severin Schindler, Ingo Schnapperelle, Eberhardt Herdtweck, and Stefan M. Huber. Organocatalysis by neutral multidentate halogen-bond donors. *Angewandte Chemie International Edition*, 52(27):7028–7032, 2013. doi: https://doi.org/10.

1002/anie.201301351. URL https://onlinelibrary.wiley.com/doi/abs/10.1002/anie.201301351.

[119] Stefan H. Jungbauer, Sebastian M. Walter, Severin Schindler, Laxmidhar Rout, Florian Kniep, and Stefan M. Huber. Activation of a carbonyl compound by halogen bonding. *Chemical Communications*, 50(47):6281, 2014. ISSN 1364-548X. doi: 10.1039/c4cc03124e. URL http://dx.doi.org/10.1039/C4CC03124E.

[120] Rainer Wilcken, Markus O. Zimmermann, Andreas Lange, Stefan Zahn, and Frank M. Boeckler. Using halogen bonds to address the protein backbone: a systematic evaluation. *Journal of Computer-Aided Molecular Design*, 26(8):935–945, August 2012. ISSN 1573-4951. doi: 10.1007/s10822-012-9592-8. URL http://dx.doi.org/10.1007/s10822-012-9592-8.

[121] Carsten Bolm, Angelika Bruckmann, and Miguel Pena. Organocatalysis through halogen-bond activation. *Synlett*, 2008(6):900–902, April 2008. doi: 10.1055/s-2008-1042935. URL https://doi.org/10.1055/s-2008-1042935.

[122] Wei He, Yi-Cen Ge, and Choon-Hong Tan. Halogen-bonding-induced hydrogen transfer to cn bond with hantzsch ester. *Organic Letters*, 16(12):3244–3247, June 2014. ISSN 1523-7052. doi: 10.1021/ol501259q. URL http://dx.doi.org/10.1021/ol501259q.

[123] Olivier Coulembier, Franck Meyer, and Philippe Dubois. Controlled room temperature rop of l-lactide by icl3: a simple halogen-bonding catalyst. *Polymer Chemistry*, 1(4):434–437, 2010. ISSN 1759-9962. doi: 10.1039/c0py00013b. URL http://dx.doi.org/10.1039/c0py00013b.

[124] Youhei Takeda, Daichi Hisakuni, Chun-Hsuan Lin, and Satoshi Minakata. 2-halogenoimidazolium salt catalyzed aza-diels–alder reaction through halogen-bond formation. *Organic Letters*, 17(2):318–321, December 2014. ISSN 1523-7052. doi: 10.1021/ol503426f. URL http://dx.doi.org/10.1021/ol503426f.

[125] Jan-Philipp Gliese, Stefan H. Jungbauer, and Stefan M. Huber. A halogen-bonding-catalyzed michael addition reaction. *Chemical Communications*, 53(88): 12052–12055, 2017. doi: 10.1039/c7cc07175b. URL https://doi.org/10.1039/c7cc07175b.

[126] Xuelei Liu, Shuang Ma, and Patrick H. Toy. Halogen bond-catalyzed friedel–crafts reactions of aldehydes and ketones using a bidentate halogen bond donor catalyst: Synthesis of symmetrical bis(indolyl)methanes. *Organic Letters*, 21(22):9212–9216, October 2019. ISSN 1523-7052. doi: 10.1021/acs.orglett.9b03578. URL http://dx.doi.org/10.1021/acs.orglett.9b03578.

[127] Huimiao Zhang and Patrick H. Toy. Halogen bond-catalyzed friedelcrafts reactions of furans using a 2, 2'-bipyridine-based catalyst. *Advanced Synthesis amp; Catalysis*, 363(1):215–221, November 2020. ISSN 1615-4169. doi: 10.1002/adsc.202001019. URL http://dx.doi.org/10.1002/adsc.202001019.

[128] Avery J. To and Graham K. Murphy. Iodolium salts as halogen-bond donor catalysts in the nazarov cyclization: the molecular oxygen enigma. *New Journal of Chemistry*, 46(32):15313–15320, 2022. ISSN 1369-9261. doi: 10.1039/d2nj02731c. URL http://dx.doi.org/10.1039/d2nj02731c.

[129] Herbert Mayr, Martin Breugst, and Armin R. Ofial. Farewell to the hsab treatment of ambident reactivity. *Angewandte Chemie International Edition*, 50 (29):6470–6505, July 2011. ISSN 1521-3773. doi: 10.1002/anie.201007100. URL http://dx.doi.org/10.1002/anie.201007100.

[130] Revannath L. Sutar, Elric Engelage, Raphael Stoll, and Stefan M. Huber. Bidentate chiral bis(imidazolium)-based halogen-bond donors: Synthesis and applications in enantioselective recognition and catalysis. *Angewandte Chemie International Edition*, 59(17):6806–6810, March 2020. ISSN 1521-3773. doi: 10.1002/anie.201915931. URL http://dx.doi.org/10.1002/anie.201915931.

[131] Julian Wolf, Meghana Poliyodath Mohanan, Raphaël Robidas, Revannath L.

Sutar, Elric Engelage, Claude Y. Legault, and Stefan M. Huber. Highly enantioselective organocatalysis with bidentate halogen bond donors. *Angewandte Chemie International Edition*, 64(30), June 2025. ISSN 1521-3773. doi: 10.1002/anie.202506476. URL http://dx.doi.org/10.1002/anie.202506476.

[132] Florian Ostler, Dariusz G. Piekarski, Tobias Danelzik, Mark S. Taylor, and Olga García Mancheño. Neutral chiral tetrakis-iodo-triazole halogen-bond donor for chiral recognition and enantioselective catalysis. *Chemistry – A European Journal*, 27(7):2315–2320, January 2021. ISSN 1521-3765. doi: 10.1002/chem.202005016. URL http://dx.doi.org/10.1002/chem.202005016.

[133] Alica C. Keuper, Kevin Fengler, Florian Ostler, Tobias Danelzik, Dariusz G. Piekarski, and Olga García Mancheño. Fine-tuning substrate–catalyst halogen–halogen interactions for boosting enantioselectivity in halogen-bonding catalysis. *Angewandte Chemie International Edition*, page e202304781, May 2023. doi: 10.1002/anie.202304781. URL https://doi.org/10.1002/anie.202304781.

[134] Yasushi Yoshida, Tappei Fujimura, Takashi Mino, and Masami Sakamoto. Chiral binaphthyl-based iodonium salt (hypervalent iodine(iii)) as hydrogen- and halogen-bonding bifunctional catalyst: Insight into abnormal counteranion effect and asymmetric synthesis of n,s-acetals. *Advanced Synthesis & Catalysis*, 364(6):1091–1098, 2022. doi: 10.1002/adsc.202101380.

[135] Mattis Damrath, Tarek Scheele, Daniel Duvinage, Tim Neudecker, and Boris Johannes Nachtsheim. Chiral triazole-substituted iodonium salts in enantioselective halogen bond catalysis. *ChemRxiv*, June 2024. doi: 10.26434/chemrxiv-2024-kkrjl. URL http://dx.doi.org/10.26434/chemrxiv-2024-kkrjl.

[136] Susumu Mitsumori, Haile Zhang, Paul Ha-Yeon Cheong, KN Houk, Fujie Tanaka, and Carlos F Barbas. Direct asymmetric a nti-mannich-type reactions

catalyzed by a designed amino acid. *Journal of the American Chemical Society*, 128(4):1040–1041, 2006.

[137] C. B. Shinisha and Raghavan B. Sunoj. Bicyclic proline analogues as organocatalysts for stereoselective aldol reactions: an in silico dft study. *Organic amp; Biomolecular Chemistry*, 5(8):1287, 2007. ISSN 1477-0539. doi: 10.1039/b701688c. URL http://dx.doi.org/10.1039/b701688c.

[138] Jeremiah P. Malerich, Koji Hagihara, and Viresh H. Rawal. Chiral squaramide derivatives are excellent hydrogen bond donor catalysts. *Journal of the American Chemical Society*, 130(44):14416–14417, October 2008. doi: 10.1021/ja805693p. URL https://doi.org/10.1021/ja805693p.

[139] Andrew J. Neel, Jörg P. Hehn, Pascal F. Tripet, and F. Dean Toste. Asymmetric cross-dehydrogenative coupling enabled by the design and application of chiral triazole-containing phosphoric acids. *Journal of the American Chemical Society*, 135(38):14044–14047, September 2013. ISSN 1520-5126. doi: 10.1021/ja407410b. URL http://dx.doi.org/10.1021/ja407410b.

[140] Datta Markad and Sanjay K. Mandal. Design of a primary-amide-functionalized highly efficient and recyclable hydrogen-bond-donating heterogeneous catalyst for the friedel–crafts alkylation of indoles with -nitrostyrenes. *ACS Catalysis*, 9(4):3165–3173, February 2019. ISSN 2155-5435. doi: 10.1021/acscatal.8b04962. URL http://dx.doi.org/10.1021/acscatal.8b04962.

[141] Sofia Lindblad, Krenare Mehmeti, Alberte X. Veiga, Bijan Nekoueishahraki, Jürgen Gräfenstein, and Máté Erdélyi. Halogen bond asymmetry in solution. *Journal of the American Chemical Society*, 140(41):13503–13513, September 2018. ISSN 1520-5126. doi: 10.1021/jacs.8b09467. URL http://dx.doi.org/10.1021/jacs.8b09467.

[142] Gautam R. Desiraju, P. Shing Ho, Lars Kloo, Anthony C. Legon, Roberto Marquardt, Pierangelo Metrangolo, Peter Politzer, Giuseppe Resnati, and Kari Ris-

sanen. Definition of the halogen bond (iupac recommendations 2013). *Pure and Applied Chemistry*, 85(8):1711–1713, 2013. doi: doi:10.1351/PAC-REC-12-05-10. URL https://doi.org/10.1351/PAC-REC-12-05-10.

[143] Changwei Wang, David Danovich, Yirong Mo, and Sason Shaik. On the nature of the halogen bond. *Journal of Chemical Theory and Computation*, 10(9):3726–3737, July 2014. doi: 10.1021/ct500422t. URL https://doi.org/10.1021/ct500422t.

[144] Raffaella Papagna, Dana Kutzinski, and Stefan M. Huber. Polymer-bound halogen bonding organocatalysis**. *European Journal of Organic Chemistry*, 2022(31), August 2022. ISSN 1099-0690. doi: 10.1002/ejoc.202200852. URL http://dx.doi.org/10.1002/ejoc.202200852.

[145] Stefan H. Jungbauer, David Bulfield, Florian Kniep, Christian W. Lehmann, Eberhardt Herdtweck, and Stefan M. Huber. Toward molecular recognition: Three-point halogen bonding in the solid state and in solution. *Journal of the American Chemical Society*, 136(48):16740–16743, November 2014. ISSN 1520-5126. doi: 10.1021/ja509705f. URL http://dx.doi.org/10.1021/ja509705f.

[146] Stefan H. Jungbauer and Stefan M. Huber. Cationic multidentate halogen-bond donors in halide abstraction organocatalysis: Catalyst optimization by preorganization. *Journal of the American Chemical Society*, 137(37):12110–12120, September 2015. ISSN 1520-5126. doi: 10.1021/jacs.5b07863. URL http://dx.doi.org/10.1021/jacs.5b07863.

[147] Greta Bergamaschi, Luisa Lascialfari, Andrea Pizzi, Maria Isabel Martinez Espinoza, Nicola Demitri, Alberto Milani, Alessandro Gori, and Pierangelo Metrangolo. A halogen bond-donor amino acid for organocatalysis in water. *Chemical Communications*, 54(76):10718–10721, 2018. ISSN 1364-548X. doi: 10.1039/c8cc06010j. URL http://dx.doi.org/10.1039/C8CC06010J.

[148] Alexander Dreger, Elric Engelage, Bert Mallick, Paul D. Beer, and Stefan M.

Huber. The role of charge in 1, 2, 3-triazol(ium)-based halogen bonding activators. *Chemical Communications*, 54(32):4013–4016, 2018. ISSN 1364-548X. doi: 10.1039/c8cc00527c. URL http://dx.doi.org/10.1039/C8CC00527C.

[149] Kohei Matsuzaki, Hiroto Uno, Etsuko Tokunaga, and Norio Shibata. Fluorobissulfonylmethyl iodides: An efficient scaffold for halogen bonding catalysts with an sp3-hybridized carbon–iodine moiety. *ACS Catalysis*, 8(7): 6601–6605, June 2018. ISSN 2155-5435. doi: 10.1021/acscatal.8b01330. URL http://dx.doi.org/10.1021/acscatal.8b01330.

[150] Nils Schulz, Pandian Sokkar, Elric Engelage, Severin Schindler, Mate Erdelyi, Elsa Sanchez-Garcia, and Stefan M. Huber. The interaction modes of haloimidazolium salts in solution. *Chemistry – A European Journal*, 24(14): 3464–3473, December 2017. ISSN 1521-3765. doi: 10.1002/chem.201705032. URL http://dx.doi.org/10.1002/chem.201705032.

[151] Richard A. Squitieri, Keegan P. Fitzpatrick, Ashley A. Jaworski, and Karl A. Scheidt. Synthesis and evaluation of azolium-based halogen-bond donors. *Chemistry – A European Journal*, 25(43):10069–10073, July 2019. ISSN 1521-3765. doi: 10.1002/chem.201902298. URL http://dx.doi.org/10.1002/chem.201902298.

[152] Patrick M. J. Szell, Scott Zablotny, and David L. Bryce. Halogen bonding as a supramolecular dynamics catalyst. *Nature Communications*, 10(1), February 2019. ISSN 2041-1723. doi: 10.1038/s41467-019-08878-8. URL http://dx.doi.org/10.1038/s41467-019-08878-8.

[153] Sebastian M. Walter, Florian Kniep, Laxmidhar Rout, Franz P. Schmidtchen, Eberhardt Herdtweck, and Stefan M. Huber. Isothermal calorimetric titrations on charge-assisted halogen bonds: Role of entropy, counterions, solvent, and temperature. *Journal of the American Chemical Society*, 134(20):8507–8512, May

2012. ISSN 1520-5126. doi: 10.1021/ja2119207. URL http://dx.doi.org/10.1021/ja2119207.

[154] Daniel von der Heiden, Seyma Bozkus, Martin Klussmann, and Martin Breugst. Reaction mechanism of iodine-catalyzed michael additions. *The Journal of Organic Chemistry*, 82(8):4037–4043, April 2017. doi: 10.1021/acs.joc.7b00445. URL https://doi.org/10.1021/acs.joc.7b00445.

[155] Yuk-Cheung Chan and Ying-Yeung Yeung. Halogen-bond-catalyzed addition of carbon-based nucleophiles to n-acylimminium ions. *Organic Letters*, 21(14): 5665–5669, July 2019. ISSN 1523-7052. doi: 10.1021/acs.orglett.9b02006. URL http://dx.doi.org/10.1021/acs.orglett.9b02006.

[156] Timothy Clark, Matthias Hennemann, Jane S. Murray, and Peter Politzer. Halogen bonding: the -hole: Proceedings of "modeling interactions in biomolecules ii", prague, september 5th–9th, 2005. *Journal of Molecular Modeling*, 13(2): 291–296, August 2006. ISSN 0948-5023. doi: 10.1007/s00894-006-0130-2. URL http://dx.doi.org/10.1007/s00894-006-0130-2.

[157] Raphaël Robidas and Claude Y. Legault. Direct pi-activation vs. o-activation in halogen-bonding catalysis. *Angewandte Chemie International Edition*, 62(16): e202301190, March 2023. doi: 10.1002/anie.202301190. URL https://doi.org/10.1002/anie.202301190.

[158] Iñigo Iribarren, Tim Renningtlotz, and Cristina Trujillo. *In silico catalyst design within asymmetric organocatalysis*. Wiley, February 2026.

[159] K. N. Houk and Paul Ha-Yeon Cheong. Computational prediction of small-molecule catalysts. *Nature*, 455(7211):309–313, September 2008. ISSN 1476-4687. doi: 10.1038/nature07368. URL http://dx.doi.org/10.1038/nature07368.

[160] ChristopherR. Corbeil, Sabine Thielges, JeremyA. Schwartzentruber, and Nicolas Moitessier. Toward a computational tool predicting the stereochemical outcome of asymmetric reactions: Development and application of a

rapid and accurate program based on organic principles. *Angewandte Chemie International Edition*, 47(14):2635–2638, March 2008. ISSN 1521-3773. doi: 10.1002/anie.200704774. URL http://dx.doi.org/10.1002/anie.200704774.

[161] Nathanael Weill, Christopher R. Corbeil, Joris W. De Schutter, and Nicolas Moitessier. Toward a computational tool predicting the stereochemical outcome of asymmetric reactions: Development of the molecular mechanics-based program ace and application to asymmetric epoxidation reactions. *Journal of Computational Chemistry*, 32(13):2878–2889, July 2011. ISSN 1096-987X. doi: 10.1002/jcc.21869. URL http://dx.doi.org/10.1002/jcc.21869.

[162] Yanfei Guan, Victoria M. Ingman, Benjamin J. Rooks, and Steven E. Wheeler. Aaron: An automated reaction optimizer for new catalysts. *Journal of Chemical Theory and Computation*, 14(10):5249–5261, August 2018. ISSN 1549-9626. doi: 10.1021/acs.jctc.8b00578. URL http://dx.doi.org/10.1021/acs.jctc.8b00578.

[163] Anthony R. Rosales, Jessica Wahlers, Elaine Limé, Rebecca E. Meadows, Kevin W. Leslie, Rhona Savin, Fiona Bell, Eric Hansen, Paul Helquist, Rachel H. Munday, Olaf Wiest, and Per-Ola Norrby. Rapid virtual screening of enantioselective catalysts using catvs. *Nature Catalysis*, 2(1):41–45, December 2018. ISSN 2520-1158. doi: 10.1038/s41929-018-0193-3. URL http://dx.doi.org/10.1038/s41929-018-0193-3.

[164] Alistair J. Sterling, Stamatia Zavitsanou, Joseph Ford, and Fernanda Duarte. Selectivity in organocatalysis—from qualitative to quantitative predictive models. *WIREs Computational Molecular Science*, 11(5), February 2021. ISSN 1759-0884. doi: 10.1002/wcms.1518. URL http://dx.doi.org/10.1002/wcms.1518.

[165] Nika Melnyk, Iñigo Iribarren, Eric Mates-Torres, and Cristina Trujillo. Theoretical perspectives in organocatalysis. *Chemistry – A European Journal*, 28 (58), August 2022. ISSN 1521-3765. doi: 10.1002/chem.202201570. URL http://dx.doi.org/10.1002/chem.202201570.

[166] Iñigo Iribarren, Marianne Rica Garcia, and Cristina Trujillo. Catalyst design within asymmetric organocatalysis. *WIREs Computational Molecular Science*, 12(6), March 2022. ISSN 1759-0884. doi: 10.1002/wcms.1616. URL http://dx.doi.org/10.1002/wcms.1616.

[167] John A. Keith, Valentin Vassilev-Galindo, Bingqing Cheng, Stefan Chmiela, Michael Gastegger, Klaus-Robert Müller, and Alexandre Tkatchenko. Combining machine learning and computational chemistry for predictive insights into chemical systems. *Chemical Reviews*, 121(16):9816–9872, July 2021. ISSN 1520-6890. doi: 10.1021/acs.chemrev.1c00107. URL http://dx.doi.org/10.1021/acs.chemrev.1c00107.

[168] Takashi Toyao, Zen Maeno, Satoru Takakusagi, Takashi Kamachi, Ichigaku Takigawa, and Ken-ichi Shimizu. Machine learning for catalysis informatics: Recent applications and prospects. *ACS Catalysis*, 10(3):2260–2297, December 2019. ISSN 2155-5435. doi: 10.1021/acscatal.9b04186. URL http://dx.doi.org/10.1021/acscatal.9b04186.

[169] John R. Kitchin. Machine learning in catalysis. *Nature Catalysis*, 1(4):230–232, April 2018. ISSN 2520-1158. doi: 10.1038/s41929-018-0056-y. URL http://dx.doi.org/10.1038/s41929-018-0056-y.

[170] Zheng Li, Siwen Wang, and Hongliang Xin. Toward artificial intelligence in catalysis. *Nature Catalysis*, 1(9):641–642, September 2018. ISSN 2520-1158. doi: 10.1038/s41929-018-0150-1. URL http://dx.doi.org/10.1038/s41929-018-0150-1.

[171] Wenhong Yang, Timothy Tizhe Fidelis, and Wen-Hua Sun. Machine learning in catalysis, from proposal to practicing. *ACS Omega*, 5(1):83–88, December 2019. ISSN 2470-1343. doi: 10.1021/acsomega.9b03673. URL http://dx.doi.org/10.1021/acsomega.9b03673.

[172] Jacques A. Esterhuizen, Bryan R. Goldsmith, and Suljo Linic. Inter-

pretable machine learning for knowledge generation in heterogeneous catalysis. *Nature Catalysis*, 5(3):175–184, March 2022. ISSN 2520-1158. doi: 10.1038/s41929-022-00744-z. URL http://dx.doi.org/10.1038/s41929-022-00744-z.

[173] Fernando Gomollón-Bel. Ten chemical innovations that will change our world: Iupac identifies emerging technologies in chemistry with potential to make our planet more sustainable. *Chemistry International*, 41(2):12–17, April 2019. ISSN 0193-6484. doi: 10.1515/ci-2019-0203. URL http://dx.doi.org/10.1515/ci-2019-0203.

[174] Wenhong Yang, Timothy Tizhe Fidelis, and Wen-Hua Sun. Machine learning in catalysis, from proposal to practicing. *ACS omega*, 5(1):83–88, 2019.

[175] Andrew F Zahrt, Jeremy J Henle, Brennan T Rose, Yang Wang, William T Darrow, and Scott E Denmark. Prediction of higher-selectivity catalysts by computer-driven workflow and machine learning. *Science*, 363(6424):eaau5631, 2019.

[176] Christoph Grondal, Matthieu Jeanty, and Dieter Enders. Organocatalytic cascade reactions as a new tool in total synthesis. *Nature chemistry*, 2(3):167–178, 2010.

[177] Yong Huang, Abbas M Walji, Catharine H Larsen, and David WC MacMillan. Enantioselective organo-cascade catalysis. *Journal of the American Chemical Society*, 127(43):15051–15053, 2005.

[178] Bruce A Arndtsen and Liu-Zhu Gong. *Asymmetric organocatalysis combined with metal catalysis*. Springer, 2020.

[179] Dian-Feng Chen and Liu-Zhu Gong. Organo/transition-metal combined catalysis rejuvenates both in asymmetric synthesis. *Journal of the American Chemical Society*, 144(6):2415–2437, 2022.

[180] Bryon Simmons, Abbas M Walji, and David WC MacMillan. Cycle-specific organocascade catalysis: application to olefin hydroamination, hydro-oxidation, and amino-oxidation, and to natural product synthesis. *Angewandte Chemie*, 121(24):4413–4417, 2009.

[181] Simon Krautwald, David Sarlah, Michael A Schafroth, and Erick M Carreira. Enantio-and diastereodivergent dual catalysis: α-allylation of branched aldehydes. *Science*, 340(6136):1065–1068, 2013.

[182] Kevin J Schwarz, Jessica L Amos, J Cullen Klein, Dung T Do, and Thomas N Snaddon. Uniting c1-ammonium enolates and transition metal electrophiles via cooperative catalysis: the direct asymmetric α-allylation of aryl acetic acid esters. *Journal of the American Chemical Society*, 138(16):5214–5217, 2016.

[183] Adam Trotta and Eric N Jacobsen. Chiral ureas, thioureas, and squaramides in anion-binding catalysis with co-catalytic b rønsted/l ewis acids. *Anion-Binding Catalysis*, pages 141–159, 2022.

[184] G PUPO, AC VICINI, DMH ASCOUGH, F IBBA, KE CHRISTENSEN, and AL THOMPSON. Jm brown, rs paton, v. gouverneur*(university of oxford, uk and colorado state university, fort collins, usa). *J. Am. Chem. Soc*, 141:2878–2883, 2019.

[185] Martin Breugst and Jonas J Koenig. σ-hole interactions in catalysis. *European Journal of Organic Chemistry*, 2020(34):5473–5487, 2020.

[186] Stefan Huber. *Halogen Bonding in Solution*. John Wiley & Sons, 2021.

[187] Pierangelo Metrangolo, Hannes Neukirch, Tullio Pilati, and Giuseppe Resnati. Halogen bonding based recognition processes: a world parallel to hydrogen bonding. *Accounts of Chemical Research*, 38(5):386–395, March 2005. doi: 10.1021/ar0400995. URL `https://doi.org/10.1021/ar0400995`.

[188] Arijit Mukherjee, Srinu Tothadi, and Gautam R. Desiraju. Halogen bonds in crystal engineering: Like hydrogen bonds yet different. *Accounts of Chemical Research*, 47(8):2514–2524, May 2014. doi: 10.1021/ar5001555. URL https://doi.org/10.1021/ar5001555.

[189] Hui Li, Bai-Ru Ai, and Miao Hong. Stereoselective ring-opening polymerization of rac-lactide by bulky chiral and achiral n-heterocyclic carbenes. *Chinese Journal of Polymer Science*, 36(2):231–236, November 2017. ISSN 1439-6203. doi: 10.1007/s10118-018-2071-5. URL http://dx.doi.org/10.1007/s10118-018-2071-5.

[190] Flemming Heinen, Elric Engelage, Alexander Dreger, Robert Weiss, and Stefan M. Huber. Iodine(iii) derivatives as halogen bonding organocatalysts. *Angewandte Chemie International Edition*, 57(14):3830–3833, March 2018. ISSN 1521-3773. doi: 10.1002/anie.201713012. URL http://dx.doi.org/10.1002/anie.201713012.

[191] Flemming Heinen, Elric Engelage, Christopher J. Cramer, and Stefan M. Huber. Hypervalent iodine(iii) compounds as biaxial halogen bond donors. *Journal of the American Chemical Society*, 142(19):8633–8640, April 2020. ISSN 1520-5126. doi: 10.1021/jacs.9b13309. URL http://dx.doi.org/10.1021/jacs.9b13309.

[192] Flemming Heinen, Dominik L. Reinhard, Elric Engelage, and Stefan M. Huber. A bidentate iodine(iii)-based halogen-bond donor as a powerful organocatalyst**. *Angewandte Chemie International Edition*, 60(10):5069–5073, January 2021. ISSN 1521-3773. doi: 10.1002/anie.202013172. URL http://dx.doi.org/10.1002/anie.202013172.

[193] Raphaël Robidas, Dominik L. Reinhard, Claude Y. Legault, and Stefan M. Huber. Iodine(iii)-based halogen bond donors: Properties and applications. *The Chemical Record*, 21(8):1912–1927, June 2021. ISSN 1528-0691. doi: 10.1002/tcr.202100119. URL http://dx.doi.org/10.1002/tcr.202100119.

[194] Susana Portela, Jorge J. Cabrera-Trujillo, and Israel Fernandez. Catalysis by bidentate iodine(iii)-based halogen donors: Surpassing the activity of strong lewis acids. *The Journal of Organic Chemistry*, 86(7):5317–5326, 2021. ISSN 0022-3263. doi: 10.1021/acs.joc.1c00534.

[195] Florian Weigend and Reinhart Ahlrichs. Balanced basis sets of split valence, triple zeta valence and quadruple zeta valence quality for h to rn: Design and assessment of accuracy. *Physical Chemistry Chemical Physics*, 7(18):3297, 2005. doi: 10.1039/b508541a. URL https://doi.org/10.1039/b508541a.

[196] LOUIS DE BROGLIE. Waves and quanta. *Nature*, 112(2815):540–540, October 1923. ISSN 1476-4687. doi: 10.1038/112540a0. URL http://dx.doi.org/10.1038/112540a0.

[197] E. Schrödinger. Quantisierung als eigenwertproblem. *Annalen der Physik*, 385 (13):437–490, January 1926. ISSN 1521-3889. doi: 10.1002/andp.19263851302. URL http://dx.doi.org/10.1002/andp.19263851302.

[198] D. R. Hartree. The wave mechanics of an atom with a non-coulomb central field. part i. theory and methods. *Mathematical Proceedings of the Cambridge Philosophical Society*, 24(1):89–110, January 1928. ISSN 1469-8064. doi: 10.1017/s0305004100011919. URL http://dx.doi.org/10.1017/S0305004100011919.

[199] V. Fock. Nherungsmethode zur lsung des quantenmechanischen mehrkrperproblems. *Zeitschrift fr Physik*, 61(1–2):126–148, January 1930. ISSN 1434-601X. doi: 10.1007/bf01340294. URL http://dx.doi.org/10.1007/BF01340294.

[200] J. C. Slater. Note on hartree's method. *Physical Review*, 35(2):210–211, January 1930. ISSN 0031-899X. doi: 10.1103/physrev.35.210.2. URL http://dx.doi.org/10.1103/PhysRev.35.210.2.

[201] Chr. Møller and M. S. Plesset. Note on an approximation treatment for many-electron systems. *Physical Review*, 46(7):618–622, October 1934. ISSN 0031-899X.

doi: 10.1103/physrev.46.618. URL http://dx.doi.org/10.1103/PhysRev.46.618.

[202] E. U. Condon and G. H. Shortley. The theory of complex spectra ii. *Physical Review*, 37(9):1025–1043, May 1931. ISSN 0031-899X. doi: 10.1103/physrev.37.1025. URL http://dx.doi.org/10.1103/PhysRev.37.1025.

[203] E. U. Condon. The theory of complex spectra. *Physical Review*, 36(7):1121–1133, October 1930. ISSN 0031-899X. doi: 10.1103/physrev.36.1121. URL http://dx.doi.org/10.1103/PhysRev.36.1121.

[204] John A. Pople, Martin Head-Gordon, and Krishnan Raghavachari. Quadratic configuration interaction. a general technique for determining electron correlation energies. *The Journal of Chemical Physics*, 87(10):5968–5975, November 1987. ISSN 1089-7690. doi: 10.1063/1.453520. URL http://dx.doi.org/10.1063/1.453520.

[205] Krishnan Raghavachari, Gary W. Trucks, John A. Pople, and Martin Head-Gordon. A fifth-order perturbation comparison of electron correlation theories. *Chemical Physics Letters*, 157(6):479–483, May 1989. ISSN 0009-2614. doi: 10.1016/s0009-2614(89)87395-6. URL http://dx.doi.org/10.1016/S0009-2614(89)87395-6.

[206] Jiří Čížek. On the correlation problem in atomic and molecular systems. calculation of wavefunction components in ursell-type expansion using quantum-field theoretical methods. *The Journal of Chemical Physics*, 45(11):4256–4266, December 1966. ISSN 1089-7690. doi: 10.1063/1.1727484. URL http://dx.doi.org/10.1063/1.1727484.

[207] Hendrik J. Monkhorst. Calculation of properties with the coupled-cluster method. *International Journal of Quantum Chemistry*, 12(S11):421–432, June 2009. ISSN 1097-461X. doi: 10.1002/qua.560120850. URL http://dx.doi.org/10.1002/qua.560120850.

[208] W. Kohn and L. J. Sham. Self-consistent equations including exchange and correlation effects. *Physical Review*, 140(4A):A1133–A1138, November 1965. ISSN 0031-899X. doi: 10.1103/physrev.140.a1133. URL http://dx.doi.org/10.1103/PhysRev.140.A1133.

[209] J. P. Perdew, E. R. McMullen, and Alex Zunger. Density-functional theory of the correlation energy in atoms and ions: A simple analytic model and a challenge. *Physical Review A*, 23(6):2785–2789, June 1981. ISSN 0556-2791. doi: 10.1103/physreva.23.2785. URL http://dx.doi.org/10.1103/PhysRevA.23.2785.

[210] John P. Perdew and Yue Wang. Accurate and simple analytic representation of the electron-gas correlation energy. *Physical Review B*, 45(23):13244–13249, June 1992. ISSN 1095-3795. doi: 10.1103/physrevb.45.13244. URL http://dx.doi.org/10.1103/PhysRevB.45.13244.

[211] S. H. Vosko, L. Wilk, and M. Nusair. Accurate spin-dependent electron liquid correlation energies for local spin density calculations: a critical analysis. *Canadian Journal of Physics*, 58(8):1200–1211, August 1980. ISSN 1208-6045. doi: 10.1139/p80-159. URL http://dx.doi.org/10.1139/p80-159.

[212] P. A. M. Dirac. Note on exchange phenomena in the thomas atom. *Mathematical Proceedings of the Cambridge Philosophical Society*, 26(3):376–385, July 1930. ISSN 1469-8064. doi: 10.1017/s0305004100016108. URL http://dx.doi.org/10.1017/S0305004100016108.

[213] Teepanis Chachiyo. Communication: Simple and accurate uniform electron gas correlation energy for the full range of densities. *The Journal of Chemical Physics*, 145(2), July 2016. ISSN 1089-7690. doi: 10.1063/1.4958669. URL http://dx.doi.org/10.1063/1.4958669.

[214] Louis A Girifalco. *Statistical mechanics of solids*. Monographs on the Physics and Chemistry of Materials. Oxford University Press, New York, NY, July 2005.

[215] O. Gunnarsson and B. I. Lundqvist. Exchange and correlation in atoms, molecules, and solids by the spin-density-functional formalism. *Physical Review B*, 13(10):4274–4298, May 1976. ISSN 0556-2805. doi: 10.1103/physrevb.13.4274. URL http://dx.doi.org/10.1103/PhysRevB.13.4274.

[216] John P. Perdew. Density-functional approximation for the correlation energy of the inhomogeneous electron gas. *Physical Review B*, 33(12):8822–8824, June 1986. ISSN 0163-1829. doi: 10.1103/physrevb.33.8822. URL http://dx.doi.org/10.1103/PhysRevB.33.8822.

[217] A. D. Becke. Density-functional exchange-energy approximation with correct asymptotic behavior. *Physical Review A*, 38(6):3098–3100, September 1988. ISSN 0556-2791. doi: 10.1103/physreva.38.3098. URL http://dx.doi.org/10.1103/PhysRevA.38.3098.

[218] Chengteh Lee, Weitao Yang, and Robert G. Parr. Development of the colle-salvetti correlation-energy formula into a functional of the electron density. *Physical Review B*, 37(2):785–789, January 1988. ISSN 0163-1829. doi: 10.1103/physrevb.37.785. URL http://dx.doi.org/10.1103/physrevb.37.785.

[219] Yan Zhao and Donald G. Truhlar. The m06 suite of density functionals for main group thermochemistry, thermochemical kinetics, noncovalent interactions, excited states, and transition elements: two new functionals and systematic testing of four m06-class functionals and 12 other functionals. *Theoretical Chemistry Accounts*, 120(1–3):215–241, July 2007. ISSN 1432-2234. doi: 10.1007/s00214-007-0310-x. URL http://dx.doi.org/10.1007/s00214-007-0310-x.

[220] O. Gunnarsson and B. I. Lundqvist. Exchange and correlation in atoms, molecules, and solids by the spin-density-functional formalism. *Physical Review B*, 13(10):4274–4298, May 1976. ISSN 0556-2805. doi: 10.1103/physrevb.13.4274. URL http://dx.doi.org/10.1103/PhysRevB.13.4274.

[221] Stefan Kurth, John P. Perdew, and Peter Blaha. Molecular and solid-state tests of

density functional approximations: Lsd, ggas, and meta-ggas. *International Journal of Quantum Chemistry*, 75(4–5):889–909, 1999. ISSN 1097-461X. doi: 10.1002/(sici)1097-461x(1999)75:4/5<889::aid-qua54>3.0.co;2-8. URL http://dx.doi.org/10.1002/(SICI)1097-461X(1999)75:4/5<889::AID-QUA54>3.0.CO;2-8.

[222] J Harris and R O Jones. The surface energy of a bounded electron gas. *Journal of Physics F: Metal Physics*, 4(8):1170–1186, August 1974. ISSN 0305-4608. doi: 10.1088/0305-4608/4/8/013. URL http://dx.doi.org/10.1088/0305-4608/4/8/013.

[223] Axel D. Becke. A new mixing of hartree–fock and local density-functional theories. *The Journal of Chemical Physics*, 98(2):1372–1377, January 1993. ISSN 1089-7690. doi: 10.1063/1.464304. URL http://dx.doi.org/10.1063/1.464304.

[224] Edmanuel Torres and Gino A. DiLabio. A (nearly) universally applicable method for modeling noncovalent interactions using b3lyp. *The Journal of Physical Chemistry Letters*, 3(13):1738–1744, June 2012. ISSN 1948-7185. doi: 10.1021/jz300554y. URL http://dx.doi.org/10.1021/jz300554y.

[225] Stefan Grimme, Jens Antony, Tobias Schwabe, and Christian Mück-Lichtenfeld. Density functional theory with dispersion corrections for supramolecular structures, aggregates, and complexes of (bio)organic molecules. *Org. Biomol. Chem.*, 5(5):741–758, 2007. ISSN 1477-0539. doi: 10.1039/b615319b. URL http://dx.doi.org/10.1039/B615319B.

[226] Jeng-Da Chai and Martin Head-Gordon. Long-range corrected hybrid density functionals with damped atom–atom dispersion corrections. *Physical Chemistry Chemical Physics*, 10(44):6615, 2008. ISSN 1463-9084. doi: 10.1039/b810189b. URL http://dx.doi.org/10.1039/B810189B.

[227] Lars Goerigk and Stefan Grimme. Double-hybrid density functionals. *WIREs Computational Molecular Science*, 4(6):576–600, July 2014. ISSN 1759-0884. doi: 10.1002/wcms.1193. URL http://dx.doi.org/10.1002/wcms.1193.

[228] J E Lennard-Jones. Cohesion. *Proceedings of the Physical Society*, 43(5):461–482, September 1931. ISSN 0959-5309. doi: 10.1088/0959-5309/43/5/301. URL http://dx.doi.org/10.1088/0959-5309/43/5/301.

[229] R McWEENY. Gaussian approximations to wave functions. *Nature*, 166(4209): 21–22, July 1950.

[230] Jan Almlöf and Peter R Taylor. General contraction of gaussian basis sets. i. atomic natural orbitals for first- and second-row atoms. *J. Chem. Phys.*, 86(7): 4070–4077, April 1987.

[231] Per-Olof Widmark, Per-ke Malmqvist, and Bjrn O Roos. Density matrix averaged atomic natural orbital (ANO) basis sets for correlated molecular wave functions. *Theoret. Chim. Acta*, 77(5):291–306, 1990.

[232] Kirk A Peterson and Thom H Dunning, Jr. Accurate correlation consistent basis sets for molecular core–valence correlation effects: The second row atoms Al–Ar, and the first row atoms B–Ne revisited. *J. Chem. Phys.*, 117(23):10548–10560, December 2002.

[233] Michael J. Frisch, John A. Pople, and J. Stephen Binkley. Self-consistent molecular orbital methods 25. supplementary functions for gaussian basis sets. *The Journal of Chemical Physics*, 80(7):3265–3269, April 1984. ISSN 1089-7690. doi: 10.1063/1.447079. URL http://dx.doi.org/10.1063/1.447079.

[234] P. C. Hariharan and J. A. Pople. The influence of polarization functions on molecular orbital hydrogenation energies. *Theoretica Chimica Acta*, 28 (3):213–222, 1973. ISSN 1432-2234. doi: 10.1007/bf00533485. URL http://dx.doi.org/10.1007/BF00533485.

[235] Thom H. Dunning. Gaussian basis sets for use in correlated molecular calculations. i. the atoms boron through neon and hydrogen. *The Journal of Chemical Physics*, 90(2):1007–1023, January 1989. ISSN 1089-7690. doi: 10.1063/1.456153. URL http://dx.doi.org/10.1063/1.456153.

[236] Arnim Hellweg and Dmitrij Rappoport. Development of new auxiliary basis functions of the karlsruhe segmented contracted basis sets including diffuse basis functions (def2-svpd, def2-tzvppd, and def2-qvppd) for ri-mp2 and ri-cc calculations. *Physical Chemistry Chemical Physics*, 17(2):1010–1017, 2015. ISSN 1463-9084. doi: 10.1039/c4cp04286g. URL http://dx.doi.org/10.1039/C4CP04286G.

[237] R. Krishnan, J. S. Binkley, R. Seeger, and J. A. Pople. Self-consistent molecular orbital methods. xx. a basis set for correlated wave functions. *The Journal of Chemical Physics*, 72(1):650–654, January 1980. ISSN 1089-7690. doi: 10.1063/1.438955. URL http://dx.doi.org/10.1063/1.438955.

[238] C. F. Matta and R. J. Gillespie. Understanding and interpreting molecular electron density distributions. *Journal of Chemical Education*, 79(9):1141, September 2002. ISSN 1938-1328. doi: 10.1021/ed079p1141. URL http://dx.doi.org/10.1021/ed079p1141.

[239] Richard F W Bader, Marshall T Carroll, James R Cheeseman, and Cheng Chang. Properties of atoms in molecules: atomic volumes. *Journal of the American Chemical Society*, 109(26):7968–7979, 1987. ISSN 0002-7863. doi: 10.1021/ja00260a006.

[240] Paul Popelier and Patrick Bultinck. *Atoms in Molecules and Population Analysis*. CRC Press, February 2009. ISBN 9781420065442. doi: 10.1201/9781420065442.ch15. URL http://dx.doi.org/10.1201/9781420065442.ch15.

[241] Erich Runge and E. K. U. Gross. Density-functional theory for time-dependent systems. *Physical Review Letters*, 52(12):997–1000, March 1984. ISSN 0031-9007. doi: 10.1103/physrevlett.52.997. URL http://dx.doi.org/10.1103/PhysRevLett.52.997.

[242] Frank Weinhold and Clark R. Landis. *Valency and Bonding: A Natural Bond Orbital Donor-Acceptor Perspective*. Cambridge University Press, October 2003.

ISBN 9780511614569. doi: 10.1017/cbo9780511614569. URL http://dx.doi.org/10.1017/CBO9780511614569.

[243] Benjamin D. Dunnington and J. R. Schmidt. Generalization of natural bond orbital analysis to periodic systems: Applications to solids and surfaces via plane-wave density functional theory. *Journal of Chemical Theory and Computation*, 8(6):1902–1911, May 2012. ISSN 1549-9626. doi: 10.1021/ct300002t. URL http://dx.doi.org/10.1021/ct300002t.

[244] Alan E. Reed, Larry A. Curtiss, and Frank Weinhold. A. e. reed, l. a. curtiss, f. weinhold. *Chemical Reviews*, 88(6):899–926, 1988. doi: 10.1021/cr00088a005.

[245] Shuaifei Guo, Cuihong Sun, Lingpeng Meng, and Yanli Zeng. The mechanism of ring-opening polymerization of l-lactide by icl3 catalysts: Halogen bond catalysis or participating in reactions? *Journal of Computational Chemistry*, 40 (32):2827–2833, August 2019. ISSN 1096-987X. doi: 10.1002/jcc.26059. URL http://dx.doi.org/10.1002/jcc.26059.

[246] Jeng-Da Chai and Martin Head-Gordon. Long-range corrected hybrid density functionals with damped atom-atom dispersion corrections. *Phys. Chem. Chem. Phys.*, 10(44):6615–6620, November 2008.

[247] Ansgar Schäfer, Hans Horn, and Reinhart Ahlrichs. Fully optimized contracted gaussian basis sets for atoms li to kr. *J. Chem. Phys.*, 97(4):2571–2577, August 1992.

[248] Florian Weigend. Accurate coulomb-fitting basis sets for h to rn. *Physical Chemistry Chemical Physics*, 8(9):1057, 2006. ISSN 1463-9084. doi: 10.1039/b515623h. URL http://dx.doi.org/10.1039/b515623h.

[249] M J Frisch et al. Gaussian 16 rev. c.01, 2016.

[250] Aleksandr V. Marenich, Christopher J. Cramer, and Donald G. Truhlar. Universal solvation model based on solute electron density and on a continuum

model of the solvent defined by the bulk dielectric constant and atomic surface tensions. *The Journal of Physical Chemistry B*, 113(18):6378–6396, April 2009. ISSN 1520-5207. doi: 10.1021/jp810292n. URL http://dx.doi.org/10.1021/jp810292n.

[251] Tian Lu and Feiwu Chen. Multiwfn: A multifunctional wavefunction analyzer. *Journal of Computational Chemistry*, 33(5):580–592, December 2011. ISSN 1096-987X. doi: 10.1002/jcc.22885. URL http://dx.doi.org/10.1002/jcc.22885.

[252] Jmol development team. Jmol. URL http://jmol.sourceforge.net/.

[253] E. D. Glendening, J. K. Badenhoop, A. E. Reed, J. E. Carpenter, J. A. Bohmann, C. M. Morales, and C. R. Weinhold F. Karafiloglou, P. Landis. Nbo 7.0., 2018.

[254] Lucius E. Johnson and Donald B. DuPré. Topological and orbital-based mechanisms of the electronic stabilization of bis(diisopropylamino)cyclopropenylidene. *The Journal of Physical Chemistry A*, 112(32):7448–7454, July 2008. ISSN 1520-5215. doi: 10.1021/jp802214u. URL http://dx.doi.org/10.1021/jp802214u.

[255] P SHYAM VINOD KUMAR, V RAGHAVENDRA, and V SUBRAMANIAN. Bader's theory of atoms in molecules (aim) and its applications to chemical bonding. *Journal of Chemical Sciences*, 128(10):1527–1536, October 2016. ISSN 0973-7103. doi: 10.1007/s12039-016-1172-3. URL http://dx.doi.org/10.1007/s12039-016-1172-3.

[256] Yong-Xing Song and Da-Ming Du. Recent advances in catalytic asymmetric aza-michael addition triggered cascade reactions. *Advanced Synthesis amp; Catalysis*, 363(20):4667–4694, September 2021. ISSN 1615-4169. doi: 10.1002/adsc.202100624. URL http://dx.doi.org/10.1002/adsc.202100624.

[257] Yuan Kou, Jianjun Lu, and Yuanqi Yin. Supported tetranuclear carbonyl clusters: 1. framework distortion and catalytic activity in hydroformylation.

Catalysis Letters, 2(3):157–163, 1989. ISSN 1572-879X. doi: 10.1007/bf00775065. URL http://dx.doi.org/10.1007/BF00775065.

[258] Ajoy K Banerjee, Willliam Vera, Henry Mora, Manuel S Laya, Liadis Bedoya, and Elvia V Cabrera. Iodine in organic synthesis j. sci ind. res. 65:299–308, 2006.

[259] Marjan Jereb, Dejan Vražič, and Marko Zupan. Iodine-catalyzed transformation of molecules containing oxygen functional groups. *Tetrahedron*, 67(7): 1355–1387, 2011.

[260] Martin Breugst and Daniel von der Heiden. Mechanisms in iodine catalysis. *Chemistry - A European Journal*, 24(37):9187–9199, April 2018. doi: 10.1002/chem.201706136. URL https://doi.org/10.1002/chem.201706136.

[261] Stojan Stavber, Marjan Jereb, and Marko Zupan. Electrophilic iodination of organic compounds using elemental iodine or iodides. *Synthesis*, 2008(10): 1487–1513, May 2008. doi: 10.1055/s-2008-1067037. URL https://doi.org/10.1055/s-2008-1067037.

[262] Njomza Ajvazi and Stojan Stavber. Electrophilic iodination of organic compounds using elemental iodine or iodides: Recent advances 2008-2021: Part i. *Compounds*, 2(1):3–24, 2022. ISSN 2673-6918. doi: 10.3390/compounds2010002. URL https://www.mdpi.com/2673-6918/2/1/2.

[263] Hirokatsu Nagura, Shunsuke Kuribayashi, Yutaka Ishiguro, Shinsuke Inagi, and Toshio Fuchigami. Electrochemical iodofluorination of electron-deficient olefins. *Tetrahedron*, 66(1):183–186, 2010. ISSN 0040-4020. doi: https://doi.org/10.1016/j.tet.2009.11.005. URL https://www.sciencedirect.com/science/article/pii/S0040402009016950.

[264] J. Armando Luján-Montelongo, Jeferson B. Mateus-Ruiz, and Ricardo M. Valdez-García. Iodine and iodide in reductive transformations. *Euro-*

pean Journal of Organic Chemistry, 26(9):e202201156, February 2023. doi: 10.1002/ejoc.202201156. URL https://doi.org/10.1002/ejoc.202201156.

[265] Flemming Heinen, Elric Engelage, Alexander Dreger, Robert Weiss, and Stefan M. Huber. Iodine(iii) derivatives as halogen bonding organocatalysts. *Angewandte Chemie International Edition*, 57(14):3830–3833, 2018. doi: 10.1002/anie.201713012.

[266] Flemming Heinen, Elric Engelage, Christopher J. Cramer, and Stefan M. Huber. Hypervalent iodine(iii) compounds as biaxial halogen bond donors. *Journal of the American Chemical Society*, 142(19):8633–8640, 2020. doi: 10.1021/jacs.9b13309.

[267] Flemming Heinen, Dominik L. Reinhard, Elric Engelage, and Stefan M. Huber. A bidentate iodine(iii)-based halogen-bond donor as a powerful organocatalyst**. *Angewandte Chemie International Edition*, 60(10):5069–5073, 2021. doi: 10.1002/anie.202013172.

[268] Raphaël Robidas, Dominik L. Reinhard, Claude Y. Legault, and Stefan M. Huber. Iodine(iii)-based halogen bond donors: Properties and applications. *The Chemical Record*, 21(8):1912–1927, 2021. doi: 10.1002/tcr.202100119.

[269] P. Muller. Glossary of terms used in physical organic chemistry (iupac recommendations 1994). *Pure and Applied Chemistry*, 66(5):1124, 1994. doi: doi:10.1351/pac199466051077. URL https://doi.org/10.1351/pac199466051077.

[270] P. Muller. Glossary of terms used in physical organic chemistry (iupac recommendations 1994). *Pure and Applied Chemistry*, 66(5):1139, 1994. doi: doi:10.1351/pac199466051077. URL https://doi.org/10.1351/pac199466051077.

[271] Jonathan Clayden, Nick Greeves, and Stuart Warren. *Chapter 21 Electrophilic Aromatic Substitution*, pages 471–491. Oxford University Press, Oxford, New York, 2nd edition, 2012.

[272] Timothy Clark, Matthias Hennemann, Jane S. Murray, and Peter Politzer. Halogen bonding: the -hole. *Journal of Molecular Modeling*, 13(2):291–296, 2007. doi: 10.1007/s00894-006-0130-2.

[273] Jonathan Clayden, Nick Greeves, and Stuart Warren. *Chapter 8 Acidity, Basicity, and pKa*, pages 175–176. Oxford University Press, Oxford, New York, 2nd edition, 2012.

[274] Piotr Bałczewski, Emilia Kowalska, Ewa Różycka-Sokołowska, Paweł Uznański, Joanna Wilk, Marek Koprowski, Krzysztof Owsianik, and Bernard Marciniak. Organosulfur materials with high photo- and photo-oxidation stability: 10-anthryl sulfoxides and sulfones and their photophysical properties dependent on the sulfur oxidation state. *Materials*, 14(13):3506, 2021. doi: 10.3390/ma14133506.

[275] David Givaudan, Bohdan Biletskyi, Antonio Recupido, Virginie Héran, Olivier Chuzel, Thierry Constantieux, Jean-Luc Parrain, and Xavier Bugaut. Bifunctional iodoazolium salts: Searching for cooperation between halogen bonding and hydrogen bonding. *European Journal of Organic Chemistry*, 27(15): e202300261, 2024. doi: https://doi.org/10.1002/ejoc.202300261.

[276] Rhianon K Rowe and P Shing Ho. Relationships between hydrogen bonds and halogen bonds in biological systems. *Acta Crystallogr. B Struct. Sci. Cryst. Eng. Mater.*, 73(2):255–264, April 2017.

[277] Janaka C Gamekkanda, Abhijeet S Sinha, John Desper, Marijana Đaković, and Christer B Aakeröy. Competition between hydrogen bonds and halogen bonds: a structural study. *New J. Chem.*, 42(13):10539–10547, 2018.

[278] Sean W Robinson, Chantal L Mustoe, Nicholas G White, Asha Brown, Amber L Thompson, Pierre Kennepohl, and Paul D Beer. Evidence for halogen bond covalency in acyclic and interlocked halogen-bonding receptor anion recognition. *J. Am. Chem. Soc.*, 137(1):499–507, January 2015.

[279] Ronny Tepper, Benjamin Schulze, Helmar Görls, Peter Bellstedt, Michael Jäger, and Ulrich S Schubert. Preorganization in a cleft-type anion receptor featuring iodo-1,2,3-triazoles as halogen bond donors. *Org. Lett.*, 17(23):5740–5743, December 2015.

[280] Asia Marie S. Riel, Daniel A. Decato, Jiyu Sun, Casey J. Massena, Morly J. Jessop, and Orion B. Berryman. The intramolecular hydrogen bonded–halogen bond: a new strategy for preorganization and enhanced binding. *Chemical Science*, 9(26):5828–5836, 2018. ISSN 2041-6539. doi: 10.1039/c8sc01973h. URL http://dx.doi.org/10.1039/C8SC01973H.

[281] Yusuke Kobayashi, Yuya Nakatsuji, Shanji Li, Seiji Tsuzuki, and Yoshiji Takemoto. Direct n-glycofunctionalization of amides with glycosyl trichloroacetimidate by thiourea/halogen bond donor co-catalysis. *Angewandte Chemie International Edition*, 57(14):3646–3650, March 2018. ISSN 1521-3773. doi: 10.1002/anie.201712726. URL http://dx.doi.org/10.1002/anie.201712726.

[282] Stefan H. Jungbauer and Stefan M. Huber. Cationic multidentate halogen-bond donors in halide abstraction organocatalysis: Catalyst optimization by preorganization. *Journal of the American Chemical Society*, 137(37):12110–12120, 2015. doi: 10.1021/jacs.5b07863.

[283] Kevin E. Riley and Khanh-An Tran. Strength, character, and directionality of halogen bonds involving cationic halogen bond donors. *Faraday Discussions*, 203:47–60, 2017. ISSN 1359-6640. doi: 10.1039/C7FD00106A.

[284] Luka Fotović, Nikola Bedeković, and Vladimir Stilinović. Evaluation of halogenopyridinium cations as halogen bond donors. *Crystal Growth & Design*, 21(12):6889–6901, 2021. ISSN 1528-7483. doi: 10.1021/acs.cgd.1c00805.

[285] Ingo Krossing and Ines Raabe. Noncoordinating anions—fact or fiction? a survey of likely candidates. *Angewandte Chemie International Edition*, 43(16): 2066–2090, 2004. doi: https://doi.org/10.1002/anie.200300620.

[286] Fabian Scharinger, Ádám Márk Pálvölgyi, Veronika Zeindlhofer, Michael Schnürch, Christian Schröder, and Katharina Bica-Schröder. Counterion enhanced organocatalysis: A novel approach for the asymmetric transfer hydrogenation of enones. *ChemCatChem*, 12(14):3776–3782, 2020. doi: https://doi.org/10.1002/cctc.202000414.

[287] Juan Angel de Gracia Triviño and Mårten S. G. Ahlquist. The Role of Counterions in Intermolecular Radical Coupling of Ru-bda Catalysts. *Topics in Catalysis*, 65(1-4):383–391, 2022. ISSN 1022-5528. doi: 10.1007/s11244-021-01492-3.

[288] Alexandra A. Sysoeva, Yana V. Safinskaya, Mikhail V. Il'in, Alexander S. Novikov, and Dmitrii S. Bolotin. Halonium and chalconium salt-catalyzed schiff condensation: kinetics and dft insights into organocatalyst activity parameters. *Org. Biomol. Chem.*, 23:1970–1980, 2025. doi: 10.1039/D4OB01798F.

[289] Philipp Erdmann, Manuel Schmitt, Lukas M. Sigmund, Felix Krämer, Frank Breher, and Lutz Greb. How to deal with charge in the ranking of lewis acidity: Critical evaluation of an extensive set of cationic lewis acids. *Angewandte Chemie International Edition*, 63(22):e202403356, 2024. doi: https://doi.org/10.1002/anie.202403356.

[290] Dominik L. Reinhard, Anna Iniutina, Sven Reese, Tushar Shaw, Christian Merten, Benjamin List, and Stefan M. Huber. Asymmetric counteranion-directed halogen bonding catalysis. *Journal of the American Chemical Society*, 2025. ISSN 0002-7863. doi: 10.1021/jacs.4c18378.

[291] Andreas Klamt and Volker Jonas. Treatment of the outlying charge in continuum solvation models. *The Journal of Chemical Physics*, 105(22):9972–9981, 1996. ISSN 0021-9606. doi: 10.1063/1.472829.

[292] Yan Zhao and Donald Truhlar. The m06 suite of density functionals for main group thermochemistry, thermochemical kinetics, noncovalent interactions, excited states, and transition elements: two new functionals and systematic

testing of four m06 functionals and 12 other functionals. *Theoretical Chemistry Accounts*, 120:215–241, 04 2008. doi: 10.1007/s00214-007-0310-x.

[293] Florian Weigend. Accurate coulomb-fitting basis sets for h to rn. *Physical Chemistry Chemical Physics*, 8(9):1057–1065, 2006. ISSN 1463-9076. doi: 10.1039/b515623h.

[294] Sebastian Kozuch and Jan M. L. Martin. Halogen bonds: Benchmarks and theoretical analysis. *Journal of Chemical Theory and Computation*, 9(4):1918–1931, 2013. ISSN 1549-9618. doi: 10.1021/ct301064t.

[295] Narbe Mardirossian and Martin Head-Gordon. How accurate are the minnesota density functionals for noncovalent interactions, isomerization energies, thermochemistry, and barrier heights involving molecules composed of main-group elements? *Journal of Chemical Theory and Computation*, 12(9):4303–4325, 2016. doi: 10.1021/acs.jctc.6b00637.

[296] Michal H. Kolář and Pavel Hobza. Computer modeling of halogen bonds and other -hole interactions. *Chemical Reviews*, 116(9):5155–5187, 2016. doi: 10.1021/acs.chemrev.5b00560.

[297] Stefan Grimme, Jens Antony, Stephan Ehrlich, and Helge Krieg. A consistent and accurate ab initio parametrization of density functional dispersion correction (DFT-D) for the 94 elements H-Pu. *J. Chem. Phys.*, 132(15):154104, 2010. ISSN 0021-9606. doi: 10.1063/1.3382344.

[298] Elric Engelage, Nils Schulz, Flemming Heinen, Stefan M. Huber, Donald G. Truhlar, and Christopher J. Cramer. Refined smd parameters for bromine and iodine accurately model halogen-bonding interactions in solution. *Chem. Eur. J.*, 24(60):15983–15987, 2018. doi: https://doi.org/10.1002/chem.201803652.

[299] Philipp Pracht, Fabian Bohle, and Stefan Grimme. Automated exploration of the low-energy chemical space with fast quantum chemical methods. *Phys. Chem. Chem. Phys.*, 22:7169–7192, 2020. doi: 10.1039/C9CP06869D.

[300] Christoph Bannwarth, Eike Caldeweyher, Sebastian Ehlert, Andreas Hansen, Philipp Pracht, Jakob Seibert, Sebastian Spicher, and Stefan Grimme. Extended <scp>tight-binding</scp> quantum chemistry methods. *WIREs Computational Molecular Science*, 11(2), August 2020. ISSN 1759-0884. doi: 10.1002/wcms.1493. URL http://dx.doi.org/10.1002/wcms.1493.

[301] Sebastian Spicher and Stefan Grimme. Robust atomistic modeling of materials, organometallic, and biochemical systems. *Angewandte Chemie International Edition*, 59(36):15665–15673, May 2020. ISSN 1521-3773. doi: 10.1002/anie.202004239. URL http://dx.doi.org/10.1002/anie.202004239.

[302] J. C. Kromann. Calculate root-mean-square deviation (rmsd) of two molecules using rotation. *Calculate Root-mean-square deviation (RMSD) of Two Molecules Using Rotation*, 2020.

[303] H. W. Kuhn. The hungarian method for the assignment problem. *Naval Research Logistics Quarterly*, 2(1–2):83–97, March 1955. ISSN 1931-9193. doi: 10.1002/nav.3800020109. URL http://dx.doi.org/10.1002/nav.3800020109.

[304] W. Kabsch. A solution for the best rotation to relate two sets of vectors. *Acta Crystallographica Section A*, 32(5):922–923, September 1976. ISSN 0567-7394. doi: 10.1107/s0567739476001873. URL http://dx.doi.org/10.1107/S0567739476001873.

[305] Christoph Bannwarth, Eike Caldeweyher, Sebastian Ehlert, Andreas Hansen, Philipp Pracht, Jakob Seibert, Sebastian Spicher, and Stefan Grimme. Extended tight-binding quantum chemistry methods. *WIREs Computational Molecular Science*, 11(2):e1493, 2021. doi: https://doi.org/10.1002/wcms.1493.

[306] Christoph Bannwarth, Sebastian Ehlert, and Stefan Grimme. Gfn2-xtb—an accurate and broadly parametrized self-consistent tight-binding quantum chemical method with multipole electrostatics and density-dependent disper-

sion contributions. *Journal of Chemical Theory and Computation*, 15(3):1652–1671, 2019. doi: 10.1021/acs.jctc.8b01176.

[307] Sebastian Ehlert, Marcel Stahn, Sebastian Spicher, and Stefan Grimme. Robust and efficient implicit solvation model for fast semiempirical methods. *Journal of Chemical Theory and Computation*, 17(7):4250–4261, 2021. doi: 10.1021/acs.jctc.1c00471.

[308] Guilian Luchini, David M.H. Ascough, Juan V. Alegre-Requena, Veronique Gouverneur, and Robert S. Paton. Data-mining the diaryl(thio)urea conformational landscape: Understanding the contrasting behavior of ureas and thioureas with quantum chemistry. *Tetrahedron*, 75(6):697–702, 2019. ISSN 0040-4020. doi: 10.1016/j.tet.2018.12.033.

[309] Julia Bamberger, Florian Ostler, and Olga García Mancheño. Frontiers in Halogen and Chalcogen-Bond Donor Organocatalysis. *ChemCatChem*, 11(21): 5198–5211, 2019. ISSN 1867-3880. doi: 10.1002/cctc.201901215.

[310] Daniel A. Decato, Asia Marie S. Riel, James H. May, Vyacheslav S. Bryantsev, and Orion B. Berryman. Theoretical, solid-state, and solution quantification of the hydrogen bond-enhanced halogen bond. *Angewandte Chemie International Edition*, 60(7):3685–3692, 2021. doi: https://doi.org/10.1002/anie.202012262.

Appendix

A1 Supporting Information

Chapter 3 Monovalent XB-Based Scaffolds

The supporting information for the Michael addition of indole to *trans*-crotonophenone can be found in the following repository:

DOI 10.5281/zenodo.10017508

The supporting information for the ROP of *L*-lactide can be found in the following repository:

DOI 10.5281/zenodo.18486473

Chapter 4 Hypervalent XB-Based Scaffolds

The supporting information for the Michael addition of indole to *trans*-crotonophenone can be found in the following repository:

DOI 10.5281/zenodo.11097065

Chapter 5 Counterion-Induced Conformational Effects in Catalysts

The supporting information for the counterion-induced conformational effects in catalysts study can be found in the following repository:

DOI 10.5281/zenodo.18479408

A2 Published Papers

[1] Nika Melnyk, Iñigo Iribarren, Eric Mates-Torres, and Cristina Trujillo. Theoretical perspectives in organocatalysis. *Chem. Eur. J.*, 28(58):e202201570, October 2022.

[2] Nika Melnyk, Marianne Rica Garcia, Iñigo Iribarren, and Cristina Trujillo. Evolution of design approaches in asymmetric organocatalysis over the last decade. *Tetrahedron Chem*, 5:100035, March 2023.

[3] Nika Melnyk, Rica Garcia, and Cristina Trujillo. Halogen-bond-based organocatalysis unveiled: Computational design and mechanistic insights. August 2023.

[4] James O'Brien, Nika Melnyk, Rico Shing Lee, Michael James, and Cristina Trujillo. Computational design of bidentate hypervalent iodine catalysts in halogen bond-mediated organocatalysis. *ChemPhysChem*, 25(22), October 2024.